ANALYTICAL MODELING OF DISTRIBUTED ARRAY OF RESILIENT PARTICLE IMPACT DAMPERS

A Dissertation
Presented to
The Academic Faculty

by

Kamil Kocak

In Partial Fulfillment
of the Requirements for the Degree
Doctor of Philosophy in the
George W. Woodruff School of Mechanical Engineering

Georgia Institute of Technology
December 2018

COPYRIGHT© 2018 by Kamil Kocak

ANALYTICAL MODELING OF DISTRIBUTED ARRAY OF RESILIENT PARTICLE IMPACT DAMPERS

Approved by:

Dr. Kenneth A. Cunefare,
Committee Chair, Advisor
School of Mechanical Engineering
Georgia Institute of Technology

Dr. Michael J. Leamy
School of Mechanical Engineering
Georgia Institute of Technology

Dr. Aldo A. Ferri
School of Mechanical Engineering
Georgia Institute of Technology

Dr. Massimo Ruzzene
School of Aerospace Engineering
Georgia Institute of Technology

Dr. George A. Lesieutre
School of Aerospace Engineering
The Pennsylvania State University

Date Approved: November 2, 2018

To my wife Seyma and my son Emin Aziz.

ACKNOWLEDGEMENTS

First and foremost, I would like to thank my advisor Dr. Ken Cunefare for his motivation and guidance during my Ph.D. studies. I greatly appreciate his patience, understanding, and help with technical problems and professional development as well as his feedback for papers and conference presentations. His encouragement for being an independent scholar was invaluable. I would also like to thank the other members of my reading committee, Dr. Leamy, Dr. Ferri, Dr. Ruzzene, and Dr. Lesieutre, for their suggestions and approval.

Special thanks to Dr. Fabio Menegatti de Melo for providing experimental results and data which I used in my dissertation; and Nathan Pedigo for his extensive reviews on my papers, presentations, and dissertation. Also, thanks to all my lab mates in IAL and Jason Kulpe from NML, who I consider both friends and colleagues.

I further would like to express my gratitude to my parents and my family for their continuous love and support. I owe the most thanks to my wife Şeyma for her incredible support, patience and dedication, and to my son Emin Aziz who brought so much joy and love to my life.

Finally, I must thank the Ministry of National Education of Turkey, for their financial support for my Ph.D. studies.

TABLE OF CONTENTS

LIST OF TABLES

LIST OF FIGURES

LIST OF SYMBOLS AND ABBREVIATIONS

a	Base oscillation amplitude
c	Damping constant
c'	Structural damping ratio
C_{beam}	Damping matrices of the beam without the PIDs
c_c	Damping constant of the PID ceiling
c_{cr}	Critical damping
c_{eq}	Equivalent viscous damping
c_f	Damping constant of the PID floor
C_j	Damping matrix of the jth state
C_{plate}	Damping matrices of the plate without the PIDs
c_s	Damping constant of the structure
c_w	Damping constant of the PID walls
DOF	Degree of freedom
$D(x,y)$	Bending rigidity
E	Young's modulus
f'	Dimensionless forcing amplitude
f'_{high}	A selected high forcing amplitude
f'_{low}	A selected low forcing amplitude
$F\delta(t)$	Periodic impulse force
F_R	Rayleigh's dissipation function
g	Gravity
h	Gap clearance
h'	Dimensionless gap clearance
h_n	Gap clearance of the n^{th} PID
$h(x,y)$	Plate thickness
I	Cross-section area moment of inertia
k	Spring stiffness
K_j	Stiffness matrix of the jth state
K_{beam}	Stiffness matrices of the beam without the PIDs
k_c	Spring stiffness of the ceiling
k_f	Spring stiffness of the floor
K_{plate}	Stiffness matrices of the plate without the PIDs
k_s	Spring stiffness of the structure
k_w	Spring stiffness of the PID walls
L	Length of the beam
L_x	Width of the plate
L_y	Length of the plate
m	Mass of the base
m'	mass ratio

$\boldsymbol{M_{beam}}$	Mass matrices of the beam without the PIDs
$\boldsymbol{m_b(x)}$	Mass per unit length of the beam
$\boldsymbol{M_j}$	Mass matrix of the jth state
$\boldsymbol{m_p}$	Mass of the particle
$\boldsymbol{m_{p,i}}$	Mass of the i^{th} particle
$\boldsymbol{M_{plate}}$	Mass matrices of the plate without the PIDs
$\boldsymbol{m_{pl}(x,y)}$	Mass per unit area of the plate
$\boldsymbol{m_s}$	Mass of the enclosure
$\boldsymbol{m_{s,i}}$	Mass of the i^{th} enclosure
$\boldsymbol{PID}$	Particle impact damper
$\boldsymbol{q}$	Generalized coordinates
$\boldsymbol{Q}$	Generalized force
$\boldsymbol{(Q_i)_{visc}}$	Viscous damping forces
$\boldsymbol{Sn}$	n^{th} spot on the beam starting from the free end
$\boldsymbol{(v_{rms})_{noPID}}$	RMS velocity of the base mass without an impact damper
$\boldsymbol{(v_{rms})_{PID}}$	RMS velocity of the base mass with an impact damper
$\boldsymbol{x'}$	dimensionless displacement
$\boldsymbol{x_F}$	Forcing location along the length of beam
$\boldsymbol{(x_F, y_F)}$	Forcing location on the plate
$\boldsymbol{x_i}$	Location of the i^{th} PID (along the length of beam)
$\boldsymbol{\Delta t}$	Time step
$\boldsymbol{\eta}$	Loss factor
$\boldsymbol{\lambda}$	Proportionality constant
$\boldsymbol{\mu}$	Proportionality constant
$\boldsymbol{v}$	Poisson's ratio
$\boldsymbol{\rho}$	Density of the plate
$\boldsymbol{\varphi}$	Assumed mode basis function
$\boldsymbol{\psi}$	Velocity ratio
$\boldsymbol{\omega}$	Excitation frequency
$\boldsymbol{\omega'}$	Frequency ratio
$\boldsymbol{\omega_n}$	Natural Frequency

SUMMARY

Particle impact dampers (PIDs) or shot mass dampers are known to provide high loss factors on vibrating structures by dissipating kinetic energy through particle-enclosure and particle-particle collisions. The rate of energy dissipation is amplitude dependent, which makes the particle damping highly nonlinear. Previous studies have focused on horizontal excitation (perpendicular to gravity) for particle damping. Vertically excited systems (parallel to gravity) have also been studied in the literature, in which the excitation has generally been considered to be harmonic. However, harmonic disturbances do not accurately represent some cases where repetitive impacts occur, such as manufacturing and maintaining aircraft structures with the operations of riveting and chiseling. This study is concerned with developing analysis methods for PIDs under periodic impulse excitation in the vertical direction. Impulse excitation differs from harmonic excitation in the sense of response modeling. Systems under harmonic excitation are subject to forced-response, whereas the effect of an impulse excitation is equivalent to the effect of an initial velocity condition at the impulse application time, and a free decay until the next impulse. Therefore, the systems considered herein are inherently in free-response and unforced between impulses. Particle damping is analyzed for i) a single resilient PID, ii) a cantilever beam with multiple PIDs attached to various locations on the beam, and iii) a simply supported plate with multiple PIDs attached to various locations on the plate. These analyses are used for an optimization of a distributed array of PIDs on a cantilever beam and on a simply supported plate.

The method of assumed modes and Lagrange's equations are used to model a cantilever beam and a simply supported plate. In order to simulate the PID response, the use of Linear Time Invariant methods are found to be most efficient, because the PID is never truly in a steady-state

condition. Finally, a genetic algorithm, is used to optimize the distributed array of PIDs because of the complexity and nonlinearity of the problem.

CHAPTER 1

INTRODUCTION

1.1 Overview

A particle impact damper (PID) or a shot mass damper (SMD), see Figure 1 for an array of PIDs, is a particle-filled enclosure used as a passive damping device attached to vibrating structures. Particle-enclosure and particle-particle collisions arise due to a clearance between particles and the enclosure walls. Damping mechanisms in PIDs involve internal friction and momentum transfer through inelastic impacts, which cause the rate of energy dissipation to be amplitude dependent, and the particle damping process to be highly nonlinear. Although the damping process is nonlinear and not amenable to exact analytical solutions, PIDs are interesting because they can provide a strong rate of energy dissipation within a broadband frequency range with a small weight penalty [1]. PID systems are able to achieve high loss factors by absorbing the *kinetic energy* of a structure which then leads to dissipation as heat, while traditional viscoelastic damping treatments convert the *elastic strain energy* stored to heat. Viscoelastic damping treatments include tapes and coatings which might be applied to control continuous structures. Compared to the traditional methods, PIDs can operate in harsher environments, in contrast with the damping properties of viscoelastic materials, which diminish due to temperature, aging or strain rate.

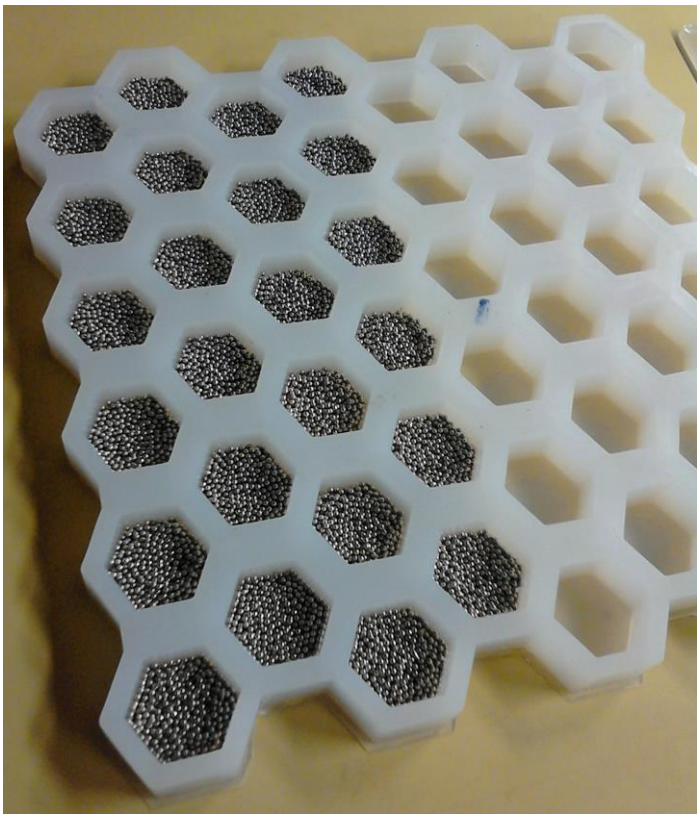

Figure 1: An array of particle impact dampers. The left half of the array is filled with nickel-plated lead shots. The right half shows the empty PID enclosures which is made of rubber [2].

The majority of previous studies have focused on horizontal excitation for particle damping where gravity is not a factor [3–18]. Vertically excited systems have also been studied in the literature, in which the excitation has generally been considered to be harmonic. However, harmonic disturbances do not accurately represent some cases where repetitive impacts occur, such as manufacturing and maintaining aircraft structures with the operations of riveting and chiseling [19]. This research is concerned with investigating analytical characterization of PIDs under periodic impact excitation in the vertical direction. Studies showed that the PID stops working for acceleration amplitudes below a certain level and behaves like a mass damper [20]. This hybrid behavior is taken into account in the analytical model. A novel model with "soft-floor and soft-ceiling" of PIDs is introduced to combine the advantages of PIDs and mass dampers.

1.2 Motivation

Applications areas of particle impact dampers include but are not limited to manufacturing and maintaining aircraft structures. Sheet metal is commonly used during these processes. Assembly and disassembly operations of sheet metal such as riveting, chiseling, punching, etc., are known to generate loud noise. Nelson et al. [21] states that the noise produced by sheet metals may potentially damage the hearing capability of the operators because of their dynamical properties.

Particle damping is a known solution to reduce the noise directly at its source. Traditionally, PIDs are permanently attached to vibrating structures which is not desirable during manufacturing processes where they are needed for temporarily. Traditional PIDs are also made of hard materials such as metals, hard plastics etc. This is disadvantageous because some products may have curved surfaces, which would cause problems on attachment points. Unlike these traditional PIDs, it is aimed to model flexible and removable PIDs in this study. An analysis method is developed for PIDs under periodic impulse excitation in the vertical direction.

1.3 Objectives

There are 4 main research objectives in this study. Particle damping is analyzed for (i) a novel single PID model with “soft-floor and soft-ceiling” to have a flexible and a removable PID solution, (ii) a cantilever beam with multiple PIDs attached to various locations of the beam, (iii) a simply supported plate with multiple PIDs attached to various locations of the plate, and (iv) optimization of the distributed array of PIDs on a cantilever beam and on a simply supported plate.

Objectives 1-3 include construction of a time stepping algorithm. The dynamical properties of the system are determined and time of impacts between the particles and the enclosure is found using an iterative solution method. The process consists of piecewise linear equations between any break points, so that LTI methods are used to find the system response. Each break point is analyzed to determine the initial conditions of the next linear equation. Then, it is possible to calculate the effectiveness of the PIDs in a given time range. The model allows for the observation of time domain features, such as the trajectories of both the particles and the enclosure, time of impacts, and effects of periodic impulse excitation.

Objective 4 has the main goal of developing an optimization solution. The motivation is as follows: Do uniformly or non-uniformly filled arrays of closely-spaced PIDs provide a better and more robust performance for an arbitrary excitation point in the broadband frequency range? A genetic algorithm is employed for the optimization because of the complexity and nonlinearity of the problem.

1.4 Unique Contributions

In this dissertation, a novel resilient and removable PID model with "soft-floor and soft-ceiling" is introduced and analytically examined under periodic impulse excitation in the vertical direction for the first time. Effects of various parameters on a single PID, a beam with distributed array of PIDs, and a plate with distributed array of PIDs are analyzed. Optimum PID locations and gap clearances (the distance between the top of the enclosure and the particles) are sought for a cantilever beam and a simply supported plate.

Analyses on a single PID provided the following innovative findings:

- Treating PIDs as state-switched devices and using LTI simulation methods for response modeling are validated by comparing the simulation results with studies in the literature.
- A new performance metric, velocity ratio, is introduced which is defined as the ratio of RMS velocity of the base mass without an impact damper to the RMS velocity of the base mass with an impact damper.
- When a limit stop is used to model the compressional length of the resilient PID floor and ceiling, the model with the limit stop approaches to a higher velocity ratio value than the model without the limit stop as the forcing amplitude goes to infinity. However, in both cases the maximum effectiveness values and corresponding forcing amplitudes are the same. Therefore, using limit stop does not affect the optimum forcing amplitude and the resultant effectiveness.
- Ideally, the impulse force is assumed to be applied instantaneously. However, in reality it takes finite amount of time to apply the force. If an evenly distributed force is considered, maximum effectiveness decreases, and corresponding forcing amplitude increases as the forcing duration increases. However, when a triangular impulsive force is considered, there is not a significant change in the analysis results as the forcing duration increases.

Analyses on a cantilever beam with distributed array of PIDs provided the following innovative findings:

- PIDs have more potential under impulse excitation with respect to harmonic excitation to provide higher performance within a broadband frequency range.

The average performance is higher for the impulse excitation compared to the harmonic excitation within the same excitation frequency range.

- There is an optimum gap clearance for a PID attached to a cantilever beam and optimum gap clearance is higher for higher forcing amplitudes. This means, for an arbitrary excitation and PID arrays, non-uniform gap clearances may be more effective.

The following results are valid when the beam is excited at the first natural frequency and the ratio of the mass of the PIDs to the mass of the beam is 0.1:

- For a fixed forcing location, PID effectiveness increases as the PIDs are moved towards the free end of the beam.
- For fixed PID locations, PID effectiveness increases as the forcing location is moved towards the free end of the beam.
- For an arbitrary forcing location, a single PID at the free end of the beam is more effective than multiple PIDs.

Analyses on a simply supported plate with distributed array of PIDs provided the following innovative findings:

- When the excitation frequency is varied around the first natural frequency of the plate, tuning the PID to the first natural frequency of the plate decreases the maximum velocity amplitude over the plate corresponding to the peak frequencies compared to the untuned case and helps the response to be less sensitive to the frequency variation. However, there is not a significant difference between the two cases if the average of the maximum velocity amplitudes in the broadband

frequency range is considered. Overall, the PIDs should be tuned especially if the objective is to reduce the maximum velocity amplitude in the system.

- When the mass of the PID compared to the mass of the plate is low, PID effectiveness depends on the excitation frequency and the resultant deflection shapes. On the other hand, when the mass of the PID compared to the mass of the plate is high, PIDs are more effective when they are closer to the excitation.
- The difference between low and high mass ratios is a result of the effects of mass loading vs. damping on the effectiveness. The role of mass loading on the PID effectiveness is generally neglected in PID studies. However, the analysis results showed that for low mass ratios the effect of damping on the effectiveness is more dominant whereas for high mass ratios the effect of mass loading is the dominant factor.
- Keeping the total mass of the PIDs constant, if the number of PIDs with uniform gap clearances increases, the effectiveness also increases.

Optimization of the gap clearances for PIDs on a cantilever beam and a simply supported plate provided the following innovative findings:

- For a fixed excitation frequency, optimizing the gap clearances for an arbitrary forcing location improves the PID effectiveness. Non-uniform gap clearances are more effective than uniform gap clearances.
- Frequency analysis showed that the advantage of the optimum case is significant only around the resonance frequency which is the same as the optimization frequency. For other frequencies, either the advantage is relatively small or the

PIDs with uniform gap clearances have better effectiveness. Overall, non-uniformly filled arrays of PIDs found to have slightly higher performance.

1.5 Organization of the Thesis

This dissertation consists of 7 chapters. **Chapter 2** reviews the particle impact dampers background. The research that has been conducted on single PIDs, PIDs attached to continuous structures, and optimization of PIDs is presented.

The modeling of the PIDs is divided into 4 chapters. **Chapter 3** presents the PID systems considered. 3 different PID models are compared and one of them is chosen for further analysis. Equivalent viscous damping model and analytic equations related to response modeling are provided. Simulation results of various parameters affecting PIDs are discussed. **Chapter 4** and **Chapter 5** detail the modeling of PIDs on a beam and a plate, respectively. Equations of motion and system matrices derived for a distributed array of PIDs on continuous structures. **Chapter 6** shows the optimization of the gap clearances of a distributed array of PIDs attached to a cantilever beam and a simply supported plate. The optimization technique employed is described and the results from the optimization of the beam and the plate are presented.

Finally, **Chapter 7** summarizes the work done in the study and provides conclusions.

CHAPTER 2

LITERATURE REVIEW

2.1 Overview

Particle impact damping has been researched experimentally, analytically, and numerically for more than half a century. Although there have been developments in the analysis techniques over the past years, modeling PIDs is still a challenge because of the nonlinear behavior of particle damping. Additionally, the performance of the PID is affected by a large number of design parameters such as device parameters and excitation parameters. The device parameters include *gap clearance* (the distance between the top of the enclosure and the particles), damping ratio, mass ratio, particle properties (size, shape and material), and enclosure properties (size, geometry and material). The excitation parameters include vibration amplitude, excitation frequency, and excitation type (e.g. harmonic, impulse, random).

This chapter is organized as follows. First PID background is presented and studies about PID modeling are briefly reviewed. Rigid and resilient impact dampers are compared and energy dissipation mechanism in resilient PIDs is discussed. Then studies that focused on PIDs on continuous structures are reviewed. Finally, PID optimization studies are shown and state-switched devices are described.

2.2 Particle Impact Dampers Background

In the literature, the term *impact dampers* refer to the devices, which contain a single moving mass inside of an enclosure; whereas the terms *particle dampers* or *particle impact dampers* refer to the devices with multiple impacting masses (see Figure 2). Impact dampers are effective in reducing the response of lightly damped structures under dynamic loading, and it is

possible to derive exact analytical solutions for certain configurations [3]. However, the performance of impact dampers is sensitive to changes in the excitation amplitude and the size of the enclosure. Also, accelerations and forces that are produced during the impact process can cause high levels of noise and deterioration of interface materials [4]. Papalou and Masri [4] showed that, by replacing the single moving mass of an impact damper with a number of particles of equivalent total mass (resulting in a particle damper), the aforementioned problems might be diminished or eliminated.

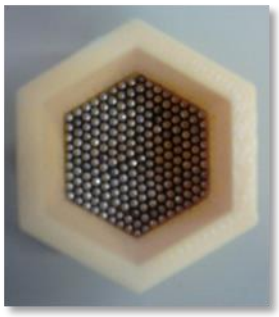

Figure 2: A particle impact damper (top view).The ceiling of the PID enclosure has been removed for a better representation.

2.3 Particle Impact Damper Modeling

Researchers have used various techniques to model particle dampers. To simplify the inherent mathematical complexity, most of the studies focused on modeling a bed of particles as a single particle [22]. Although impact dampers have drawbacks over particle dampers such as being much more sensitive to operating conditions and parameters, modeling a particle damper as an impact damper is a preferred analytical approximation technique [23,24]. This dissertation also uses this approach, i.e. the bed of particles is assumed to be a single particle, which moves in the direction of gravity.

Excitation direction is important for PID modeling, because gravity acts in the direction of particle motion for vertical excitation; whereas it is generally neglected for horizontal

excitation except to the extent that it might permit friction losses. Therefore, impact damping literature may be categorized by the excitation direction. Most studies have focused on excitation in the horizontal plane [3–18]. Without the effect of gravity, modeling the system is relatively simple because impacts may produce symmetric motion. Masri [5] showed that when the impact damper is in steady-state motion with two impacts per cycle, the impacts are generally equally spaced in time, and the motion of the system is symmetric about its equilibrium position. Bapat and Sankar also considered symmetric periodic motion for their studies on single unit [7] and multi-unit impact dampers [8]. Their theoretical results showed that replacing a single unit with a number of units having equivalent total mass retains the vibration amplitude reduction, but decreases the velocity discontinuity of the main mass at the impacts. In the case of symmetric two impacts per cycle motion, they found that impacts were not evenly distributed over the entire cycle. Witt and Kinra [14,15] performed experiments to show that PIDs can provide an efficient method of damping for horizontally vibrating structures under transient conditions. Zahrai and Rod [17] found out that impact dampers are effective devices for reducing vibration under impulsive and harmonic excitations. A single, horizontal, and triangular impulsive load was applied at the beginning of their simulation whereas repetitive and vertical excitations were considered in this dissertation.

All of the previously described works involve the excitation in the horizontal direction. However, there are some applications where the system is vertically excited, meaning gravity cannot be neglected. PID systems under vertical excitation have also been studied [1,2,19–27]. Friend and Kinra investigated vertical PIDs both experimentally and numerically [25,26]. They constructed an analytical model to calculate cycle-by-cycle damping, and to capture the amplitude dependent behavior of particle damping. Ramachandran and Lesieutre [27] modeled a

single-particle impact damper under harmonic excitation. The time simulation of impacts between particle and enclosure walls is derived using an implicit set of difference equations. Duncan et al. [28] also modeled a single-particle impact damper under harmonic excitation. However, this time the damper structure was attached to the base with a spring and a damper. In both studies, a fixed coefficient of restitution was used. Yang et. al [22] experimentally developed design curves for PIDs to predict the damping characteristics. The effects of vibration amplitude, excitation frequency, gap clearance and particle mass were analyzed under harmonic loading.

While PIDs have been studied heavily under harmonic excitation, modeling arrays of PIDs with "soft-floor and soft-ceiling" under periodic impulse excitation is a new research opportunity. Impulse excitation differs from harmonic excitation in the sense of response modeling. Systems under harmonic excitation are subject to forced response, whereas the effect of an impulse excitation is equivalent to the effect of an initial velocity condition at the impulse application time, and a free decay until the next impulse [32].

2.3.1 Resilient Particle Impact Dampers

In resilient PIDs, impacts between the particle and the enclosure deform the contacting surfaces. The impact duration is longer as compared to an equivalent rigid PID. Therefore, coefficient of restitution models fail and the impact duration must be considered for proper modeling [33]. Cheng and Wang [34] used a spring-damper model to formulate the deformation during the impacts of a vibratory system equipped with a resilient impact damper, so that the impact duration was taken into consideration. Li and Darby [35–38] also presented a similar spring-damper model and compared theoretical and experimental results. The spring-damper model was shown to be effective in situations where the impulse-momentum model fails.

2.3.2 Equivalent Viscous Damping Model

Chen et al. [39] studied the main energy dissipation mechanism in rigid PIDs using discrete element method. They showed that the effectiveness of frictional dissipation is on the same numerical scale as that of collision mechanism. Xiao et al. [40] also used the discrete element method and developed an energy dissipation model accounting for friction and inelastic collisions.

Energy dissipation mechanism on resilient impact dampers has also been studied. Chen and Wang [34] analytically modeled a resilient impact damper system assuming a viscous type damping because the damping capacity of the vibratory system is predominantly produced in the contacting surface. Michon et al. [41] replaced hard particles with soft hollow ones in honeycomb structures. Experimental and theoretical validations showed that, instead of dissipation by friction and impact, visco-elastic behavior was dominant. Li and Darby [33] introduced a flexible buffer zone between the moving particle and the stop fixed onto the primary system. The damping characteristics of the buffered damper were investigated, and a spring-damper model of the buffer is found to be more appropriate rather than a coefficient of restitution model. In another study [35], the same authors calculated the stiffness and damping parameters of the aforementioned model using measured coefficient of restitution and contact time data.

2.3.3 Nonlinear Energy Sinks

A PID can be thought as a nonlinear energy sink (NES). NESs are strongly nonlinear, passive, and local attachments which are employed to alter the dynamics of the primary system to which it is attached. Properly designed NESs can capture and dissipate either narrowband or

broadband energy. NESs were introduced and detailed by Vakakis et al [42]. Analytical and experimental studies were carried out for mitigation vibration due to impulsive excitation [43–45]. However, most of the NES studies considers horizontal excitation as in the case of PID studies. For example, Li et al. [46] analytically studied a linear oscillator coupled with a vibro-impact NES under horizontal periodic and transient excitations. An asymmetric, single-sided vibro-impact NES for shock mitigation was studied by Al-Shudeifat et al. [47]. The proposed NES passively absorbs and dissipates the impulse energy induced into the structure. A clearance-type nonlinear energy sink (NES) is explored by Darabi and Leamy [48] for increasing electrical energy harvesting during impact events. Either side of the clearance contain displaceable degrees of freedom which is not typical for single-DOF NES studies. Two different approaches are considered for gap modeling: a coefficient of restitution and a stiff gap spring model. Coefficient of restitution model assumes the contact between the two sides of the gap occurs in zero time whereas in the stiff gap spring model contact and separation occurs over a finite time. To sum up, PIDs are closely related to NESs, and NES literature may be explored for studies that aim to characterize the nonlinearity in vibro-impact systems and exploit the energy trapped or dissipated.

2.4 PIDs on Continuous Structures

The majority of particle damping studies in the literature involve testing PIDs on a structure such as a cantilever beam. Continuous structures with PIDs are generally modeled as single degree of freedom (SDOF) systems [15,25,26,31]. For example, Friend and Kinra [25,26] reduced the continuous cantilever beam system in Figure 3(a) to an equivalent SDOF system at the free end of the beam in Figure 3(b). The beam was assumed to vibrate in its fundamental mode. Then the reduced mass, stiffness, and damping coefficient of the beam were used to find

the response of the system. While this simplification provided good agreement between theory and experiment, multi degree of freedom (MDOF) systems are needed to model structures with more than one PID placed at different locations on the continuous structure.

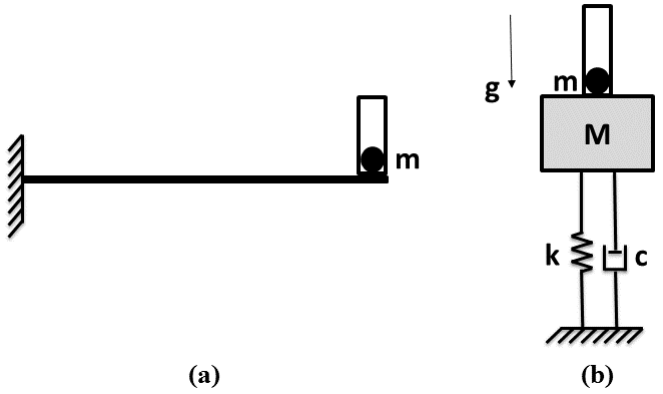

Figure 3: Model reproduced from Friend and Kinra [26]. (a) Schematic of a cantilever beam and a PID. (b) The equivalent single degree of freedom system.

Roy et al. developed a finite element model for clamped and simply supported beams under harmonic excitation [16]. For both cases, an impact damper is installed in the mid-position. They assumed that an impact affected the velocity of the beam only at the point of the impact. The results demonstrated the effectiveness of the impact damper near the resonant frequencies. The effectiveness was found to be directly related to the mass of the impact damper. Also for a damper of a given mass, there was a specific clearance that produced the most effective reduction in response. This result is particularly important for optimization purposes.

Butt and Akl [29] developed a finite element model for beams with non-classic boundary conditions. Impacts of the damper are modeled considering a change in the velocities of all points of the structure at each impact, because experimental studies showed that the velocities of all points are affected by the impacting mass. Conservation of momentum is assumed to occur between the mass of the particle and the entire mass of the structure. In this way, the continuity of the system was taken into account.

Trigui et al. [49] investigated dynamic response of a plate treated by PID under harmonic excitation. The damping of PID was measured without a supplementary use of a primary structure. Then, the nonlinear damping was converted into an equivalent viscous damping coefficient and used in a finite element model of a free-free plate. The dynamic response was predicted by considering the dependence on the excitation frequency. The dependence on the excitation amplitude was neglected, which caused the numerical and experimental responses to be different.

2.5 PID Optimization

Optimization of a single PID has been studied heavily in literature, especially for harmonic excitations. Previous studies on PIDs show that there is an optimum gap clearance (the distance between the top of the enclosure and the particles) for a single PID with a given set of parameters such as excitation amplitude, mass ratio, damping ratio etc. Butt and Akl [29] considered the placement of an impact damper along the length of a beam and showed that the damper is most effective when located close to the anti-nodes. The optimum gap clearance was found to be smaller for modes occurring at higher frequencies. Papalou and Masri [13] showed that higher values of mass ratio result in less efficient decrease in the response amplitude. However, average velocities between different mass ratios were not compared.

Popplewell and Liao [9] discussed the optimum design for a single horizontal impact damper under harmonic excitation. The effects of damping ratio, coefficient of restitution, and mass ratio were analyzed for the optimum gap clearance and displacement reduction. Papalou and Masri [13] carried an analytical and experimental study of the performance of particle dampers under wide-band random excitation. An approximate analytical solution, which was based on an equivalent single degree of freedom system, provided adequate estimate of the

response when the particle damper is operating near its optimum range of parameters. While these studies are helpful when designing a system with a single PID, there is not much known about the optimum configurations of an array of PIDs.

Panossian et al. [50] used the term "non-obstructive particle damping (NOPD)" to describe the placing of particles inside cavities of or attached to structures by an appropriate means. The NOPD treatment in honeycomb structures was studied to develop a finite element modeling analyses. The results showed that the damping due to particles in panel cells can be significant for both high and low frequencies. In another study, Panossian and Ehrgott [51] considered the optimal fill configuration for a honeycomb panel under random excitation by minimizing the highest dynamic displacements of several vibration modes of the structure and the additional weight of the particles. A genetic optimization algorithm was used and the optimal design configuration was tested in the laboratory. The results showed that the optimal treatment was not uniform, and the panel with the optimal treatment was superior to the uniform fill configuration. Although the excitation types are different, this may indicate that the gap clearances of the array of PIDs considered herein should also be non-uniform.

Since PIDs can provide high rate of energy dissipation within a broadband frequency range, it is of interest to develop a robust optimum solution for distributed array of PIDs in a broadband range. In order to maximize the impact damping, analyses of the PID locations on the structure and fill ratios (or gap clearances) of the PIDs are necessary.

2.6 State-Switched Devices

The majority of the PID models for continuous systems involve finite element methods (FEM). While FEM is a powerful approximate solution and is preferred in most instances for

complex geometries, state-dependent and discontinuous behavior of PIDs needs to be considered for proper modeling which might not be possible for commercial FEM codes.

Devices that can instantaneously change one or more of its dynamical properties, that is, its mass, stiffness, or damping are called state-switched devices [52]. A PID can be treated as a state-switched device, because the mass of the system changes at the time of sticking or separation between the particle and the enclosure. For PIDs, the aim is not to control the instant of the switches like in traditional state-switched devices. However, if the time of impacts is tracked, the same solution methods and response modeling techniques can be applied to PIDs. Cunefare [53] used the method of assumed modes and Lagrange's equations to model a cantilever beam with a state-switched tuned vibration absorber. An absorber with state-switchable stiffness was considered and Linear Time Invariant (LTI) simulation methods were used for response modeling.

For a piecewise function, the points where the slope of the function changes are known as "break points". A PID does not achieve a steady-state condition because of the break points in the system. An impact between the enclosure and the particle, an impulse excitation, and limit stops are available break points for the systems considered in this study. These break points generate start-up transients each time they occur due to the dependence of the solution on the initial conditions that are present after the break [54]. For this reason, initial conditions must be accounted for at each break point for proper modeling of the response and a time stepping algorithm will be the most efficient approach.

In this dissertation, LTI methods are used to simulate the PIDs with state-switchable mass, stiffness, and damping. The PID system is linear and time invariant between any two break

points. At the time of a break point, all the matrices and initial conditions will be updated to reflect the effect of the break.

CHAPTER 3

ANALYTICAL MODELING OF A SINGLE RESILIENT PARTICLE IMPACT DAMPER UNDER PERIODIC IMPULSE EXCITATION

3.1 Overview

This chapter develops analysis techniques for a single resilient particle impact damper (PID) under periodic impulse excitation. The chapter begins with presenting three PID systems considered. Equations of motion and system matrices are developed for a rigid impulse-momentum and two different resilient spring-damper models. Then, an equivalent viscous damping model is introduced, and the response modeling is derived. Metric of performance for the PID systems is described. Finally, various simulation results are shown to characterize the PID effectiveness.

3.2 Systems Considered

There are 3 PID systems considered in this study. *Model 1* is an impulse-momentum model where the impacts are governed by a coefficient of restitution. Most of the investigations in the PID literature utilize the same assumption, in which the impact duration between the particle and the enclosure is neglected. This is a good approximation for the impacts between two hard surfaces [34]. However, the objective here is to characterize resilient PIDs, and *Model 1* is only utilized to compare the solution techniques here with the literature.

In resilient PIDs, impacts between the particle and the enclosure deform the contacting surfaces. The impact duration is longer as compared to an equivalent rigid PID. Therefore, coefficient of restitution models fail, and the impact duration must be considered. A similar

spring-damper approach to that of [34,55] is followed herein for *Model 2* and *Model 3* to formulate the deformation during the impacts between the particle and the enclosure, so that the impact duration was taken into consideration. The difference between the two models is, *Model 2* has hard lateral walls, whereas *Model 3* uses an extra pair of spring-damper to model the soft walls. The two models are analyzed and compared.

3.2.1 Model 1: Impulse-Momentum Model

Figure 4 shows the schematic of the modeled system. A periodic impulse force $F\delta(t)$ is applied to the enclosure in the vertical direction. The base mass m, enclosure mass m_s, and particle mass m_p are under the effect of gravity, g.

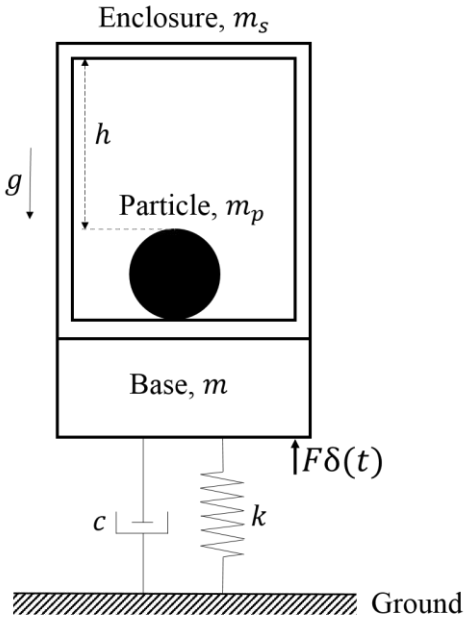

Figure 4: A schematic of the modeled vertical particle impact damper system with a limit stop for *Model 1*. (m_s: mass of the enclosure, m_p: mass of the particle, m: mass of the base, h: gap clearance, k: spring stiffness, c: damping constant, $F\delta(t)$: impulse force)

Impacts between the particle and the enclosure are characterized by a coefficient of restitution, ε. The value of the coefficient of restitution was chosen to be zero, because the

effective coefficient of restitution for multiple-particle dampers is approximately zero [24,28]. Thus, this method can be extended to multiple-particle dampers.

The model consists of piecewise continuous time-domain functions. There are two types of break points: (i) an impact between the enclosure and the particle, and (ii) impulse excitation. Between any two break points, the system is assumed to be linear and continuous.

The general form of the equations of motion is

$$M\ddot{q} + C\dot{q} + Kq = Q\ , \tag{3.1}$$

where M, C and K are mass, damping and stiffness terms, respectively, Q is the excitation force, q is the displacement, $\dot{q}$ is the velocity, $\ddot{q}$ is the acceleration of the base and enclosure.

For *Model 1*, mass is the only state-switchable term, and the number of mass states is equal to the number of equations of motion,

$$\begin{matrix} M_1\ddot{q} + C\dot{q} + Kq = Q \\ \cdots \\ M_{sN}\ddot{q} + C\dot{q} + Kq = Q \end{matrix}\ , \tag{3.2}$$

where subscript sN indicates the state number. However, only one of the equations of motion is the effective one, depending on the state of particles (i.e. sticking or separation states).

At any point of time of the simulation, the particle can have one of the following three states: (1) stuck to the enclosure floor, (2) stuck to the enclosure ceiling, (3) free flight where it moves separately from the enclosure. Here, the term “stuck” is used to describe the condition of the particle mass being held in contact with the enclosure floor or ceiling due to the acceleration of the enclosure. Hereafter, numeric subscripts are used to indicate the corresponding state.

The mass, stiffness, and damping matrices for the three states are:

$$M_{1,2} = m + m_s + m_p, \quad M_3 = m + m_s, \quad K_{1,2,3} = k, \quad C_{1,2,3} = c. \tag{3.3}$$

When the particle is stuck to the enclosure floor, it separates from there if the acceleration of the enclosure, $\ddot{q}$, is less than gravity,

$$\ddot{q} < -g\ . \tag{3.4}$$

When the particle is stuck to the ceiling of the enclosure, it separates from there if the acceleration of the enclosure is greater than gravity,

$$\ddot{q} > -g\ . \tag{3.5}$$

After the particle separates from the enclosure, it enters into the free flight mode. When the particle is in free flight mode, and then at some later time again comes into contact with the enclosure, it sticks to the enclosure if both of the following conditions are satisfied: (i) the relative velocity between the particle and the enclosure is less than some tolerance; (ii) the absolute velocity of the enclosure has the same sign as that of the absolute velocity of the particle. Using a tolerance has the advantage of not having to model the system during a large number of closely spaced low-velocity impacts. However, it should have a very low value, because the sticking time affects effectiveness. Ramachandran and Lesieutre [27] used 10^{-9} m/s as a good tolerance for the sticking condition in their numerical model. Therefore, the same value is used in this research.

3.2.2 Model 2: Resilient Spring-Damper Model with Hard Lateral Walls

In *Model 2*, both the ceiling and the floor of the enclosure are assumed to be made of a soft material such as silicone rubber [19], so that the PID floor and ceiling are attached to the enclosure with a spring and a damper. Since the compressional length of the floor and ceiling is

limited due to the thickness of the material, there is a limit stop between the enclosure and the floor and between the enclosure and the ceiling.

The schematic of the system can be seen in Figure 5. The same 3 states are still valid from *Model 1*. The particle can be: (i) stuck to the enclosure floor, (ii) stuck to the enclosure ceiling, (iii) in free flight where it moves separately from the enclosure. However, this time there are three types of break points: (i) an impact between the enclosure and the particle, and (ii) impulse excitation, and (iii) the limit stops.

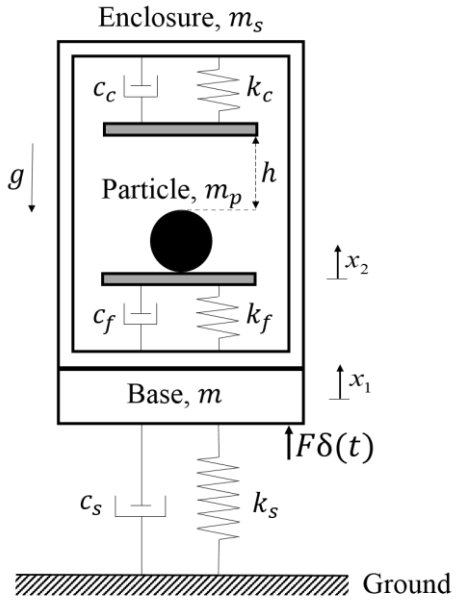

Figure 5: A schematic of the modeled vertical particle impact damper system for *Model 2*. (m_s: mass of the enclosure, m_p: mass of the particle, m: mass of the base, h: gap clearance, k_c: spring stiffness of the ceiling, k_f: spring stiffness of the floor, k_s: spring stiffness of the structure, c_c: damping constant of the ceiling, c_f: damping constant of the floor, c_s: damping constant of the structure, $F\delta(t)$: impulse force)

The general form of the equations of motion is

$$M\ddot{q} + C\dot{q} + Kq = Q\,, \tag{3.6}$$

where M, C and K are mass, damping and stiffness matrices, respectively, Q is a vector of forces, q is a vector of physical or generalized coordinates.

For *Model 2*, stiffness and damping are the state-switchable terms, and the number of states is equal to the number of equations of motion,

$$\begin{matrix} M_1\ddot{q} + C_1\dot{q} + K_1 q = Q \\ \cdots \\ M_{sN}\ddot{q} + C_{sN}\dot{q} + K_{sN} q = Q \end{matrix} . \tag{3.7}$$

where subscript *sN* indicates the state number. Only one of the equations of motion is the effective one, depending on the state of particles.

State 1: When $x_2 - x_1 < 0$, the particle collides with the enclosure floor. The mass, stiffness, and damping matrices are,

$$M_1 = \begin{bmatrix} m + m_s & 0 \\ 0 & m_p \end{bmatrix}, \tag{3.8}$$

$$K_1 = \begin{bmatrix} k_s + k_f & -k_f \\ -k_f & k_f \end{bmatrix}, \tag{3.9}$$

$$C_1 = \begin{bmatrix} c_s + c_f & -c_f \\ -c_f & c_f \end{bmatrix}. \tag{3.10}$$

State 2: When $x_2 - x_1 > h$, the particle collides with the enclosure ceiling. The mass, stiffness and damping matrices are the same as in *State 1* except the subscript *f* (floor) must be replaced with the subscript *c* (ceiling).

State 3: When $0 \le x_2 - x_1 \le h$, the particle is in free flight. The motion of the particle is followed separately with,

$$x_2 = x_0 + v_0 t - \frac{1}{2} g t^2 , \tag{3.11}$$

where x_0 and v_0 are the initial displacement and velocity just after the separation from the enclosure, respectively. Although structure DOF decreases to 1 at this state, the DOF of the

system matrices is kept the same for simulation simplicity after the stiffness and the damping matrices are decoupled, so that the 2nd DOF does not affect the 1st. The results of the second DOF are discarded at this state. The mass, stiffness and damping matrices are,

$$M_3 = \begin{bmatrix} m + m_s & 0 \\ 0 & m_p \end{bmatrix}, \tag{3.12}$$

$$K_3 = \begin{bmatrix} k_s & 0 \\ 0 & 1 \end{bmatrix}, \tag{3.13}$$

$$C_3 = \begin{bmatrix} c_s & 0 \\ 0 & 0 \end{bmatrix}. \tag{3.14}$$

3.2.3 Model 3: Resilient Spring-Damper Model with Soft Lateral Walls

Model 3, schematically depicted in Figure 3, uses the same principles with *Model 2* except the soft lateral walls are modeled using extra spring-damper.

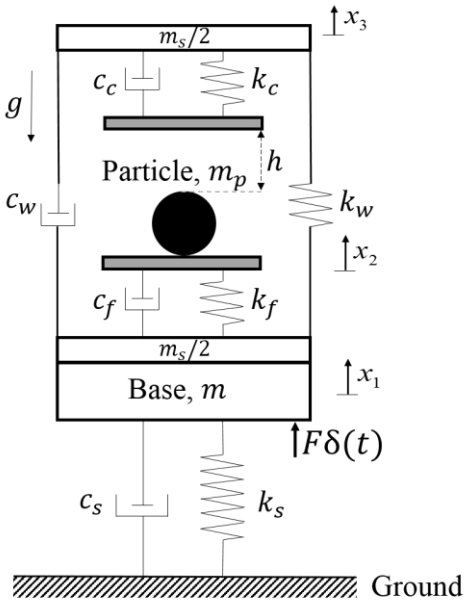

Figure 6: A schematic of the modeled vertical particle impact damper system for *Model 3*. (m_s: mass of the enclosure, m_p: mass of the particle, m: mass of the base, h: gap clearance, k_c: spring stiffness of the ceiling, k_w: spring stiffness of the walls, k_f: spring stiffness of the floor, k_s: spring stiffness of the structure, c_c: damping constant of the ceiling, c_w: damping constant of the walls, c_f: damping constant of the floor, c_s: damping constant of the structure, $F\delta(t)$: impulse force)

Equations of motion derived for *Model 2* are also valid for *Model 3*. However, this time degree of freedom is 3 because the soft lateral walls are modeled using an extra spring-damper and the mass of the enclosure is divided into separate parts.

State 1: When $x_2 - x_1 < 0$, the mass, stiffness, and damping matrices are,

$$M_1 = \begin{bmatrix} m + m_s/2 & 0 & 0 \\ 0 & m_s/2 & 0 \\ 0 & 0 & m_p \end{bmatrix}, \tag{3.15}$$

$$K_1 = \begin{bmatrix} k_s + k_w + k_f & -k_w & -k_f \\ -k_w & k_w & 0 \\ -k_f & 0 & k_f \end{bmatrix}, \tag{3.16}$$

$$C_1 = \begin{bmatrix} c_s + c_w + c_f & -c_w & -c_f \\ -c_w & c_w & 0 \\ -c_f & 0 & c_f \end{bmatrix}. \tag{3.17}$$

State 2: When $x_2 - x_1 > h$,

$$M_2 = \begin{bmatrix} m + m_s/2 & 0 & 0 \\ 0 & m_s/2 & 0 \\ 0 & 0 & m_p \end{bmatrix}, \tag{3.18}$$

$$K_2 = \begin{bmatrix} k_s + k_w & -k_w & 0 \\ -k_w & k_w + k_c & -k_c \\ 0 & -k_c & k_c \end{bmatrix}, \tag{3.19}$$

$$C_2 = \begin{bmatrix} c_s + c_w & -c_w & 0 \\ -c_w & c_w + c_c & -c_c \\ 0 & -c_c & c_c \end{bmatrix}. \tag{3.20}$$

State 3: When $0 \le x_2 - x_1 \le h$,

$$M_3 = \begin{bmatrix} m + m_s/2 & 0 & 0 \\ 0 & m_s/2 & 0 \\ 0 & 0 & m_p \end{bmatrix}, \tag{3.21}$$

$$K_3 = \begin{bmatrix} k_s + k_w & -k_w & 0 \\ -k_w & k_w & 0 \\ 0 & 0 & 1 \end{bmatrix}, \tag{3.22}$$

$$C_2 = \begin{bmatrix} c_s + c_w & -c_w & 0 \\ -c_w & c_w & 0 \\ 0 & 0 & 0 \end{bmatrix}. \tag{3.23}$$

Here, since the particle is in free flight, the particle is tracked separately with Equation (3.11) as in *Model 2*. Hence, the results of the third DOF of the above matrices are discarded.

3.3 Equivalent Viscous Damping Model

An equivalent viscous damping coefficient is calculated for *Model 2* and *Model 3* to estimate the energy loss in the particle bed. The damping model algorithm works as follows: When the simulation starts, a function is called to construct a trend line using spline interpolant fit for RMS acceleration vs. c_{eq} values which are derived from the tests conducted by de Melo [55]. The trend line is necessary to evaluate it for any acceleration other than test data. It is constructed once in advance and then evaluated at each RMS acceleration half-cycle to find the corresponding c_{eq}. These c_{eq} values will be used as floor and ceiling damping coefficients for the next half cycles (see Figure 7). For the first half-cycle, the c_{eq} value corresponding to the upper limit of the acceleration data is used since the simulation starts with an initial impulse excitation. Then, c_{eq} for the second half-cycle is found based on the first half-cycle data. Assuming a free decay behavior, the current method slightly overestimates the RMS acceleration

value. This may produce either a slightly high or low c_{eq}value depending on being below or above optimum acceleration, respectively. Test data spans from $0.7g$ to $7.6g$. If the RMS acceleration is outside of this range, one of the two limit values for c_{eq} is used depending on the RMS acceleration value being low or high.

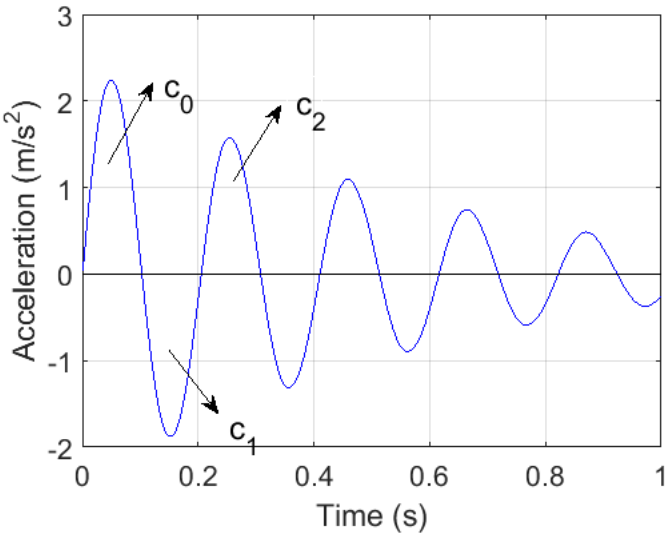

Figure 7: Time vs acceleration of the base mass.

3.4 Response Modeling

Cunefare et al. [52] presented an in-depth coverage of response modeling for LTI systems with state-switchable stiffness. Below is the derivation of response modeling equations for LTI systems with state-switchable mass, spring and damper. The state-space representation of the dynamical system described above is

$$\dot{x}(t) = A_j x(t) + B_j u(t), \tag{3.24}$$

where A_j and B_j both depends upon the system matrices. In Eq. (3.24)

$$x(t) = \begin{Bmatrix} q(t) \\ \dot{q}(t) \end{Bmatrix}, \tag{3.25}$$

is the state vector, and

$$u(t) = \begin{Bmatrix} \{0\} \\ \{Q(t)\} \end{Bmatrix}. \tag{3.26}$$

There are as many A and B matrices as the number of the states of the system but only one of them will be valid at any time, where

$$A_j = \begin{bmatrix} [0] & [1] \\ -\left[M_j^{-1}K_j\right] & -\left[M_j^{-1}C_j\right] \end{bmatrix}, \tag{3.27}$$

$$B_j = \begin{bmatrix} [0] & [0] \\ [0] & \left[M_j^{-1}\right] \end{bmatrix}. \tag{3.28}$$

The solution of the LTI system for one period of impulse excitation can be divided into two parts: (i) the time of the impulse, (ii) free response. At the time t_0 of the impulse excitation, the solution of the LTI system $\dot{x}(t) = Ax(t) + Bu(t)$ for an impulse input u is [32]

$$x(t) = e^{AT}x(t_0) + \int_{t_0^-}^{t_0^+} e^{A(t_0+T-\tau)}Bu\,d\tau\,, \tag{3.29}$$

where T is the time step of the discrete simulation. Defining

$$A_{dj} = e^{A_jT}\,, \tag{3.30}$$

and

$$B_{dj} = \left[\int_0^T e^{A_j\tau}\,d\tau\right]B_j = A_j^{-1}(A_{dj} - I)B_j\,, \tag{3.31}$$

then the iterative solution of the system response for impulse excitation is found as

$$x(k+1) = A_{dj}x(k) + B_{dj}u(k)\,, \tag{3.32}$$

where the subscript j indicates the index of the current state.

The free response solution of the LTI system with the homogeneous equation $\dot{x}(t) = Ax(t)$ from initial time t_0 to final time is

$$x(t) = e^{A(t-t_0)}x(t_0)\,. \tag{3.33}$$

The iterative solution of the system response for impulse excitation is found as

$$x(k+1) = A_{dj}x(k)\,. \tag{3.34}$$

At each time step k, the next state vector can be computed through Eq. (3.32) or Eq. (3.34) depending on whether it is an excitation time or not.

3.5 Metric of Performance

There are various methods to measure damping performance of the PIDs in the literature. Duncan et al. [28] quantified the effectiveness of the PID by

$$\eta = \frac{\sigma_{undamped}}{\sigma_{damped}}\,, \tag{3.35}$$

where η is the displacement ratio, $\sigma_{undamped}$ is the standard deviation of the position of the structure without an impact damper, and σ_{damped} is the standard deviation of the position of the structure with an impact damper. While comparing *Model 1* results with [28], the same method is followed. $\eta > 1$, $\eta < 1$ and $\eta = 1$ correspond to increased effectiveness, decreased effectiveness and no impact, respectively.

Friend and Kinra [26] states that PID systems are able to achieve high damping by absorbing the *kinetic energy* of a structure, while traditional viscoelastic dampers convert the elastic strain energy stored to heat. Therefore, a velocity-based metric would be more appropriate than a displacement-based metric. For this reason, the metric of performance was defined to be

$$\psi = \frac{(v_{rms})_{noPID}}{(v_{rms})_{PID}}\,, \tag{3.36}$$

where $(v_{rms})_{noPID}$ is the RMS velocity of the base mass without an impact damper, and $(v_{rms})_{PID}$ is the RMS velocity of the base mass with an impact damper. $\psi > 1$, $\psi < 1$ and $\psi = 1$ correspond to increased effectiveness, decreased effectiveness and no impact, respectively.

The dimensionless parameters used can be seen in Table 1. In Table 1, ω is the impulse excitation frequency, and $\omega_n = \sqrt{k_s/m}$ is the natural frequency.

Table 1: Dimensionless parameters

Parameter	**Value**
Dimensionless displacement, x'	$x' = x/h$
Mass ratio, m'	$m' = m_p/m$
Structural damping ratio, c'	$c' = c/2\sqrt{k_s m}$
Dimensionless gap clearance, h'	$h' = h{\omega_n}^2/g$
Dimensionless forcing amplitude, f'	$f' = F/(mg)$
Frequency ratio, ω'	$\omega' = \omega/\omega_n$

3.6 Simulation Results

When the simulation starts, the particle is located on the enclosure floor, and the system is at the static equilibrium position. At time $t = 0$, an impulsive force is applied, which gives an initial velocity to the system. Figures 8-10 are sample time plots from *Model 2* where the floor and ceiling of the enclosure is resilient.

Figure 8 plots the motion of the floor, ceiling, and particle for the undamped case, after initial impulse excitation at $t = 0$. Here, both c' and m' equal to zero. As a result, particle

motion is hypothetical. Since there is no damping factor, energy is conserved and all of the cycles have the same amplitude.

Figure 9 shows the time simulation plot with the same parameters as in Figure 8, except $c' = 0.01$. The amplitude decrement of the cycles indicates that the damper slowly dissipates mechanical energy. Figure 10 shows the time simulation plot for $m' = 0.1$ and $c' = 0.01$. The resilience of the enclosure floor and ceiling is evident in Figure 10 where both resilient and hypothetical rigid paths of the floor and the ceiling are plotted. When the particle displacement is above the displacement of the hypothetical rigid ceiling or below the displacement of the hypothetical rigid floor paths, it means the ceiling or the floor is compressed, respectively. The amplitude decrement is higher than the previous cases this time, because the damping effect of the particle impact is added to the dissipation mechanism. Note that the amplitude of the last peak in Figure 10 is lower than the amplitude of the last peak in Figure 9 which shows the greater amplitude decrement for the former.

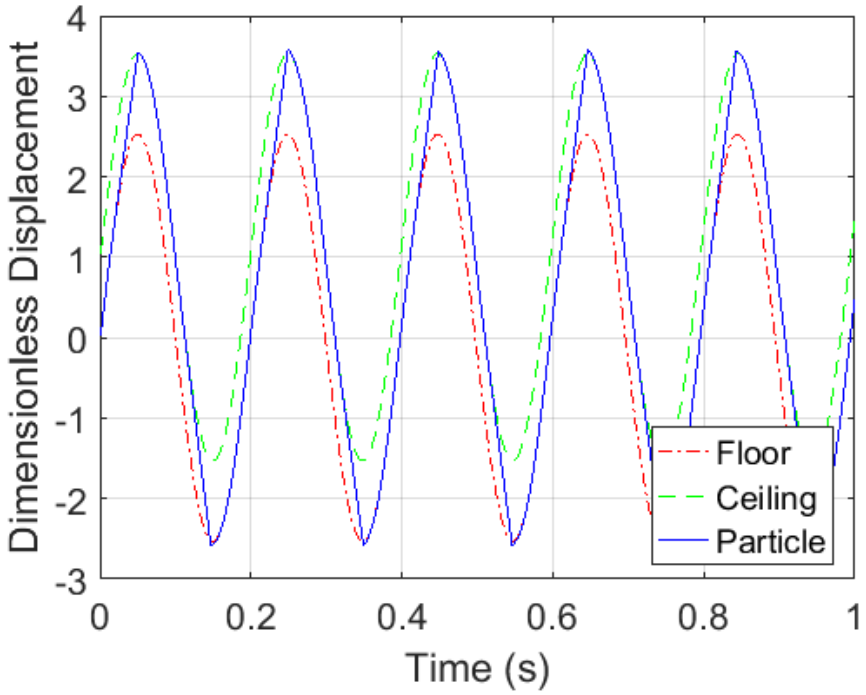

Figure 8: Time simulation plot for $m' = 0$ and $c' = 0$.

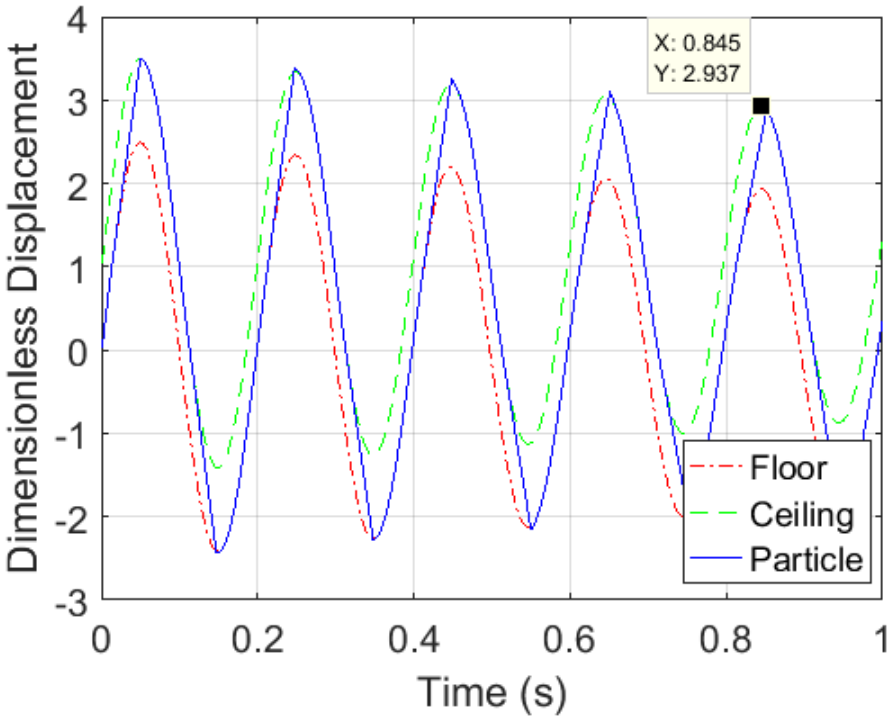

Figure 9: Time simulation plot for $m' = 0$ and $c' = 0.01$.

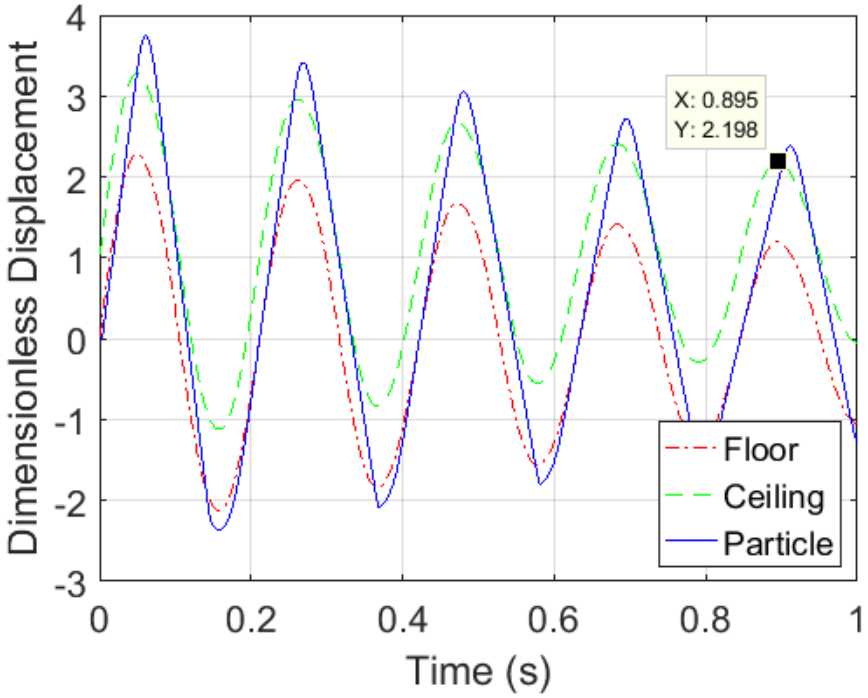

Figure 10: Time simulation plot for $m' = 0.1$ and $c' = 0.01$.

Figure 11 shows the time simulation plot for periodic impulse excitation where the frequency ratio is $\omega' = 1$. Periodic cyclic behavior indicates that the initial transients are diminished in this time range. Time simulation results for varying parameter values show that initial transients die out after the first 25 cycles. Therefore, for the damping calculations, the first 25 cycles are neglected and the data of next 100 cycles are collected in order to avoid the effect of initial transients.

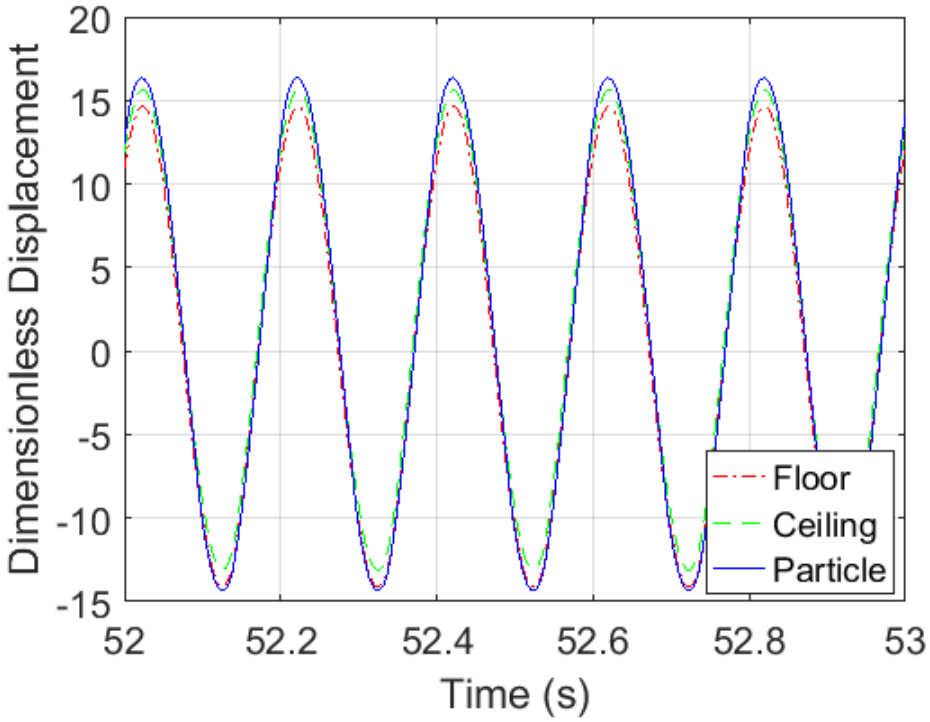

Figure 11: The time simulation plot for periodic impulse excitation for a time period after all initial transients have died out, where $\omega' = 1$.

3.6.1 Comparison of Model 1 Results with Literature

Duncan et al. [28] modeled a vertical impact damper system shown in Figure 12. The modeled system has a base oscillating sinusoidally with amplitude, a, and radian frequency, ω. To compare *Model 1* results with [28], a sinusoidal force with amplitude, F, is used. The conversion between the two approaches can be achieved by,

$$F = -m_s a \omega^2. \tag{3.37}$$

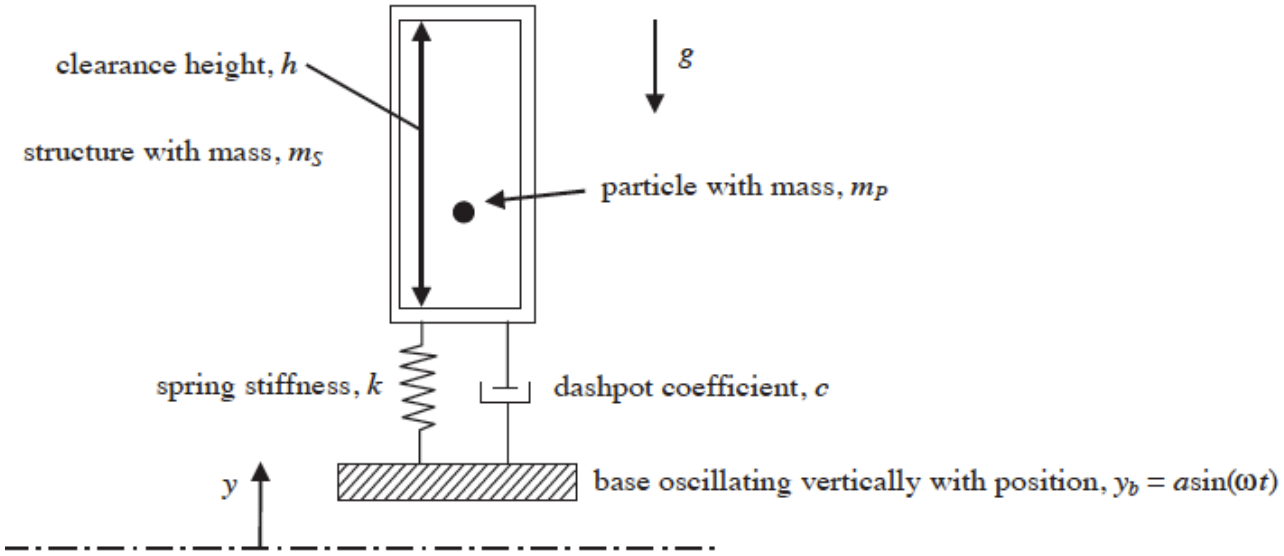

Figure 12: The schematic of the modeled impact damper system of Duncan et al [28].

Figure 13 shows the PID effectiveness comparison of *Model 1* results with [28] as a function of dimensionless base amplitude. The parameter values used can be seen in Table 2. The same simulation time step $\Delta t = 1.0 \times 10^{-5} s$ is used for all 3 cases. To avoid initial transients, 100 oscillations are averaged excluding the first 25 cycles. Both displacement ratio and velocity ratio metrics are in good agreement with Duncan et al.'s results. This shows that, displacement and velocity ratio can be used interchangeably when both are averaged over a large time.

Table 2: Model 1 parameters

Parameter	**Value**
Mass ratio, m'	0.05
Damping ratio, c'	0.05
Gap clearance, h'	50
Structural stiffness, k_s	1000 (N/m)

Base mass, m	1.0 (kg)

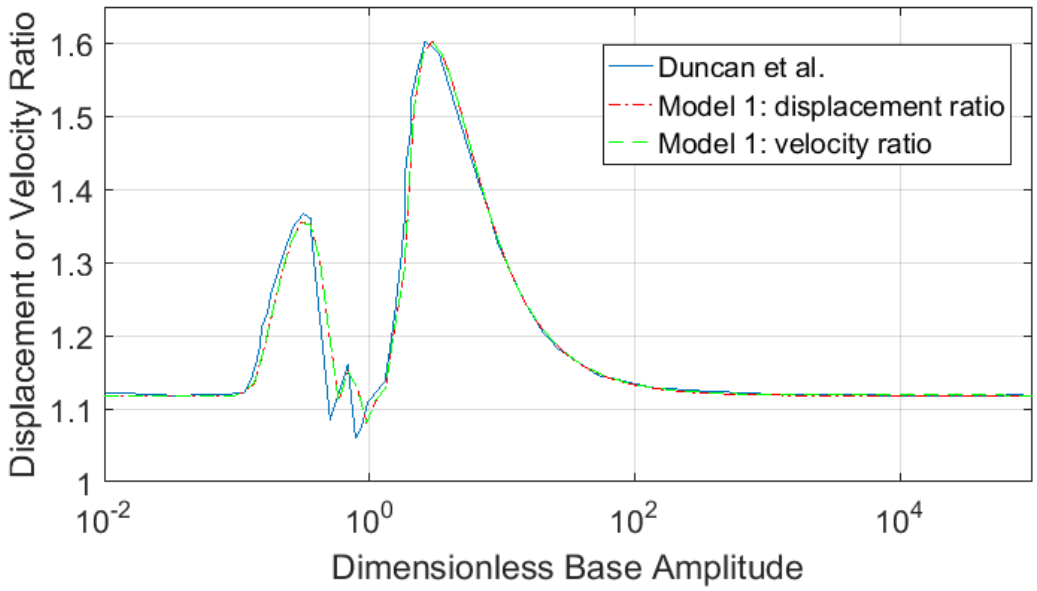

Figure 13: PID effectiveness comparison with Duncan et al. as a function of dimensionless base amplitude.

To diminish the potential for discontinuities in the response, the time step has to be short with respect to the shortest period of any of the forced and natural response frequencies of the system [53]. However, analysis results showed that using very small time step such as $\Delta t = 1.0 \times 10^{-5} s$ is computationally inefficient and the run time is inversely proportional to the time step. For the parameters in Figure 13, highest frequency in the system is 5.03 Hz, and the shortest period is $1.99 \times 10^{-1}\ s$. Typically, selecting the time step to be 1/100th or less of the shortest period is desirable, which is $1.99 \times 10^{-3}\ s$ for this case. Figure 14 compares two time step values above and below $1.99 \times 10^{-3}\ s$ for the same parameters in Figure 13. The fine time step is $\Delta t = 1.0 \times 10^{-5} s$, whereas the coarse time step is $\Delta t = 1.0 \times 10^{-2} s$. There are 2 main differences between the two curves. First, the simulation with the fine time step has the same velocity ratio for very high and low base amplitudes. On the other hand, the simulation with the

coarse time step asymptotically approaches to a higher velocity ratio value for high base amplitudes. Second, velocity ratio with fine time step is always greater than 1, meaning increased damping for any base amplitude value, however coarse time step can cause velocity ratio to be less than 1 for dimensionless base amplitudes at around 10^{-1}. These differences are numerical inaccuracies resulting from the coarse time step. Considering the tradeoff between computation time and accuracy, the coarse time step is selected because the general behaviors of the two cases are very close to each other both in base amplitude and velocity ratio. So, simulation results are not affected significantly.

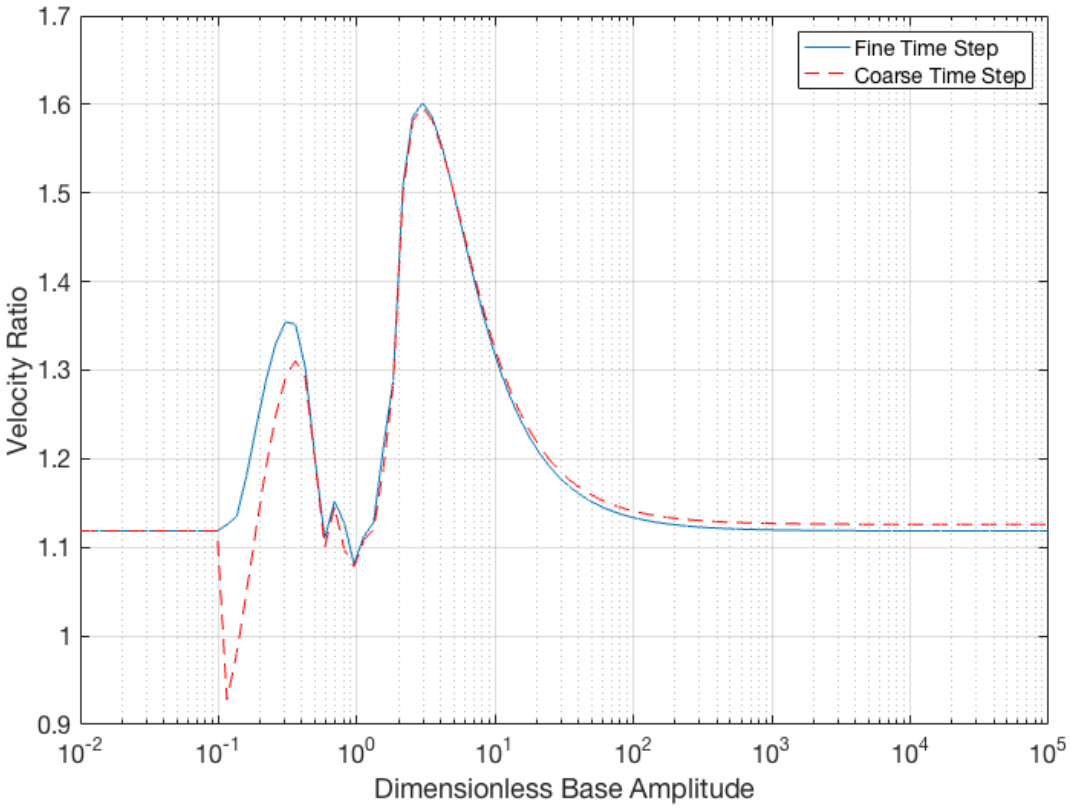

Figure 14: Time step comparison of *Model 1*. Velocity ratio as a function of dimensionless base amplitude.

Figure 15 shows the maximum PID effectiveness comparison as a function of the mass ratio. By PID effectiveness, both displacement ratio and velocity ratio are meant. Maximum

damping value increases almost linearly with increasing mass ratio in the given range. Displacement ratio and velocity ratio results of *Model 1* are in good agreement with Duncan et al.'s results.

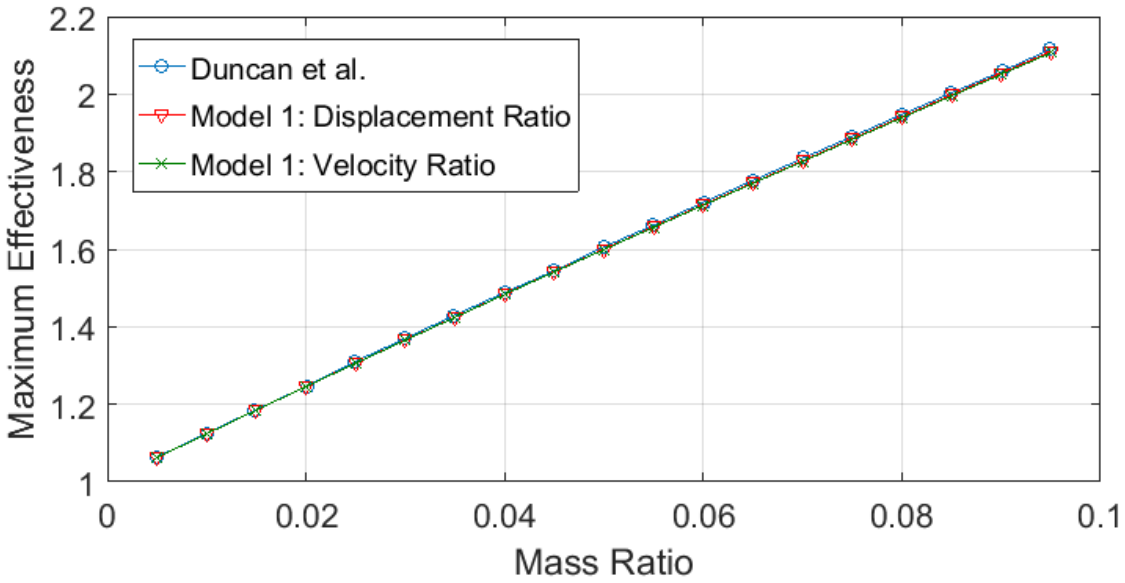

Figure 15: Maximum PID effectiveness comparison with Duncan et al. as a function of the mass ratio.

Figure 16 compares displacement ratios of 4 different gap clearances as a function of dimensionless base amplitude. Data with markers are results from *Model 1* and data with starred labels are from Duncan et al. Both results are very similar. Velocity ratio results were also in good agreement with both plots and omitted because of visual simplicity. The dimensionless gap clearance, h', values are 10, 50, 90, and infinity. As h' increases, the optimum displacement ratio regions shifts toward higher dimensionless base amplitudes. This was expected because maximum effectiveness occurs when particle collides with both the enclosure ceiling and the floor. Increasing gap clearance requires more force to induce particle-ceiling impact. Note that optimum region for h' at infinity is not available in the plot because it occurs when the force is at infinity. Maximum displacement ratio increases as the gap clearance increases.

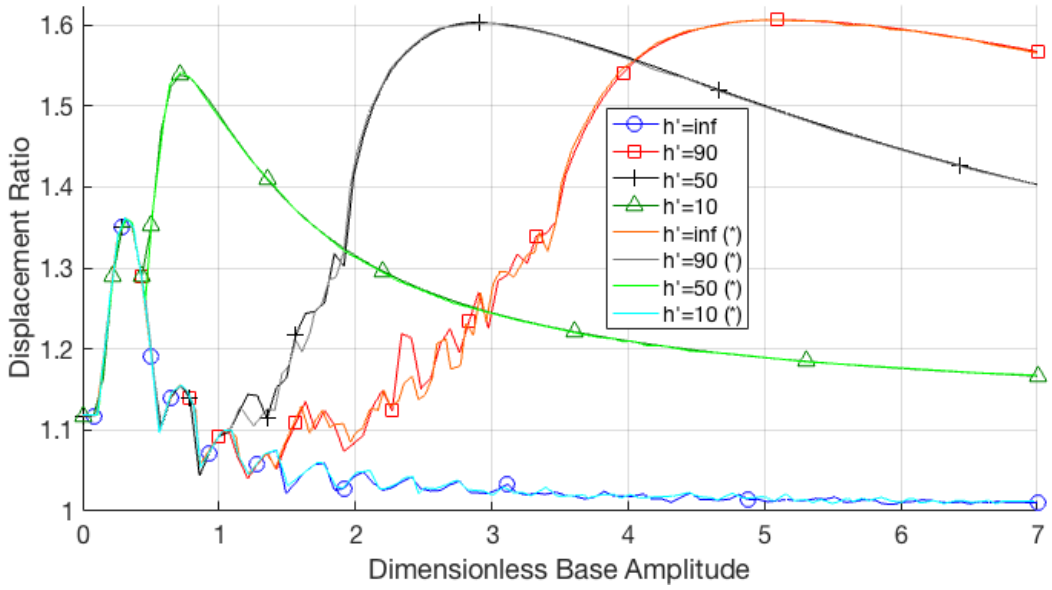

Figure 16: Gap clearance comparison with Duncan et al. as a function of dimensionless base amplitude. Data with markers are results from *Model 1*. Data with starred labels is from Duncan et al.

To summarize the results from this section, *Model 1* is compared with Duncan et al.'s vertical impact damper model under harmonic excitation. Results demonstrated the validity of treating PIDs as state-switched devices and using LTI simulation methods for response modeling. Velocity ratio is introduced as a new performance metric, which is defined as the ratio of RMS velocity of the base mass without an impact damper to the RMS velocity of the base mass with an impact damper. When averaged over a large time interval, displacement and velocity ratio can be used interchangeably.

3.6.2 Model 2 vs. Model 3

Model 2 and *Model 3* uses the same spring-damper method except *Model 3* uses an extra pair of spring-damper to model the soft lateral walls. In fact, *Model 2* is a special case of *Model 3* where the wall spring stiffness value goes to infinity. However, using very high stiffness values also increases the maximum frequency in the system, which would decrease the simulation time

step needed to resolve that frequency. Therefore, 2 different models are considered and discussed if there is a need for extra complexity for optimum damping. Figure 17 shows the maximum velocity ratio variation of *Model 3* as a function of the lateral wall stiffness. The parameter values used can be seen in Table 3. The x-axis is given as the ratio of the lateral wall stiffness to the stiffness of the structure, which is a dimensionless stiffness term. As the wall stiffness with respect to the stiffness of the structure increases, maximum velocity ratio also increases first and staying nearly constant after some point. This shows that high lateral wall stiffness value is desirable in terms of optimum damping. Besides, tested PIDs had very thick lateral walls, which can be assumed rigid. Therefore, the simulations are continued with *Model 2*.

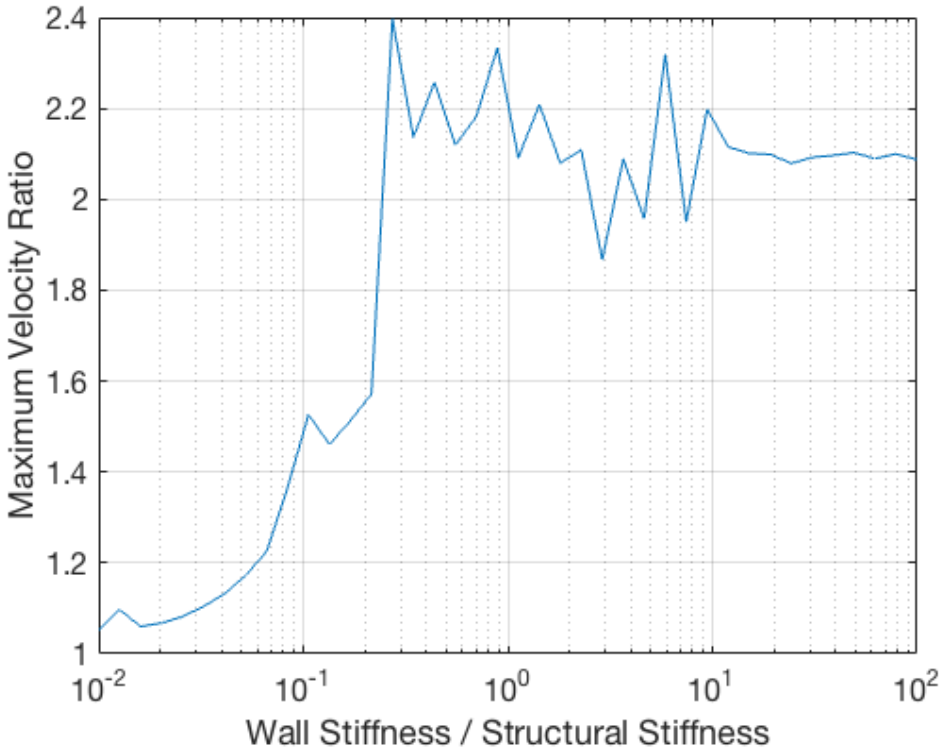

Figure 17: Maximum velocity ratio variation of *Model 3* as a function of the lateral wall stiffness.

Table 3: Model 2 and Model 3 parameters

Parameter	**Value**
Mass ratio, m'	0.05
Structural damping ratio, c'	0.05
Gap clearance, h'	50
Structural stiffness, k_s	1000 (N/m)
Floor stiffness	1.0 k_s
Damping coefficient of walls	0.0 (Ns/m)
Time step	1.0×10^{-4} (s)

3.6.3 Effect of the Limit Stop

Figure 18 shows the effect of using limit stop on the velocity ratio. With and without the limit stop simulations follow the same trend for low forcing amplitudes. Increasing the forcing amplitude activates the limit stop condition and after approximately $f' = 2$, the two plots differ. The simulation with the limit stop approaches to a higher velocity ratio value than the other as forcing amplitude goes to infinity. Note that both plots have the same maximum velocity ratio at the same forcing amplitude so that using limit stop does not affect the optimum forcing amplitude and the resultant effectiveness.

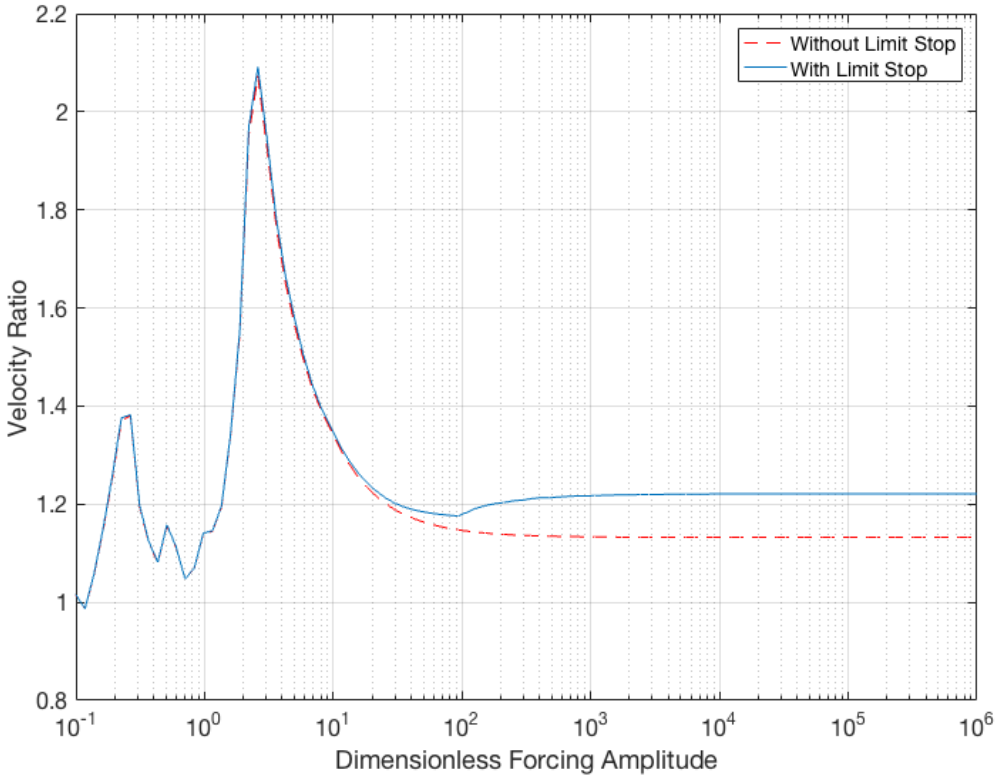

Figure 18: Effect of the limit stop on the velocity ratio.

3.6.4 Effect of Forcing Amplitude

The effect of the forcing amplitude on the velocity ratio is shown in Figure 19. For small forcing amplitudes, the particle stays in contact with the floor. Increasing the forcing amplitude results in a higher acceleration of the enclosure (both in the positive direction, and in the negative direction), allowing the separation conditions to be met. As a result, particle-floor impacts occur, and the velocity ratio increases. Velocity ratio reaches its maximum when both particle-floor and particle-ceiling impacts exist (when $f' = 2.5$). As the forcing amplitude is further increased, the velocity ratio decreases.

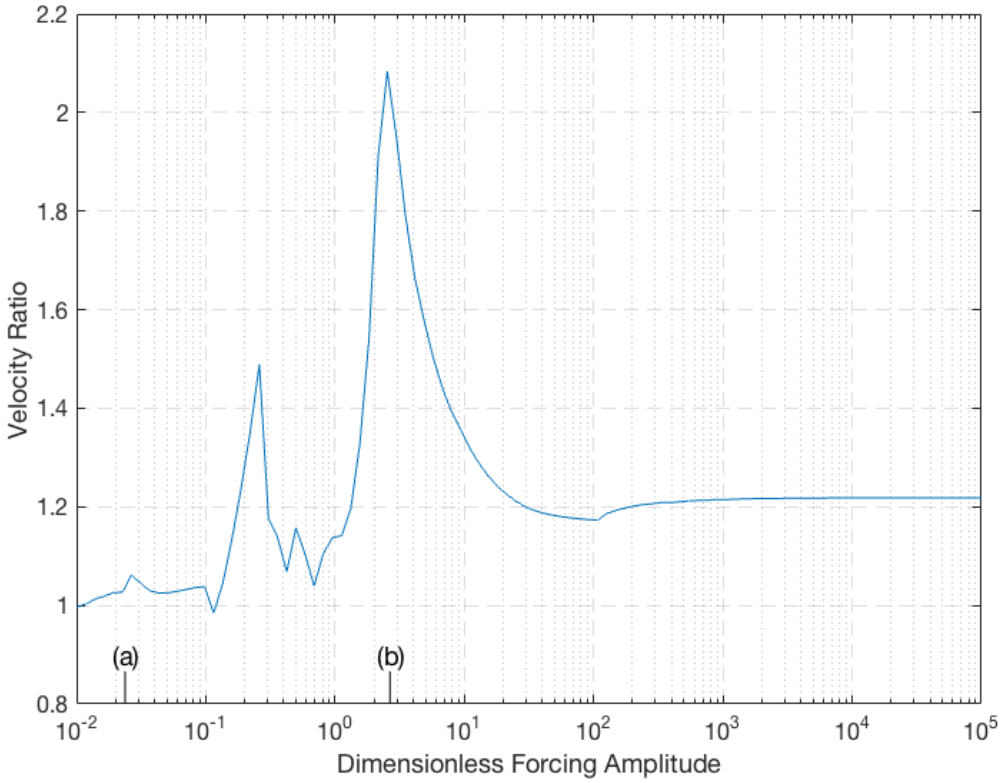

Figure 19: Velocity ratio vs. dimensionless forcing amplitude. (a) Ground separation. (b) Ceiling impacts start to occur.

3.6.5 Effect of Forcing Frequency

Figure 20 shows the relationship between the velocity ratio variation and the frequency ratio (ω') under periodic impulse excitation with fixed forcing amplitude ($f' = 4$). For very high and low ω' values, velocity ratio stays constant just above 1. In between $\omega' = 10^{-1}$ and $\omega' = 1$, an oscillatory behavior was observed on the velocity ratio. The same interval was run with a fine time step, $1.0 \times 10^{-5}s$, and the results were similar (see Figure 21). For comparison, Figure 22 shows the velocity ratio variation under harmonic excitation as a function of dimensionless frequency. Harmonic excitation does not have the same oscillatory behavior but a single effective region around $\omega' = 1$. When the time plots were investigated, increased and decreased velocity ratio values are the results of the impulse excitation time with respect to the particle-

enclosure impacts. For example, Figure 23 shows the time vs. dimensionless displacement plot for $\omega' = 0.5351$ and velocity ratio, 1.516. Velocity ratio is relatively high because when the particle is about to collide with the enclosure floor, impulse force is also exerted at the same time (see Time=52.31 s). This significantly increases the relative momentum change of the structure. Cheng and Wang [34] reported that the reduction of the vibration response primarily depends on the collision that occurs while the particle mass and the main mass are moving toward each other. On the other hand, time vs. dimensionless displacement plot for a relatively low velocity ratio (0.8681) can bee seen in Figure 24. For $\omega' = 0.5351$, impulse force is applied at the same time with particle – ceiling impact (see Time=52.55 s). Since they were moving in the same direction, the relative momentum change of the structure is low.

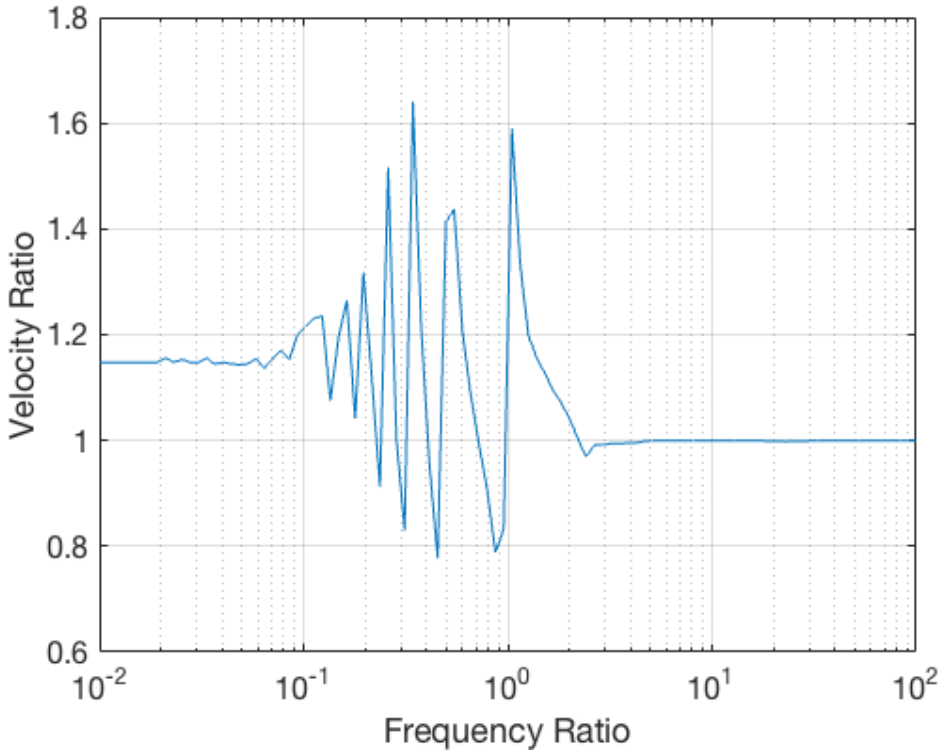

Figure 20: Velocity ratio variation under periodic impulse excitation as a function of the frequency ratio.

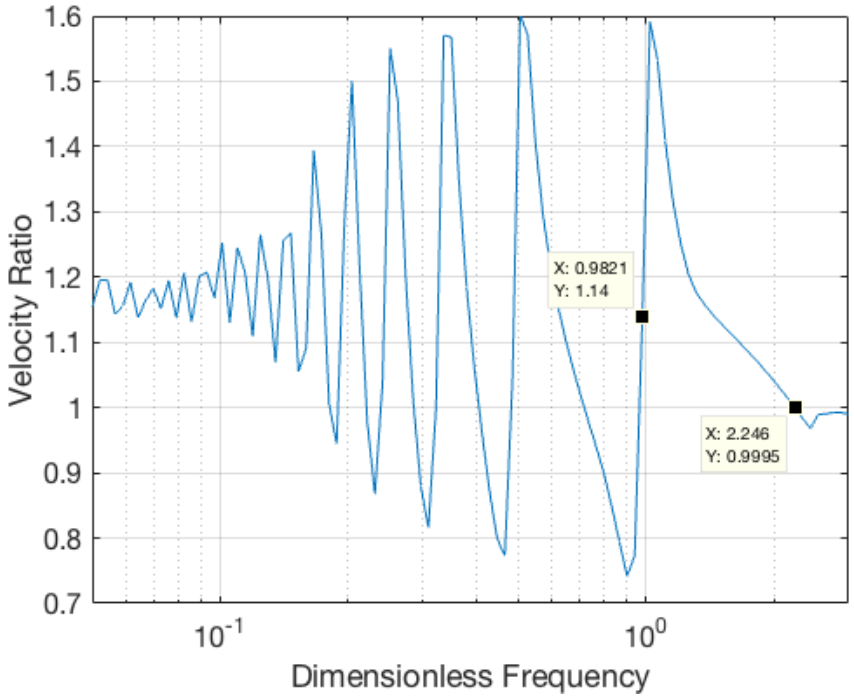

Figure 21: Velocity ratio variation under periodic impulse excitation as a function of dimensionless frequency with fine time step.

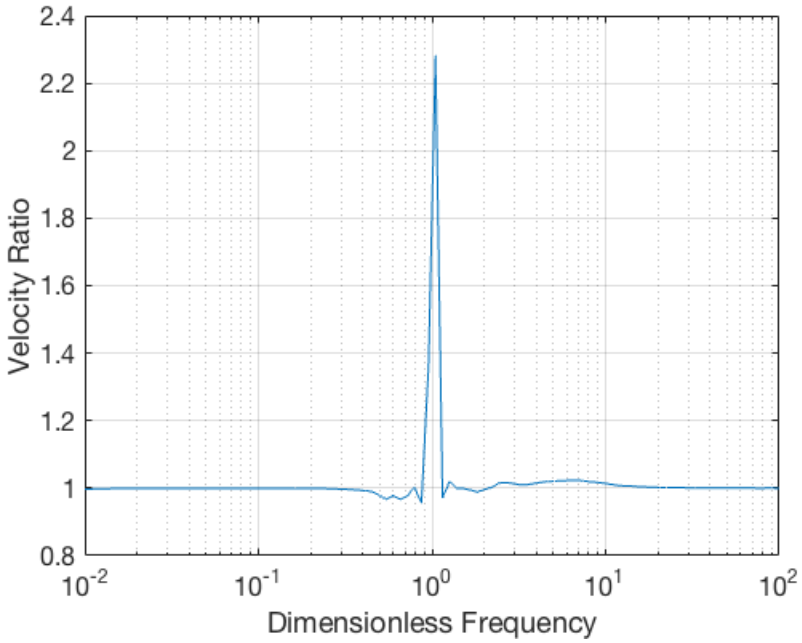

Figure 22: Velocity ratio variation under harmonic excitation as a function of dimensionless frequency.

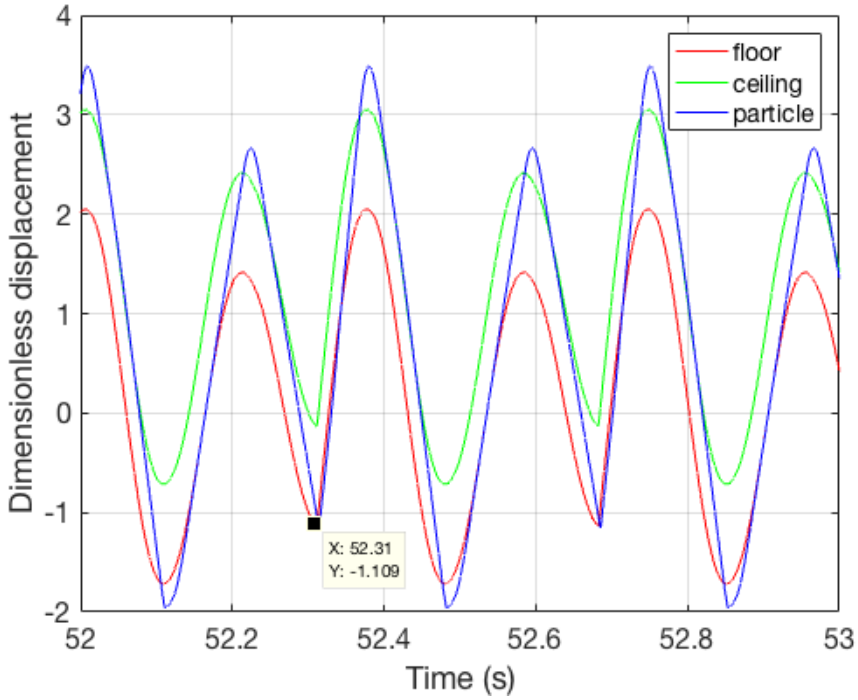

Figure 23: Time vs. dimensionless displacement plot for $\omega' = 0.5351$ and velocity ratio, 1.516.

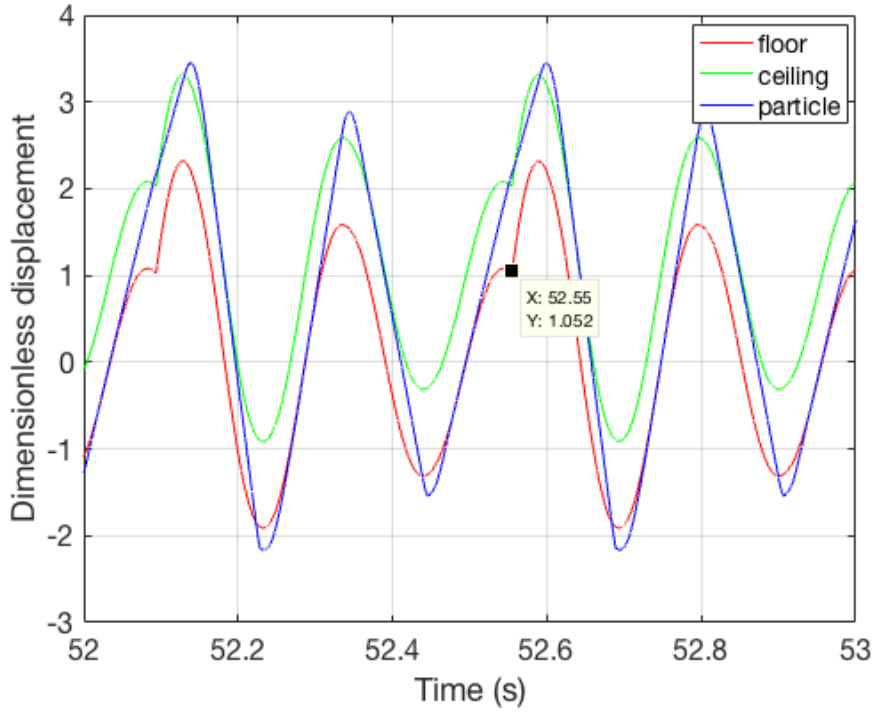

Figure 24: Time vs. dimensionless displacement plot for $\omega' = 0.4314$ and velocity ratio, 0.8681.

From Figure 20 and Figure 21, it can be concluded that for best damping performance, the frequency ratio should be slightly larger than 1 ($\omega' > 1$). This means the natural frequency of the structure should be less than the impulse-repetition frequency. This may also mean that if there are multiple excitations with different frequencies, or if the frequency of the excitation changes over time, dampers with a distribution of frequencies would be more desirable for a robust solution. As a result, when designing the PID, an appropriate stiffness value for the enclosure floor could be chosen to give best damping performance.

3.6.6 Effect of Mass Ratio

Figure 25 shows the maximum velocity ratio as a function of the mass ratio under periodic impulse excitation. As the mass ratio increases, maximum velocity ratio also increases. Figure 25 confirms that the mass ratio should be limited for the optimization process; otherwise a higher mass ratio will always increase the damping.

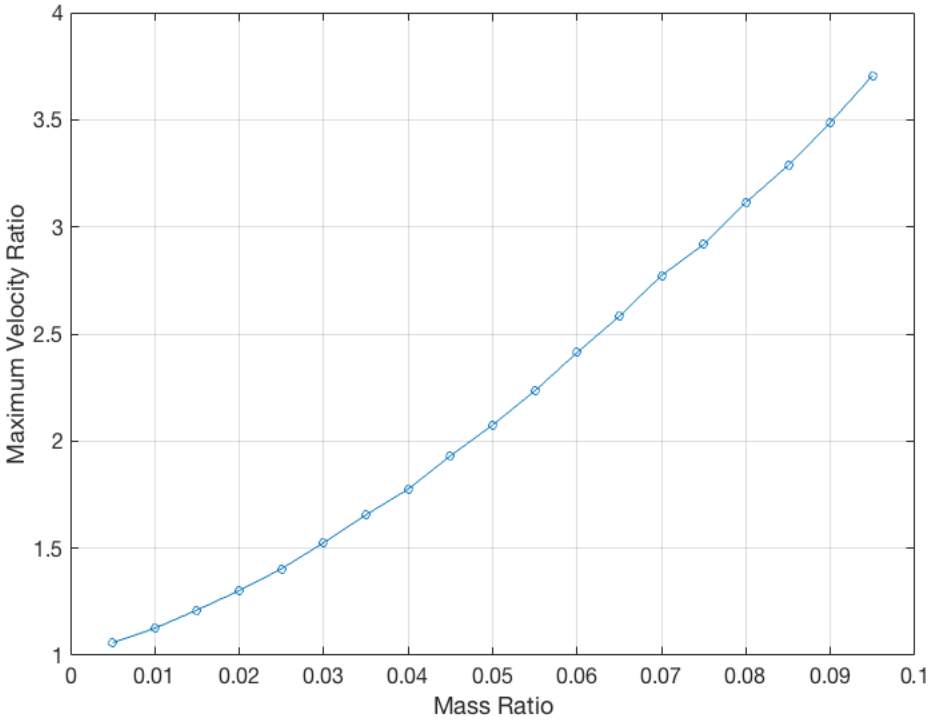

Figure 25: Velocity ratio variation as a function of the mass ratio.

3.6.7 Effect of Gap Clearance

Figure 26 compares displacement ratios of 4 different gap clearances under periodic impulse excitation as a function of dimensionless forcing amplitude. The dimensionless gap clearance, h', values are 10, 50, 90, and infinity. As h' increases, maximum velocity ratio and f' at which maximum damping occurs also increases. Note that optimum region for h' at infinity is not available in the plot because it occurs when the force is at infinity. The same gap clearances under harmonic excitation also presented in Figure 27 for comparison. The trends are similar but f' values for maximum damping are different as well as the shape of the curves.

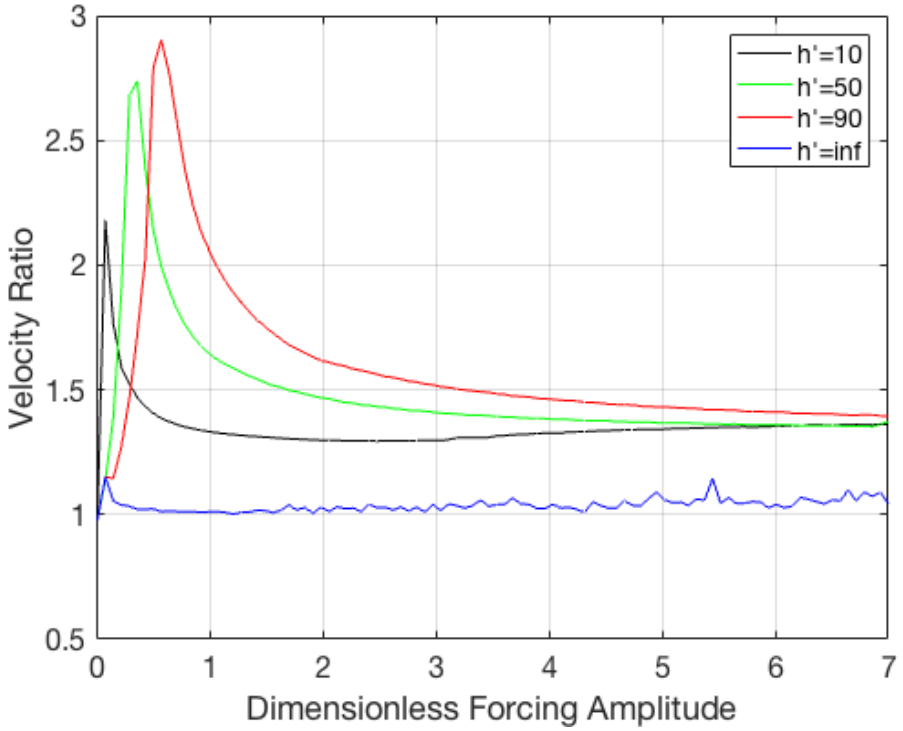

Figure 26: Gap clearance comparison under periodic impulse excitation as a function of dimensionless forcing amplitude.

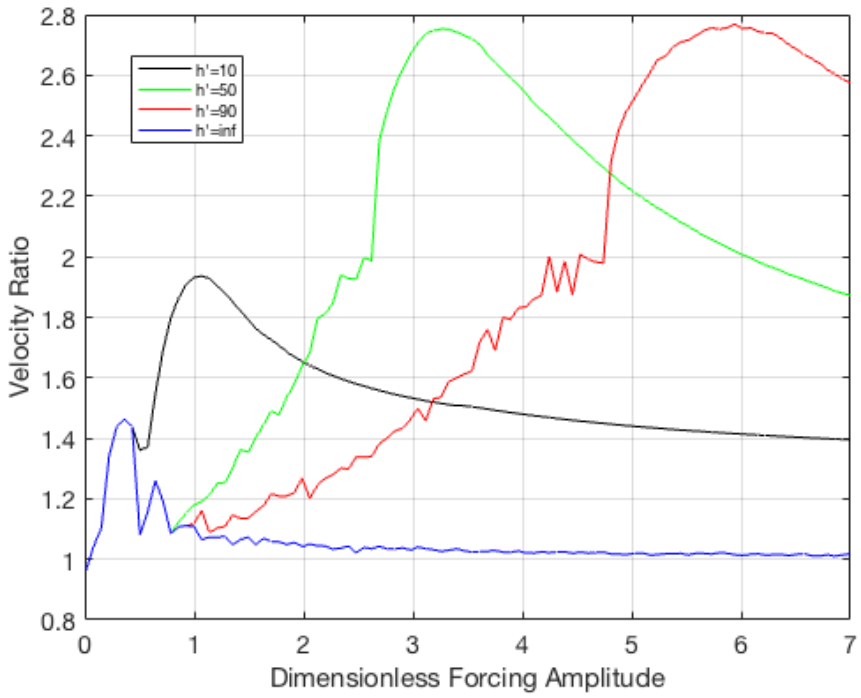

Figure 27: Gap clearance comparison under harmonic excitation as a function of dimensionless forcing amplitude.

Maximum velocity ratio variation as a function of dimensionless gap clearance is plotted in Figure 28. This plot shows that, as h' increases, maximum velocity ratio increases but also approaches a limiting value. The deviations are numerical inaccuracies resultant from the coarse time step.

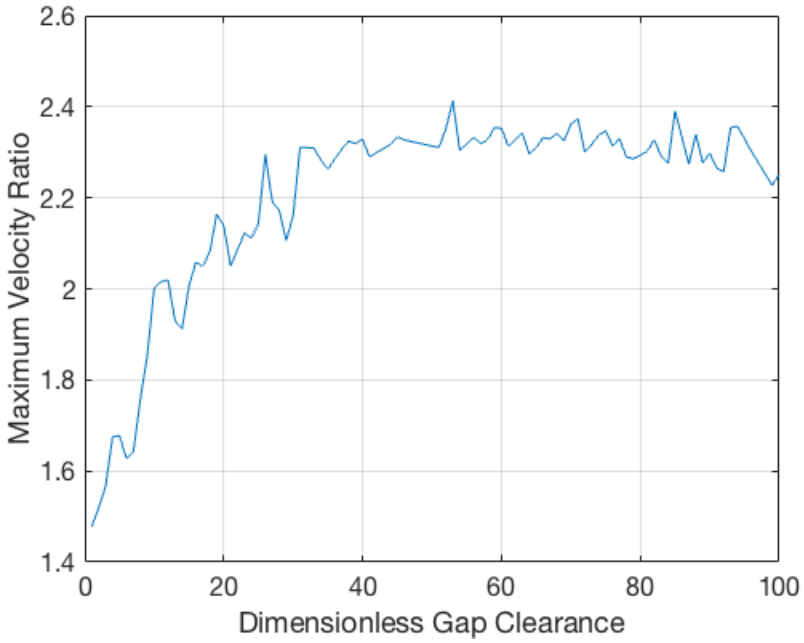

Figure 28: Maximum velocity ratio variation as a function of dimensionless gap clearance.

3.6.8 Effect of Structural Damping

Maximum velocity ratio variation as a function of structural damping ratio, c', is shown in Figure 29. As c' increases maximum velocity ratio decreases. This is because velocity ratio is a relative metric between the systems with and without the impact damper. The system without the impact damper has only structural damping as an energy dissipation mechanism and as c' increases, structural damping becomes more dominant with respect to particle damping for the system with the impact damper.

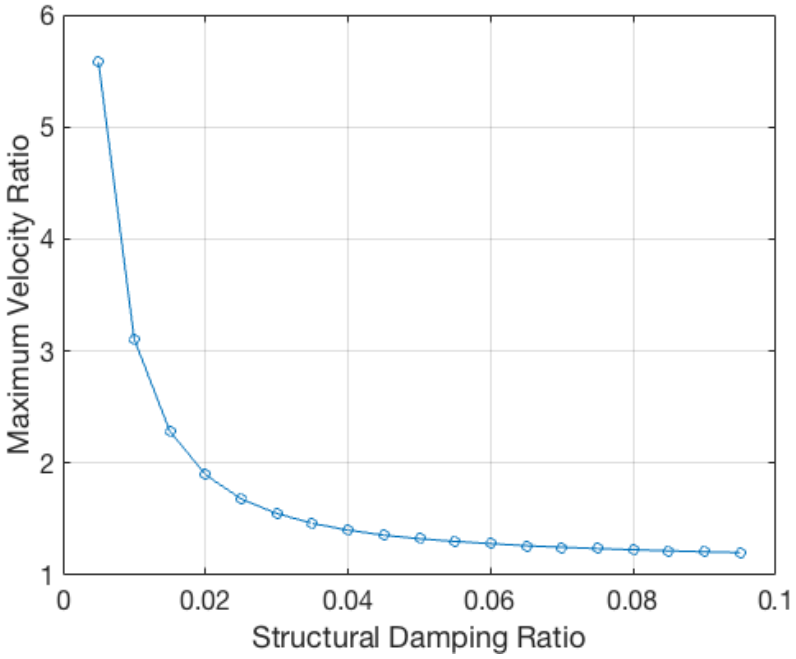

Figure 29: Maximum velocity ratio variation as a function of structural damping ratio, c'.

3.6.9 Effect of Impulsive Forcing Type and Duration

Ideally, the impulse force is assumed to be applied instantaneously. However, in reality it takes finite amount of time to apply the force. In Figure 30, the effect of the duration of the force is analyzed. For all cases, magnitude of the impulse force ($F.\delta t$) is kept constant. As the duration increased, the height of the force is decreased to keep the area of the rectangle or supplied energy constant. For the given parameters in Table 3, and time step $1.0 \times 10^{-3}s$, impulse force is applied at the beginning of every 199 time steps. The duration of the force is varied between 10 time steps to 100 time steps. As the forcing duration increases, maximum velocity ratio decreases and f' for maximum effectiveness increases. This means as the forcing duration increases, higher force is needed for the maximum effectiveness and that effectiveness value is lower with respect to the shorter forcing duration.

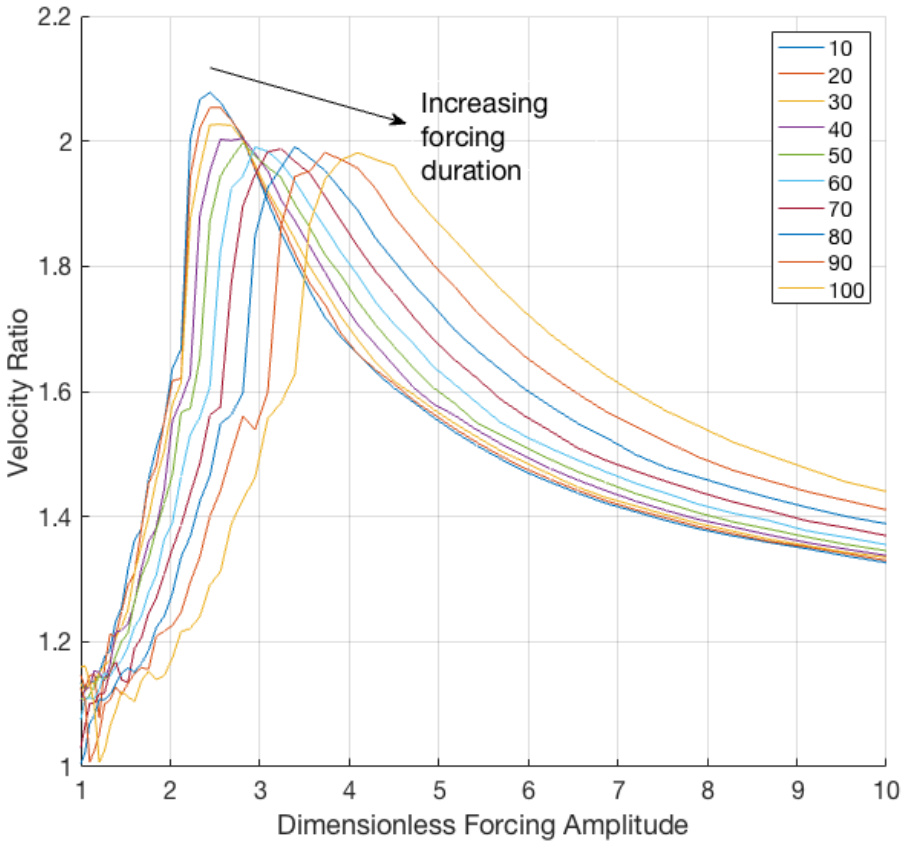

Figure 30: Forcing duration comparison for rectangular impulsive force. Time step is varied between 10-100.

Figure 31 shows forcing duration comparison for a triangular impulsive force. As an example, binomial coefficients are used as the amplitudes of the forces at each time step. Again, $F.\delta t$ is kept constant and the time step number is varied between 10-100. There is no significant difference between the plots. Considering both Figure 30 and Figure 31, it can be concluded that if the force is not distributed evenly but accumulated mostly around half of the forcing duration time, the same analysis results are valid with the impulse force that is applied in a single time step.

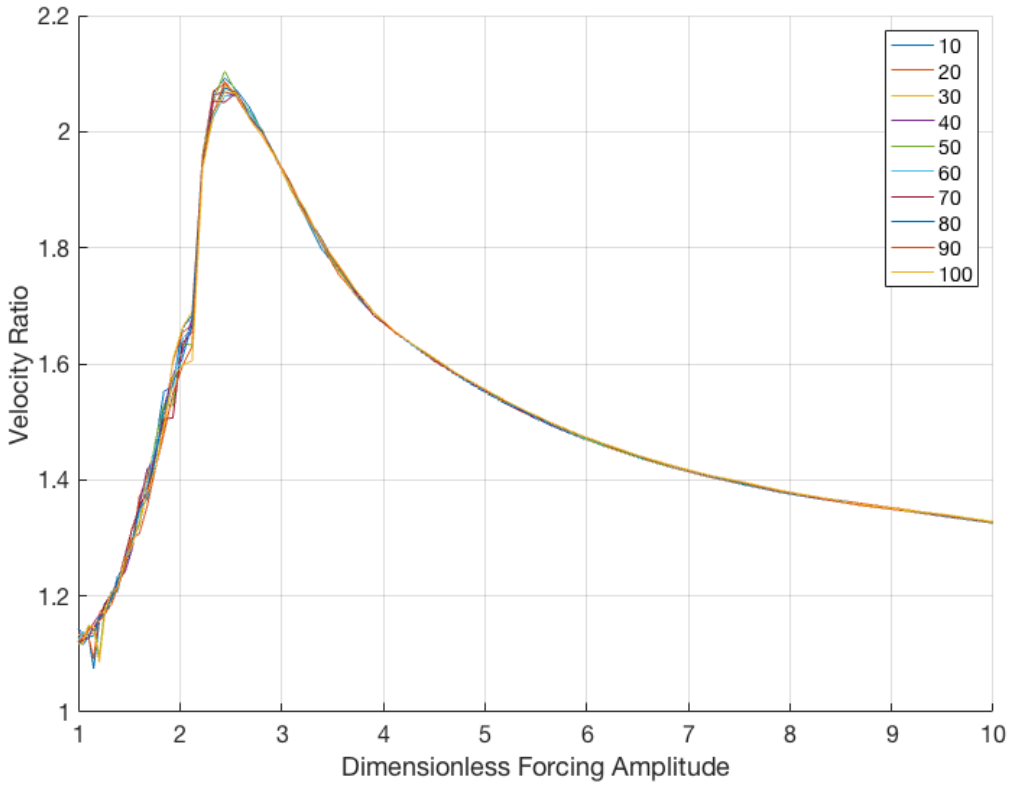

Figure 31: Forcing duration comparison for a triangular impulsive force. Time step is varied between 10-100.

CHAPTER 4

DISTRIBUTED ARRAY OF RESILIENT PARTICLE IMPACT DAMPERS ON A BEAM UNDER PERIODIC IMPULSE EXCITATION

4.1 Overview

This chapter develops analysis techniques for the distributed array of resilient PIDs attached to a beam under periodic impulse excitation. The chapter begins with the development of the equations of motion of a general beam/mass system. The method of assumed modes is used to model the transverse displacement field on the beam and Lagrange's equations are used to express the kinetic and potential energy of the beam and attached masses. Then, specific assumed mode basis functions are considered for a cantilever beam to identify the elements of the mass and the stiffness matrices. Rayleigh's dissipation function is used to construct the damping matrix. Finally, various simulation results are shown to characterize the PID effectiveness attached to a cantilever beam.

4.2 Methodology

4.2.1 Equations of Motion for a Cantilever Beam with Attached PIDs

The PID system is shown in Figure 32. Both the ceiling and the floor of the enclosures are assumed to be made of a soft material such as silicone rubber [19], so that the PID floor and ceiling are attached to the enclosure with a spring and a damper. Since the compressional length of the floor and ceiling is limited due to the thickness of the material, there is a limit stop between the enclosure and the floor and between the enclosure and the ceiling.

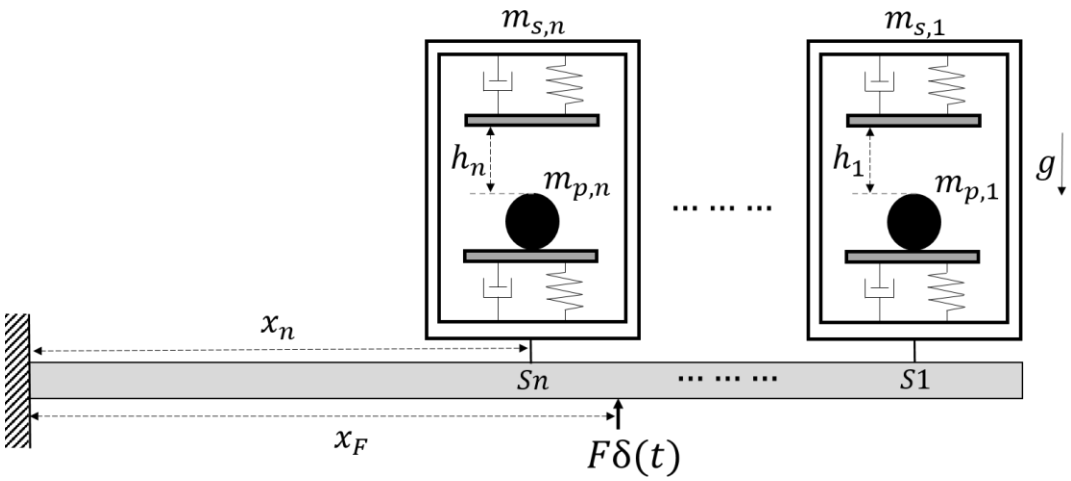

Figure 32: A schematic of the modeled cantilever beam with an array of PIDs. ($m_{s,n}$: mass of the nth enclosure, $m_{p,n}$: mass of the nth particle, h_n: nth gap clearance, x_n: nth PID location along the length of the beam, x_F: forcing location, Sn: nth spot on the beam starting from the free end, $F\delta(t)$: impulse force).

The general form of the equations of motion is the same as given in Chapter 3,

$$M\ddot{q} + C\dot{q} + Kq = Q\ , \tag{4.1}$$

where M, C and K are the mass, damping and stiffness matrices, respectively, Q is a vector of forces, q is a vector of physical or generalized coordinates. Mass, stiffness and damping are the state-switchable terms, and the number of states is equal to the number of equations of motion,

$$\begin{matrix} M_1\ddot{q} + C_1\dot{q} + K_1 q = Q \\ \cdots \\ M_{sN}\ddot{q} + C_{sN}\dot{q} + K_{sN} q = Q \end{matrix}\ . \tag{4.2}$$

where subscript sN indicates the state number. According to the method of assumed modes, the transverse displacement field on the beam is represented as

$$w(x,t) = \sum_{i=1}^{N} \varphi_i(x) q_i(t) = \varphi^T q\ , \tag{4.3}$$

where N is the number of assumed modes, φ are assumed mode basis functions, x is longitudinal position, q are generalized coordinates, t is time and superscript T stands for the transpose operation.

For notational consistency, q are used as generalized coordinates for all DOFs including those for PIDs attached to the beam. For example, if there are N modes in the expansion, plus two attached PIDs, then

$$q = \{ q_1 \ \cdots \ q_N \ q_{N+1} \ q_{N+2} \}^T . \tag{4.4}$$

In Eq. (4.4), the first N q's are the coordinates associated with the beam motion, while the last two are the coordinates related to the PID displacements.

Indicial notation is used to indicate differentiation with respect to the index in the following. If the beam has mass per unit length $m_b(x)$, and NA discrete PIDs attached, then using Lagrange's equation, the kinetic energy for the beam and attached masses may be expressed as

$$T = \frac{1}{2}\int_0^L m_b(x) w_t^2 dx + \frac{1}{2}\sum_{i=N+1}^{N+NA} \left[m_{p,i} q_{t,i}^2 + m_{s,i} w_t(x_i,t)^2 \right]. \tag{4.5}$$

In Eq. (4.5), the x_i are the physical locations of the attachment points along the length of the beam, and the $m_{p,i}$ and $m_{s,i}$ are the masses of the particles and enclosures of the PIDs, respectively. Using the assumed modes expansion for the transverse displacement field, w yields

$$T = \frac{1}{2}\sum_{i=1}^{N}\sum_{j=1}^{N} q_{t,i} q_{t,j} \int_0^L m_b(x)\varphi_i\varphi_j dx + \frac{1}{2}\sum_{i=N+1}^{N+NA}\left[m_{p,i} q_{t,i}^2 + m_{s,i}\sum_{j=1}^{N}\sum_{l=1}^{N} q_{t,j} q_{t,l} \varphi_j(x_i)\varphi_l(x_i) \right], \tag{4.6}$$

where the position dependency notation from φ_i and φ_j inside the integral dropped because of simplicity. The elements of the mass matrix are identified as

$$m_{ij} = \begin{cases} \displaystyle\int_0^L m_b(x)\varphi_i\varphi_j dx + \sum_{l=N+1}^{N+NA} m_{s,l}\varphi_i(x_l)\varphi_j(x_l), & i, j \le N \\ \delta_{ij} m_{p,i}, & i, j > N \end{cases} \tag{4.7}$$

where δ_{ij} is the Kronecker delta where $\delta_{ij} = 1$ for $i = j$ and $\delta_{ij} = 0$ for $i \neq j$. Note that the added enclosure masses couple the coordinates through the mass matrix. The mass matrix is

symmetric, that is, $m_{ij} = m_{ji}$. There are 3 states for a single PID and the mass matrix is the same for the sticking states (i.e. when the particle is (i) stuck to the enclosure floor, or (ii) stuck to the enclosure ceiling). The last state is when the particle is (iii) in free flight. The DOF of the beam system decreases for this state and the motion of the particle in free flight is tracked with free fall equation given in Eq. (3.11). However, for computational simplicity the same mass matrix is used for all 3 states and the extra DOF results for (iii) are discarded. This is possible because the stiffness and damping matrices are decoupled for (iii) which will be explained shortly. If the beam is uniform, then $m_b(x)$ is constant and may be removed from the integrand.

When the particle is stuck either to the enclosure floor or ceiling, the stiffness matrix can be found using the following analysis. If the beam has stiffness per unit length $EI(x)$, where E is the Young's modulus and I is the cross-section area moment of inertia, then the potential energy for the beam and attached masses may be expressed as

$$V = \frac{1}{2}\int_0^L EI(x) w_{xx}^2 dx + \frac{1}{2}\sum_{i=N+1}^{N+NA} k_i \left(q_i - w(x_i)\right)^2 . \tag{4.8}$$

If the beam is uniform, then EI is constant and may be removed from the integrand. In Eq. (4.8), the k_i are the floor or ceiling spring constants depending on the PID state. Using the assumed modes expansion for w yields

$$V = \frac{1}{2}\sum_{i=1}^{N}\sum_{j=1}^{N} q_i q_j \int_0^L EI(x)\varphi_{xx,i}\varphi_{xx,j} dx + \frac{1}{2}\sum_{i=N+1}^{N+NA} k_i \left(q_i - \sum_{l=1}^{N} q_l \varphi_l(x_i) \right)^2 , \tag{4.9}$$

from which the elements of the stiffness matrix are identified as

$$k_{ij} = \begin{cases} \int_0^L EI(x)\varphi_{xx,i}\varphi_{xx,j} dx + \sum_{l=N+1}^{N+NA} k_l \varphi_i(x_l)\varphi_j(x_l), & i, j \le N \\ -k_j \varphi_i(x_j), \quad i \le N, j > N, & -k_i \varphi_j(x_i), \quad j \le N, i > N \\ \delta_{ij} k_i, & i, j > N \end{cases} . \tag{4.10}$$

Note that the added discrete springs couple the coordinates though the stiffness matrix. When the particle is in free flight, the floor and ceiling springs are not active so the stiffness matrix can be found as

$$k_{ij} = \begin{cases} \int_0^L EI(x)\varphi_{xx,i}\varphi_{xx,j}dx & i, j \le N \\ 0, \quad i \le N, j > N, \quad 0, \quad j \le N, i > N. \\ 1, \quad i, j > N \end{cases} \tag{4.11}$$

The diagonal entries for PID DOFs are selected to be non-zero to keep the overall DOF constant for all 3 states. The results for the PID DOFs are discarded when the particle is in free flight as in Chapter 3. Particle motion is tracked separately. The stiffness matrix is symmetric, that is, $k_{ij} = k_{ji}$. Since multiple PIDs may be used, the number of states for n PIDs is

$$\text{Number of States} = 3^n. \tag{4.12}$$

Up to this point, specific assumed mode basis functions are not considered in the development, nor have the number and location of the discrete added PID systems been fixed. Therefore, the above development may be considered generic, and suitable for adaptation to almost any beam/mass system.

4.2.2 Cantilever Beam Specifics

For a cantilever beam, the basis functions are assumed to be

$$\varphi_i(x) = \left(\frac{x}{L}\right)^{i+1}, \tag{4.13}$$

where L is the length of the beam. These basis functions satisfy the geometric boundary conditions at $x = 0$ where both displacement and slope equal to zero. With a uniform mass density, $m_b(x) = m_b = constant$, such that the elements of the mass matrix are

$$m_{ij} = \begin{cases} m_b \int_0^L \left(\frac{x}{L}\right)^{i+j+2} dx + \sum_{l=N+1}^{N+NA} m_{s,l} \left(\frac{x_l}{L}\right)^{i+j+2}, & i, j \le N \\ \delta_{ij} m_{p,i}, & i, j > N \end{cases}, \tag{4.14}$$

$$m_{ij} = \begin{cases} \frac{m_b L}{i+j+3} + \sum_{l=N+1}^{N+NA} m_{s,l} \left(\frac{x_l}{L}\right)^{i+j+2}, & i, j \le N \\ \delta_{ij} m_{p,i}, & i, j > N \end{cases}. \tag{4.15}$$

With a uniform stiffness, $EI(x) = EI = constant$, such that the elements of the stiffness matrix for the sticking and free flight conditions respectively are

$$k_{ij} = \begin{cases} \frac{EIij(i+1)(j+1)}{(i+j-1)L^3} + \sum_{l=N+1}^{N+NA} k_l \left(\frac{x_l}{L}\right)^{i+1} \left(\frac{x_l}{L}\right)^{j+1}, & i, j \le N \\ -k_j \left(\frac{x_j}{L}\right)^{i+1}, \quad i \le N, j > N, \quad -k_i \left(\frac{x_i}{L}\right)^{j+1}, \quad j \le N, i > N, \\ \delta_{ij} k_i, & i, j > N \end{cases} \tag{4.16}$$

$$k_{ij} = \begin{cases} \frac{EIij(i+1)(j+1)}{(i+j-1)L^3} & i, j \le N \\ 0, \quad i \le N, j > N, \quad 0, \quad j \le N, i > N. \\ 1, & i, j > N \end{cases} \tag{4.17}$$

A periodic impulsive force $F(t) = F\delta(t)$ is applied at a single point on the beam, such that the generalized forces (applied to the beam DOF only, not to the PID DOF) are

$$Q_i = F\varphi_i = F\left(\frac{x_F}{L}\right)^{i+1}, \tag{4.18}$$

where x_F is the distance from the clamped end of the beam.

4.2.3 Equivalent Viscous Damping Model

The damping model consists of two elements: i) damping of the PIDs, ii) damping of the beam. The derivation of equivalent viscous damping model in Chapter 3 is used for the former. For the latter, proportional damping is used. The damping matrix of the beam without the PIDs is defined by the classical Rayleigh damping equation as

$$C_{beam} = \mu M_{beam} + \lambda K_{beam}, \tag{4.19}$$

where C_{beam}, M_{beam} and K_{beam} are damping, mass and stiffness matrices, respectively, μ and λ are proportionality constants. They are assumed to be equal for this study ($\mu = \lambda$). The damping ratio is

$$\xi = \frac{1}{2}\left(\frac{\mu}{\omega} + \lambda\omega\right), \tag{4.20}$$

where ω is the response frequency in rad/s. Equivalent viscous damping is

$$c_{eq} = \frac{k\eta}{\omega_n} = \eta\sqrt{km}, \tag{4.21}$$

where η is the loss factor, k is the stiffness, m is the mass and ω_n is the natural frequency. Equivalent damping ratio is

$$\xi_{eq} = \frac{c_{eq}}{c_{cr}} = \frac{c_{eq}}{2\sqrt{km}} = \frac{\eta\sqrt{km}}{2\sqrt{km}} = \frac{\eta}{2}, \tag{4.22}$$

where c_{cr} is the critical damping. Using Eq. (4.20) and (4.22) the loss factor is found as

$$\eta = \frac{\mu}{\omega} + \lambda\omega, \tag{4.23}$$

For a lightly damped system, it is assumed that $\eta \leq 1\%$. Typically, intended excitation mechanisms (rivet guns) operate at 30 Hz. So, the excitation frequency and loss factor are,

$$\omega = 2\pi f = 60\pi, \tag{4.24}$$

$$\eta = \lambda\left(\frac{1}{\omega} + \omega\right) \leq 0.01\,. \tag{4.25}$$

Using the given values, λ is found as

$$\lambda \leq 5.3\times10^{-5}\,. \tag{4.26}$$

Therefore, λ is assumed to be,

$$\lambda = 5.0\times10^{-5}\,. \tag{4.27}$$

Lagrange's equations in their well-known form do not account for viscous damping forces explicitly. Viscous damping forces are accounted for implicitly through the generalized nonconservative forces. However, they can be expressed explicitly in the form

$$\left(Q_i\right)_{visc} = -\frac{\partial F_R}{\partial \dot{q}_i}, \quad i = 1, 2, \ldots, N \tag{4.28}$$

where F_R, Rayleigh's dissipation function, is a function of the generalized velocities [56]. Lagrange's equations can be rewritten as

$$\frac{d}{dt}\left(\frac{\partial T}{\partial \dot{q}_i}\right) - \frac{\partial T}{\partial q_i} + \frac{\partial V}{\partial q_i} + \frac{\partial F_R}{\partial \dot{q}_i} = Q_i\,, \tag{4.29}$$

assuming that the generalized forces Q_i include all nonconservative forces with the exception of the viscous forces. Rayleigh's dissipation function has the form

$$F_R = \frac{1}{2}\sum_{i=1}^{N}\sum_{j=1}^{N} c_{ij}\dot{q}_i\dot{q}_j\,, \tag{4.30}$$

where $c_{ij} = c_{ji}$ are constant, symmetric damping coefficients [56]. To find c_{ij}, the two elements of the damping model need to be merged as

$$F_R = \frac{1}{2}\sum_{i=1}^{N}\sum_{j=1}^{N}\left(C_{beam}\right)_{ij}\dot{q}_i\dot{q}_j + \frac{1}{2}\sum_{i=N+1}^{N+NA} c_i\left(\dot{q}_i - w_t(x_i)\right)^2\,. \tag{4.31}$$

In Eq. (4.31), the c_i are the floor or ceiling damper constants depending on the PID state. Using the assumed modes expansion for *w* yields

$$F_R = \frac{1}{2}\sum_{i=1}^{N}\sum_{j=1}^{N}\left(C_{beam}\right)_{ij}\dot{q}_i\dot{q}_j + \frac{1}{2}\sum_{i=N+1}^{N+NA} c_i\left(\dot{q}_i - \sum_{l=1}^{N}\dot{q}_l\varphi_l(x_i)\right)^2, \tag{4.32}$$

from which the elements of the damping matrix for the sticking conditions are identified as

$$c_{ij} = \begin{cases} \left(C_{beam}\right)_{ij} + \sum_{l=N+1}^{N+NA} c_l\left(\frac{x_l}{L}\right)^{i+1}\left(\frac{x_l}{L}\right)^{j+1}, & i, j \le N \\ -c_j\left(\frac{x_j}{L}\right)^{i+1}, & i \le N, j > N, \quad -c_i\left(\frac{x_i}{L}\right)^{j+1}, \quad j \le N, i > N \\ \delta_{ij}c_i, & i, j > N \end{cases}. \tag{4.33}$$

When the particle is in free flight, floor and ceiling dampers are not active so the damping matrix can be found as

$$c_{ij} = \begin{cases} \left(C_{beam}\right)_{ij}, & i, j \le N \\ 0, & i \le N, j > N, \quad 0, \quad j \le N, i > N \\ 0, & i, j > N \end{cases}. \tag{4.34}$$

4.3 Simulation Results of the Cantilever Beam with PIDs

The beam parameters and their values can be seen in Table 4. The dimensionless parameters used are mass ratio, $m' = (m_p + m_s)/m$, where m is the mass of the beam, frequency ratio, $\omega' = \omega/\omega_n$, where ω is the forcing frequency and ω_{n1} is the fundamental frequency of the beam, dimensionless gap clearance $h' = h{\omega_{n1}}^2/g$, and dimensionless forcing amplitude, $f' = F/(mg)$. For the simulations below, the dimensionless parameter values are $m' = 0.1$ where $m_p = m_s$, $\omega' = 1$, h'=2, and $f' = 11$ unless otherwise noted.

Table 4: Beam parameters

Parameter	Value
Width	30 mm
Thickness	5 mm
Length	1 m
Modulus of Elasticity	200 GPa
Density	7800 kg/m^3

4.3.1 Effect of Excitation Frequency

Figure 33 shows the simulated response amplitude (normalized by the forcing amplitude) vs. excitation frequency of the beam without a PID (clean beam) and the beam with a PID attached to the free end under *harmonic excitation*. The y-axis shows the ratio of the displacement amplitude at the free end of the beam to the forcing amplitude. In the given frequency range, the beam has natural frequencies at 26 rad/s and 162 rad/s. Because of the extra mass, attaching the PID to the beam decreases the natural frequencies to 22 rad/s and 149 rad/s, respectively.

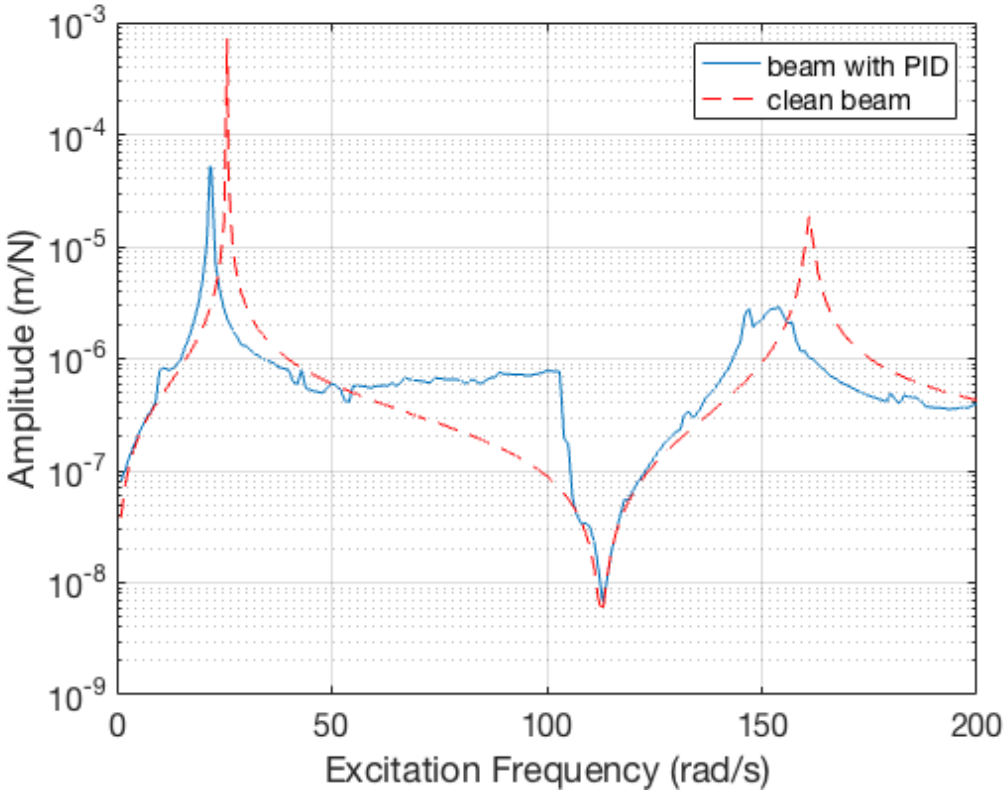

Figure 33: Response amplitude (normalized by the forcing amplitude) vs. excitation frequency of the beam without a PID and the beam with a PID attached to the free end under harmonic excitation.

Figure 34 shows the simulated response amplitude (normalized by the forcing amplitude) vs. excitation frequency of the beam without a PID (clean beam) and the beam with a PID attached to the free end under *periodic impulse excitation*. Note that compared to the harmonic excitation, there are a lot of extra peaks for both the clean beam and the beam with an attached PID in the same frequency range. This is because of the oscillatory behavior seen in Figure 3.16 and Figure 3.17. At ω_n/k where ω_n are the natural frequencies of the beam and $k = 1, 2, 3 \ldots$, response amplitudes are higher because of the high relative momentum change of the structure. For example, the first natural frequency of the clean beam is at 26 rad/s and there are peaks at one half and one third of this frequency. The same pattern is visible for the second natural

frequency as well. Note that as k increases in ω_n/k, amplitudes decrease and peaks become less prominent.

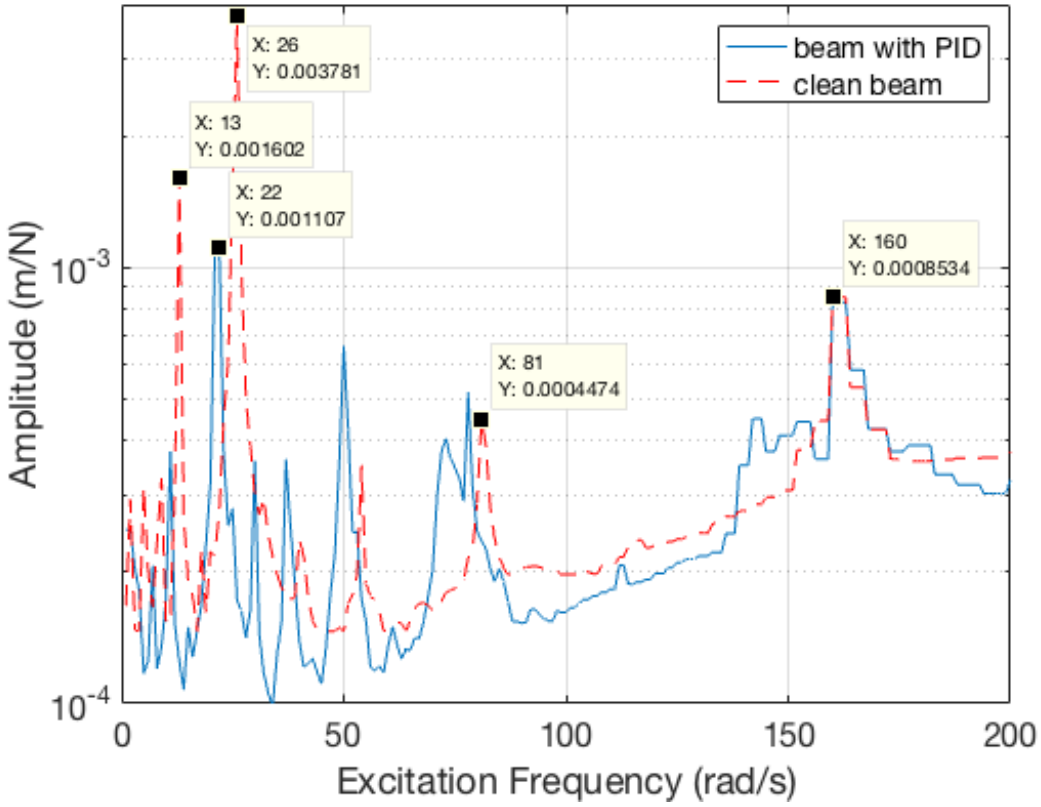

Figure 34: Response amplitude (normalized by the forcing amplitude) vs. excitation frequency of the beam without a PID and the beam with a PID attached to the free end under periodic impulse excitation.

Figure 35 is a combination of the data in Figure 33 and Figure 34. The y-axis shows the amplitude ratio of the clean beam to the beam with an attached PID for both periodic impulse and harmonic excitations. The comparison shows that, PIDs have more potential under impulse excitation to provide higher effectiveness within a broadband frequency range. As previously for a single PID, for the best damping performance of a PID on a beam, the forcing frequency should be slightly larger than the fundamental frequency of the clean beam ($\omega' > 1$). The performance is highly affected by the frequency variation below this point.

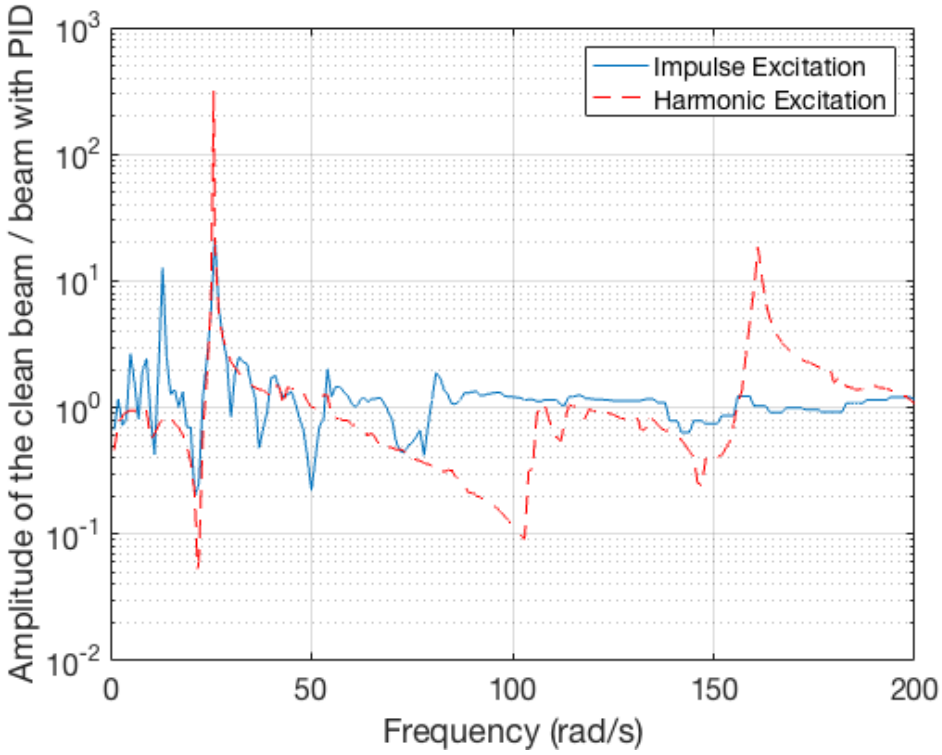

Figure 35: Amplitude of the clean beam / beam with PID comparison of harmonic vs. periodic impulse excitations.

4.3.2 Plotting Beam Mode Shapes to Explore Points with Maximum Displacement Amplitudes

Simulation results of the first 4 mode shapes of the beam can be seen in Figure 36. On the x-axis, 0 indicates the clamped end and 1 indicates the free end of the beam. Maximum displacements are normalized to 1. When the beam is excited at these 4 frequencies using periodic impulse excitation, the shapes of the beam are as in Figure 37. The difference is a result of the impulse force exciting all resonances within its useful frequency range. The useful frequency range of an impulse is a function of the impulse duration and its shape [57].

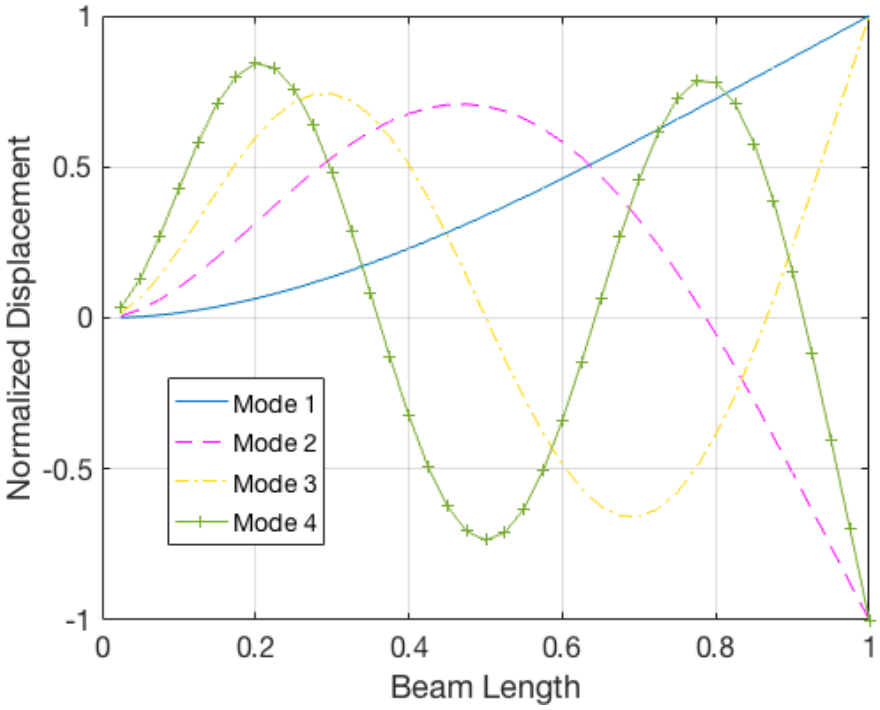

Figure 36: The first 4 mode shapes of the beam using harmonic excitation.

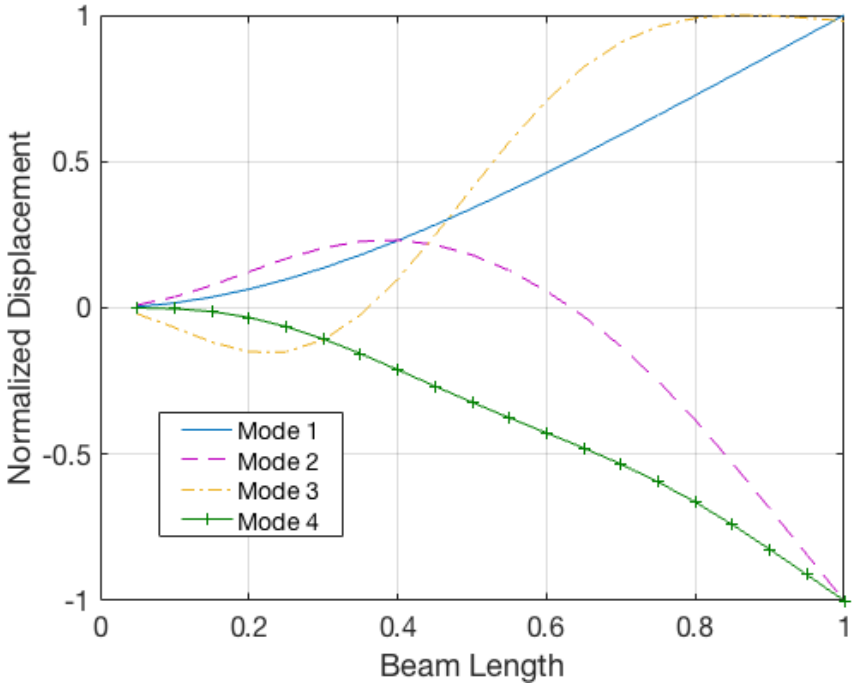

Figure 37: The operational deflection shapes of the beam using the first 4 natural frequencies under periodic impulse excitation.

Frequency analysis shows that the free end of the beam has always the maximum displacement and velocity amplitudes for the frequency range of interest. Therefore, the free end of the beam is selected as the performance point and it is aimed to decrease the maximum velocity amplitude on the beam.

4.3.3 Effect of the Gap Clearance for a Beam with a Single PID

Figure 38 shows the velocity ratio variation as a function of the dimensionless gap clearance for a single PID at the free end of the beam at $\omega' = 0.84$ for two different forcing amplitudes where $f'_{low} = 11$ and $f'_{high} = 154$. These values are chosen as examples for low and high forcing amplitudes. Figure 39 is a repetition for $f'_{low} = 11$, however with higher dimensionless gap clearance resolution between $h' = 0$ to $h' = 10$ to show the peak more clearly. Similar to the presented results for a single PID in Chapter 3, there is an optimum gap clearance for a single PID attached to a cantilever beam. Optimum gap clearance is greater for the higher forcing amplitude. This means, for an arbitrary excitation and PID arrays, non-uniform gap clearances may be more effective.

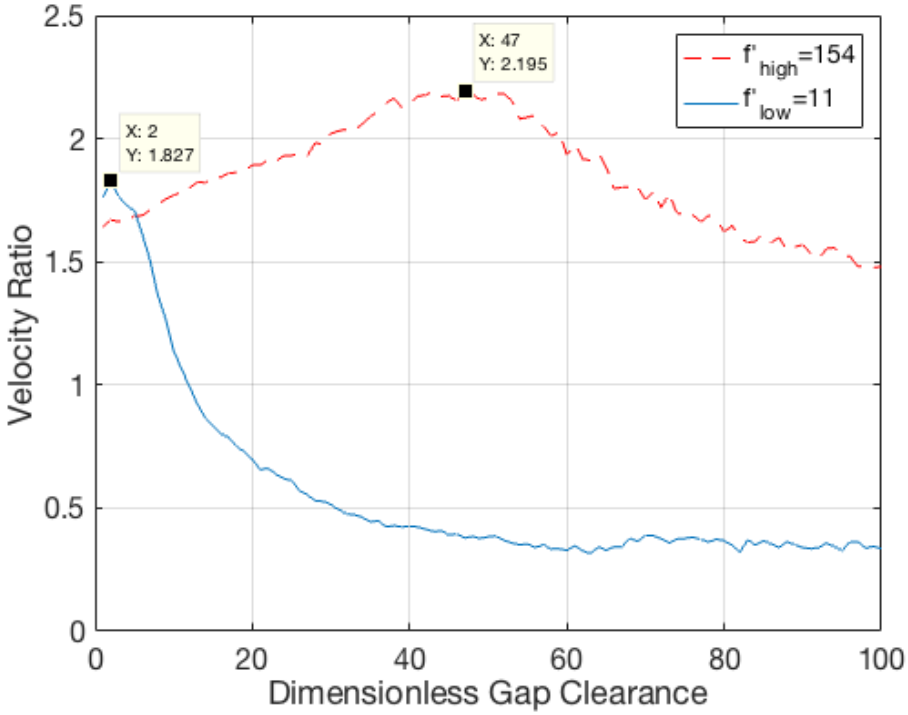

Figure 38: Velocity ratio variation as a function of the dimensionless gap clearance for two different forcing amplitudes where $f'_{low} = 11$ and $f'_{high} = 154$.

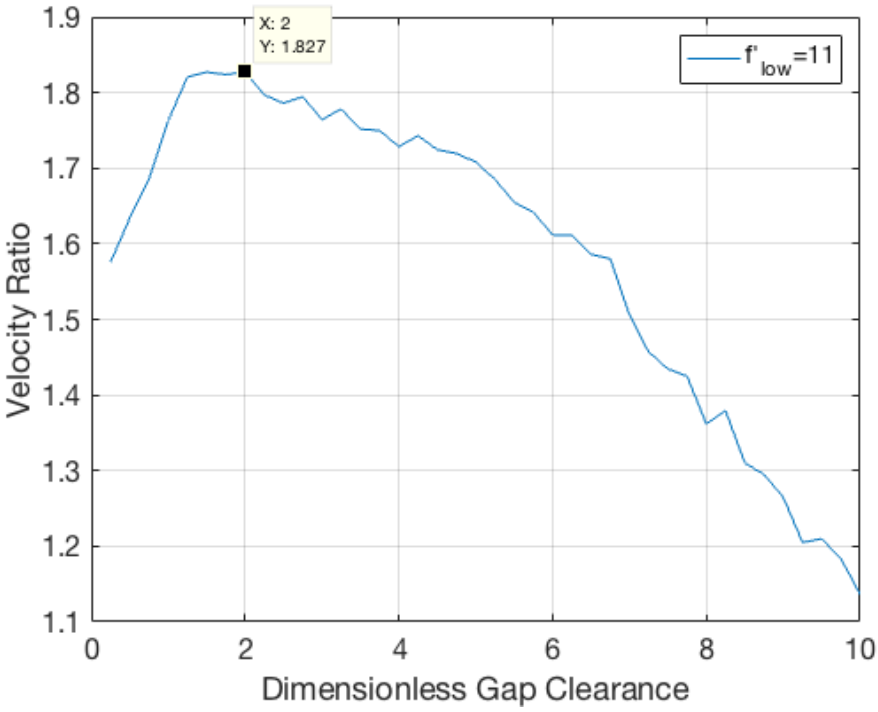

Figure 39: Velocity ratio variation as a function of the dimensionless gap clearance for $f'_{low} = 11$ (higher dimensionless gap clearance resolution between $h' = 0$ to $h' = 10$).

4.3.4 *Effect of PID Location and Excitation Point*

Figure 40 shows the velocity ratio variation as a function of a single PID location and excitation point along the length of the beam. On the *x* and *y* axes, 0 indicates the clamped end and 1 indicates the free end of the beam. For a fixed PID location, the velocity ratio increases as the excitation point is moved towards the free end. This is because the increasing moment arm of the input causes higher displacements. For a fixed forcing location, velocity ratio also increases as the PID is moved towards the free end where the amplitudes are higher. Similar trends have been reported by Butt and Akl [29]. They considered the placement of an impact damper along the length of a beam and showed that the damper is most effective when located away from the nodes of the dominant mode shape.

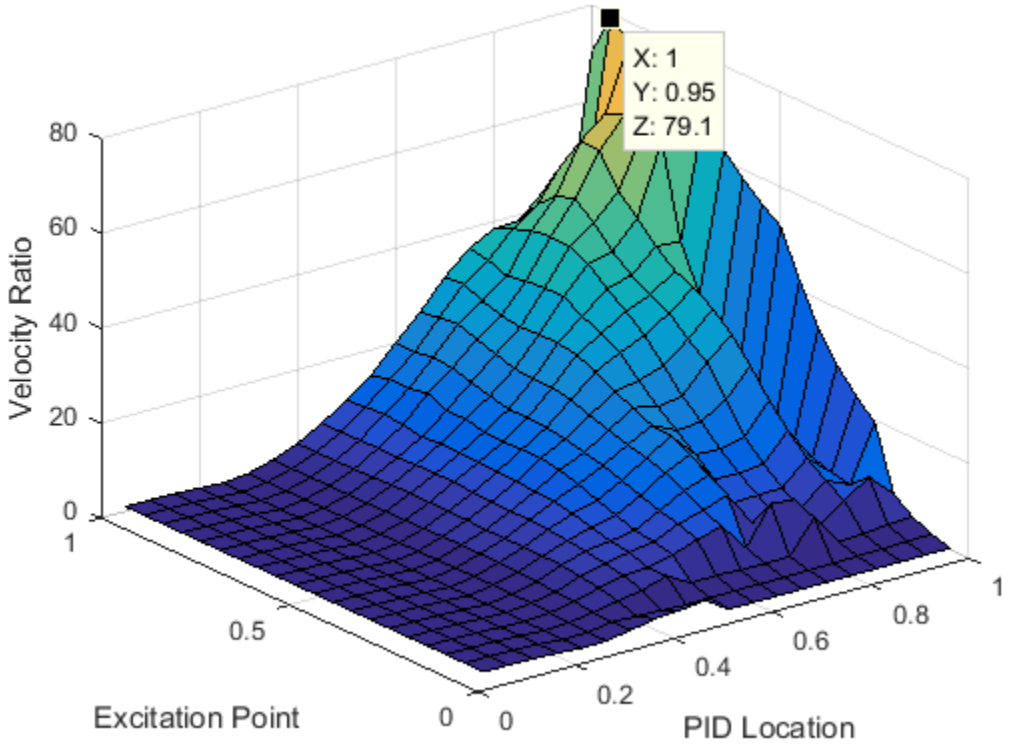

Figure 40: Velocity ratio variation as a function of PID location and excitation point along the length of the beam.

4.3.5 *Effect of Forcing Amplitude*

Figure 41 shows the schematic of the beam with forcing and an array of PID locations that are analyzed in this subsection. The force is applied at the tip of the beam. The PIDs are uniformly filled and the spacing is 4 cm. The mass ratio is constant ($m' = 0.1$) for all trials. For example, for 2 PIDs, the mass of a single PID (both m_s and m_p) is half of the 1 PID case. *S1*, *S3* and *S5* indicate the 1st, 3rd and 5th spots from the free end of the beam.

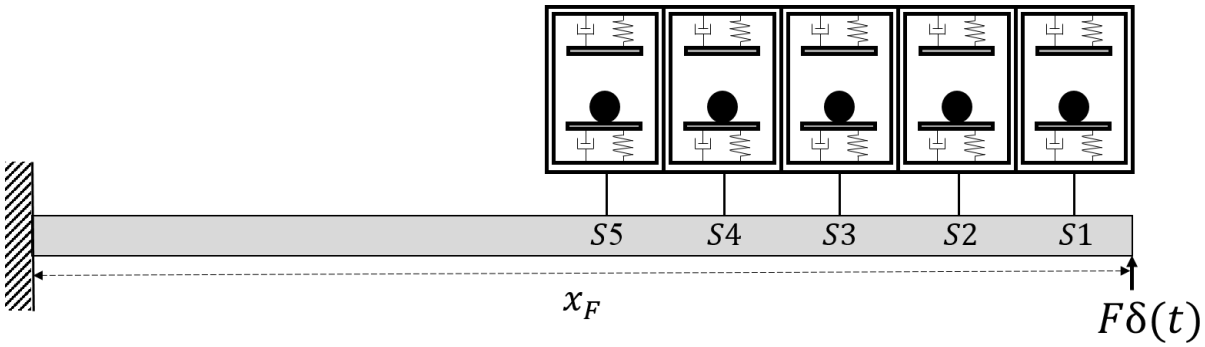

Figure 41: Modeled cantilever beam with particle impact dampers.

Figure 42 shows the velocity ratio variation as a function of the dimensionless forcing amplitude for 1 to 5 PIDs in Figure 41. A single PID at *S1* has the highest damping performance (velocity ratio). As the number of PIDs increases, the performance decreases. The reason is because amplitudes are highest at the free end of the beam and as the number of PIDs increases, the PID mass is distributed away from the tip of the beam. Also, note that the excitation point is at the tip of the beam and as the mass is distributed away from the tip, the mass impedance at the excitation point decreases. On the other hand, multiple PIDs have higher velocity ratio than a single PID at *S3* or *S5*. For a simple geometry like a cantilever beam, the points with the highest amplitudes are known but for a more complex geometry, a distributed array of PIDs may be more advantageous in terms of the damping performance.

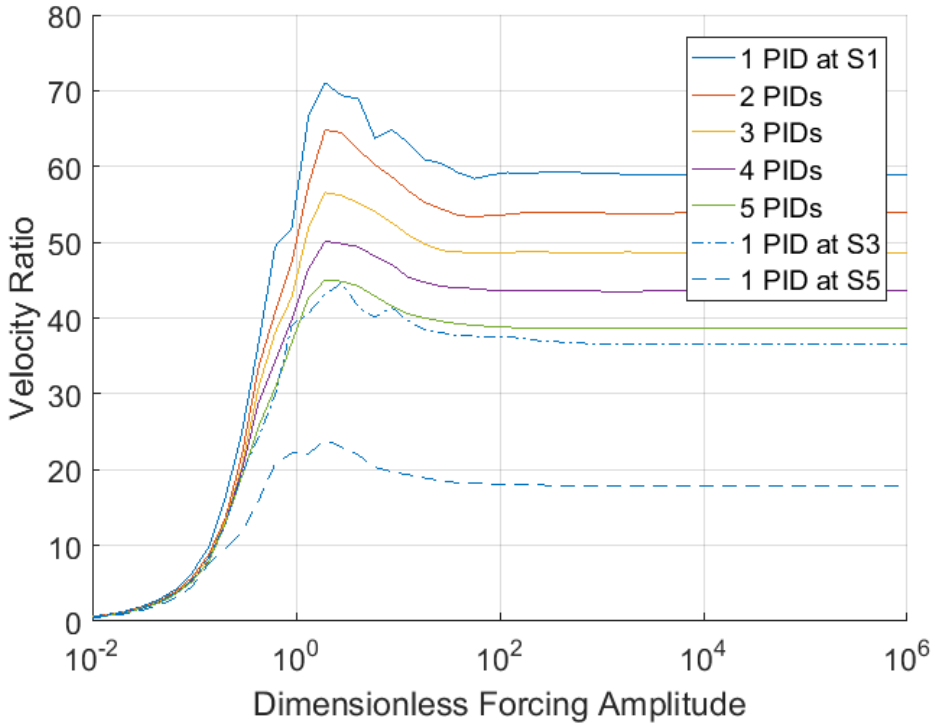

Figure 42: Velocity ratio variation as a function of the dimensionless forcing amplitude for 1-5 PIDs. Excitation is at the tip of the beam.

Velocity ratio behaviors of 1 PID vs. 5 PIDs are compared in Figure 43 as a function of the PID location along the length of the beam. The force is applied at the tip of the beam. For 5 PIDs, the rightmost (closer to the free end of the beam) PID location is selected as the reference. For both cases, as the PIDs are moved towards the free end, velocity ratios increase. Here, the idea is to compare the general trends of velocity ratio variation, not the values directly. This is done because if the number of PIDs is not equal, it is impossible to keep both the mass ratio and PID cell properties constant. In this analysis, the mass ratio is kept constant, so PID cells have less mass (m_s and m_p). Also, note that gap clearances are uniform for the 5 PID case and optimum gap clearances for each PID are not considered.

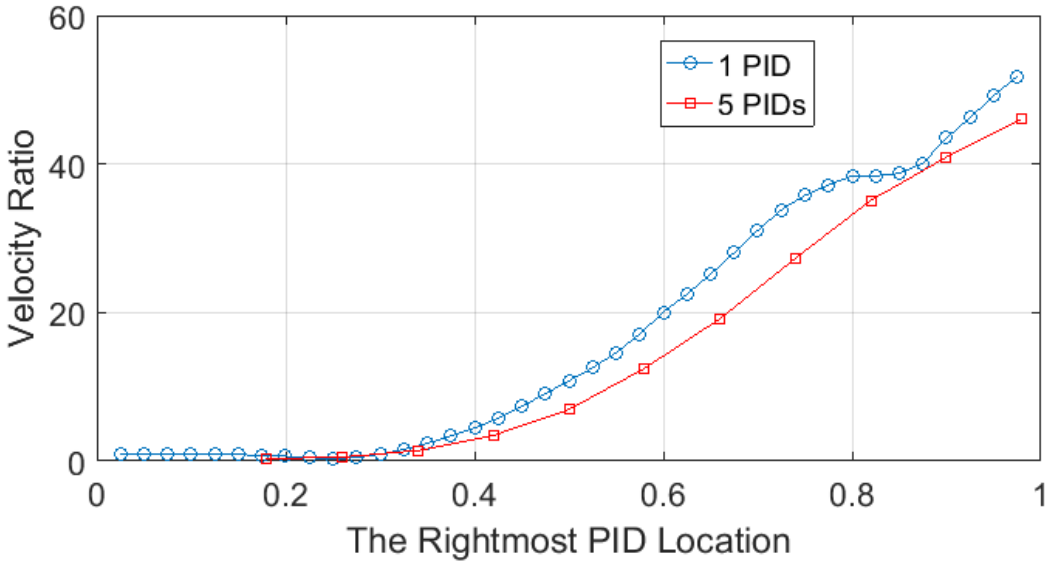

Figure 43: Velocity ratio comparison for 1 vs. 5 PIDs as a function of PID location. Excitation is at the tip of the beam.

CHAPTER 5

DISTRIBUTED ARRAY OF RESILIENT PARTICLE IMPACT DAMPERS ON A PLATE UNDER PERIODIC IMPULSE EXCITATION

5.1 Overview

This chapter develops analysis techniques for the distributed array of resilient PIDs attached to a plate under periodic impulse excitation. The chapter begins with the development of the equations of motion of a general plate/mass system. The method of assumed modes is used to model the transverse displacement field on the plate and Lagrange's equations are used to express the kinetic and potential energy of the plate and attached masses. Then, specific assumed mode basis functions are considered for a simply supported plate to identify the elements of the mass and the stiffness matrices. Rayleigh's dissipation function is used to construct the damping matrix. Finally, various simulation results are shown to characterize the PID effectiveness attached to a simply supported plate.

5.2 Methodology

5.2.1 Equations of Motion for a Plate with Attached PIDs

Figure 32 depicts the modeled particle impact damper attached to a vibrating plate. The equation of motion is identical in form to that of Eq. (4.1), that is,

$$M\ddot{q} + C\dot{q} + Kq = Q\ , \tag{5.1}$$

where M, C and K are the mass, damping and stiffness matrices, respectively, Q is a vector of forces, q is a vector of physical or generalized coordinates. For the PID system, there are as many possible equations of motion as there are available states,

$$\begin{matrix} M_1\ddot{q} + C_1\dot{q} + K_1 q = Q \\ \cdots \\ M_{sN}\ddot{q} + C_{sN}\dot{q} + K_{sN} q = Q \end{matrix} . \tag{5.2}$$

where subscript sN indicates the state number. Note that, only one of the above equations is active depending on the PID state.

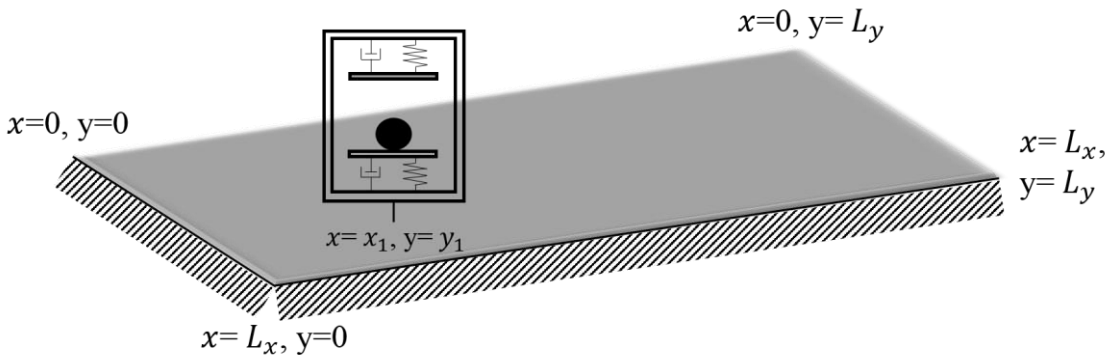

Figure 44: A schematic of the modeled particle impact damper attached to a vibrating plate. Altough arrays of PIDs are also considered, a single PID is shown for simplicity.

Using the method of assumed modes, the transverse displacement field on the beam is represented as

$$w(x, y, t) = \sum_{i=1}^{N} \varphi_i(x, y) q_i(t) = \varphi^T q \,, \tag{5.3}$$

where N is the number of assumed modes, φ are assumed mode basis functions, and q are generalized coordinates. The assumed mode basis functions are now functions of two coordinates, x and y. For simplicity, time and position dependency notation from φ and q will be omitted henceforth. In Eq. (5.3), superscript T stands for the transpose operation.

For notational consistency, q are used as generalized coordinates for all DOFs including those for PIDs attached to the plate. For example, if there are N modes in the expansion, plus two attached PIDs, then

$$q = \{q_1 \ \cdots \ q_N \ q_{N+1} \ q_{N+2}\}^T . \tag{5.4}$$

In Eq. (4.4), the first N q's are the coordinates associated with the plate motion, while the last two are the coordinates related to the PID displacements.

Indicial notation is used to indicate differentiation with respect to the index in the following. If the plate has mass per unit area $m_{pl}(x,y)$, and NA discrete PIDs attached, then using Lagrange's equation, the kinetic energy for the plate and attached masses may be expressed as

$$T = \frac{1}{2}\int_0^{L_x}\int_0^{L_y} m_{pl}(x,y)w_t^2 dydx + \frac{1}{2}\sum_{i=N+1}^{N+NA}\left[m_{p,i}q_{t,i}^2 + m_{s,i}w_t(x_i,y_i,t)^2\right]. \tag{5.5}$$

In Eq. (4.5), the (x_i, y_i) are the physical locations of the attachment points on the plate, and the $m_{p,i}$ and $m_{s,i}$ are the masses of the particles and enclosures of the PIDs, respectively. Using the assumed modes expansion for the transverse displacement field, w yields

$$\begin{aligned} T &= \frac{1}{2}\sum_{i=1}^{N}\sum_{j=1}^{N} q_{t,i}q_{t,j}\int_0^{L_x}\int_0^{L_y} m_{pl}\varphi_i\varphi_j dydx \\ &+ \frac{1}{2}\sum_{i=N+1}^{N+NA}\left[m_{p,i}q_{t,i}^2 + m_{s,i}\sum_{j=1}^{N}\sum_{l=1}^{N} q_{t,j}q_{t,l}\varphi_{j,i}\varphi_{l,i}\right] \end{aligned}. \tag{5.6}$$

From Eq. (5.6), the elements of the mass matrix, M, are

$$m_{ij} = \begin{cases} \int_0^{L_x}\int_0^{L_y} m_{pl}\varphi_i\varphi_j dydx + \sum_{l=N+1}^{N+NA} m_{s,l}\varphi_{i,l}\varphi_{j,l}, & i,j \le N \\ \delta_{ij}m_{p,i}, & i,j > N \end{cases} \tag{5.7}$$

where δ_{ij} is the Kronecker delta, $\delta_{ij} = 1$ for $i = j$ and $\delta_{ij} = 0$ for $i \neq j$. Note that the added enclosure masses couple the coordinates through the mass matrix. The mass matrix is symmetric, that is, $m_{ij} = m_{ji}$. There are 3 states for a single PID and the mass matrix is the same for the sticking states (i.e. when the particle is (i) stuck to the enclosure floor, or (ii) stuck to the enclosure ceiling). The last state is when the particle is (iii) in free flight. The DOF of the plate

system decreases for this state and the motion of the particle in free flight is tracked with free fall equation given in Eq. (3.11). However, for computational simplicity the same mass matrix is used for all 3 states and the extra DOF results for (iii) are discarded. This is possible because the stiffness and damping matrices are decoupled for (iii) which will be explained shortly. If the plate is uniform, then $m_{pl}(x,y)$ is constant and may be removed from the integrand.

When the particle is stuck either to the enclosure floor or ceiling, the stiffness matrix can be found using the following analysis. The potential energy for the plate and attached masses may be expressed as [58]

$$\begin{aligned} V &= \frac{1}{2}\int_0^{L_x}\int_0^{L_y} D(x,y)\left\{w_{xx}^2 + w_{yy}^2 + 2\nu w_{xx}w_{yy} + 2(1-\upsilon)w_{xy}^2\right\}dydx \\ &+ \frac{1}{2}\sum_{i=N+1}^{N+NA} k_i\left(q_i - w(x_i,y_i)\right)^2 \end{aligned}, \tag{5.8}$$

where

$$D(x,y) = \frac{E(x,y)h(x,y)^3}{12(1-\upsilon^2)}, \tag{5.9}$$

is the bending rigidity, E is the Young's modulus, ν is Poisson's ratio, and h is the plate thickness. If the plate is uniform, then D is constant and may be removed from the integrand. In Eq. (5.8), the k_i are the floor or ceiling spring constants depending on the PID state. Using the assumed modes expansion for w yields

$$\begin{aligned} V &= \frac{1}{2}\int_0^{L_x}\int_0^{L_y} D\left\{\sum_{j=1}^{N}\sum_{i=1}^{N} q_i q_j \varphi_{xx,i}\varphi_{xx,j} + \sum_{j=1}^{N}\sum_{i=1}^{N} q_i q_j \varphi_{yy,i}\varphi_{yy,j}\right\}dydx \\ &+ \frac{1}{2}\int_0^{L_x}\int_0^{L_y} D\,2\upsilon\left\{\left(\sum_{j=1}^{N}\sum_{i=1}^{N} q_i q_j \varphi_{xx,i}\varphi_{yy,j}\right) + (1-\upsilon)\sum_{j=1}^{N}\sum_{i=1}^{N} q_i q_j \varphi_{xy,i}\varphi_{xy,j}\right\}dydx \\ &+ \frac{1}{2}\sum_{i=N+1}^{N+NA} k_i\left(q_i - \sum_{l=1}^{N} q_l\varphi_l(x_i,y_i)\right)^2 \end{aligned}. \tag{5.10}$$

Interchanging the order of integration and summation, and dividing Eq. (5.10) into components yields

$$V = \sum_{i=1}^{5} C_i \,, \tag{5.11}$$

where

$$C_1 = \frac{1}{2}\sum_{i=1}^{N}\sum_{j=1}^{N} q_i q_j \int_0^{L_x}\int_0^{L_y} D\varphi_{xx,i}\varphi_{xx,j}\,dydx \,, \tag{5.12}$$

$$C_2 = \frac{1}{2}\sum_{i=1}^{N}\sum_{j=1}^{N} q_i q_j \int_0^{L_x}\int_0^{L_y} D\varphi_{yy,i}\varphi_{yy,j}\,dydx \,, \tag{5.13}$$

$$C_3 = \sum_{i=1}^{N}\sum_{j=1}^{N} q_i q_j \int_0^{L_x}\int_0^{L_y} D\upsilon\varphi_{xx,i}\varphi_{yy,j}\,dydx \,, \tag{5.14}$$

$$C_4 = \sum_{i=1}^{N}\sum_{j=1}^{N} q_i q_j \int_0^{L_x}\int_0^{L_y} D(1-\upsilon)\varphi_{xy,i}\varphi_{xy,j}\,dydx \,, \tag{5.15}$$

$$C_5 = \frac{1}{2}\sum_{i=N+1}^{N+NA} k_i \left(q_i - \sum_{l=1}^{N} q_l \varphi_l(x_i, y_i) \right)^2 . \tag{5.16}$$

Note that Eq. (5.10) is functionally the same as that for the beam. To make this evident, a linear differential operator L that generates the plate-dependent components of the integrals is introduced,

$$V = \frac{1}{2}\sum_{i=1}^{N}\sum_{j=1}^{N} q_i q_j \int_0^{L_x}\int_0^{L_y} L(\varphi_i, \varphi_j)\,dydx + \frac{1}{2}\sum_{i=N+1}^{N+NA} k_i \left(q_i - \sum_{l=1}^{N} q_l \varphi_l(x_i, y_i) \right)^2 . \tag{5.17}$$

The analogous expression for the beam is

$$V = \frac{1}{2}\sum_{i=1}^{N}\sum_{j=1}^{N} q_i q_j \int_0^{L} L(\varphi_i, \varphi_j)\,dx + \frac{1}{2}\sum_{i=N+1}^{N+NA} k_i \left(q_i - \sum_{l=1}^{N} q_l \varphi_l(x_i) \right)^2 , \tag{5.18}$$

which has the same functional form as Eq. (5.17). Therefore, the elements of the stiffness matrix, K, for the plate may be identified following the same procedure as for the beam, that is,

$$k_{ij} = \begin{cases} \int_0^{L_x}\int_0^{L_y} L(\varphi_i, \varphi_j)dydx + \sum_{l=N+1}^{N+NA} k_l \varphi_i(x_l, y_l)\varphi_j(x_l, y_l), & i, j \le N \\ -k_j \varphi_i(x_j, y_j), \quad i \le N, j > N, & -k_i \varphi_j(x_i, y_i), \quad j \le N, i > N \\ \delta_{ij} k_i, & i, j > N \end{cases} . \tag{5.19}$$

Note that the added discrete springs couple the coordinates though the stiffness matrix. When the particle is in free flight, the floor and ceiling springs are not active so the stiffness matrix can be found as

$$k_{ij} = \begin{cases} \int_0^{L_x}\int_0^{L_y} L(\varphi_i, \varphi_j)dydx & i, j \le N \\ 0, \quad i \le N, j > N, & 0, \quad j \le N, i > N \\ 1, & i, j > N \end{cases} . \tag{5.20}$$

The diagonal entries for PID DOFs are selected to be non-zero to keep the overall DOF constant for all 3 states. When the particle is in free flight, the results for the PID DOFs are discarded as in Chapter 3 and 4, because particle motion is tracked separately. The stiffness matrix is symmetric, that is, $k_{ij} = k_{ji}$. Since multiple PIDs may be used, the number of states for n PIDs is

$$\text{Number of States} = 3^n . \tag{5.21}$$

Up to this point, specific assumed mode basis functions are not considered in the development, nor have the number and location of the discrete added PID systems been fixed. Therefore, the above development may be considered generic, and suitable for adaptation to almost any plate/mass system.

5.2.2 Simply Supported Plate Specifics

For a uniform simply supported plate, the basis functions are assumed to be

$$\varphi(x,y) = 2\sin\left(\frac{m\pi x}{L_x}\right)\sin\left(\frac{n\pi y}{L_y}\right), \tag{5.22}$$

where m and n are integer indices. The leading factor 2 ensures that the basis functions for the plate are orthonormal. The basis functions in Eq. (5.22) are the analytical modes of simply supported plates without attachments and they are used as the assumed modes for the plate. The basis functions are formed by the multiplication of independent functions in the x and y directions. Therefore, each assumed mode has two associated indices, instead of the single index as used in Section 5.2.1.

The number of degrees of freedom is set by the upper limits selected for m and n, through the number of possible pairings of m and n,

$$DOF_{plate} = m \times n\,. \tag{5.23}$$

The total degrees of freedom in the model will be the sum of Eq. (5.23) and the number of discrete attachments in the system

$$DOF_{total} = DOF_{plate} + NA\,. \tag{5.24}$$

Each assumed mode having two associated indices, rather than a single index, introduces complexity and this complexity may be handled by structuring the coordinate vector for the plate DOF's as

$$\varphi = \{\varphi_{11} \cdots \varphi_{1M} \;\; \varphi_{21} \cdots \varphi_{2M} \cdots \varphi_{NM}\}^T\,. \tag{5.25}$$

where the subscripts on the basis functions indicate the indices m and n. By these means, each index into the coordinate vector maps to a unique combination of m and n, and the development in Section 5.2.1 may be applied.

For the mass matrix,

$$m_{ij} = \begin{cases} \int_0^{L_x}\int_0^{L_y} m_{pl}\varphi_i\varphi_j dydx + \sum_{l=DOF_{plate}+1}^{DOF_{plate}+NA} m_{s,l}\varphi_{i,l}\varphi_{j,l}, & i, j \le DOF_{plate} \\ \delta_{ij} m_{p,i}, & i, j > DOF_{plate} \end{cases}, \tag{5.26}$$

assuming a uniform plate thickness h, and for the plate degrees of freedom,

$$m_{ij} = \rho h \int_0^{L_x}\int_0^{L_y} 2\sin\left(\frac{m\pi x}{L_x}\right)\sin\left(\frac{n\pi y}{L_y}\right) 2\sin\left(\frac{p\pi x}{L_x}\right)\sin\left(\frac{q\pi y}{L_y}\right) dydx, \tag{5.27}$$

where m and n map to the subscript i, and p and q map to the subscript j. Eq. (5.27) can be rewritten as

$$m_{ij} = \rho h \int_0^{L_x} 2\sin\left(\frac{m\pi x}{L_x}\right)\sin\left(\frac{p\pi x}{L_x}\right) dx \int_0^{L_y} 2\sin\left(\frac{n\pi y}{L_y}\right)\sin\left(\frac{q\pi y}{L_y}\right) dy, \tag{5.28}$$

since the components of the mode functions are functions of a single variable. The orthogonality of the *sine* function over the plate then leads to

$$m_{ij} = \begin{cases} \rho h L_x L_{y,} & m = p \quad and \quad n = q \\ 0, & m \neq p \quad or \quad n \neq q \end{cases}. \tag{5.29}$$

The condition that $m = p$ and $n = q$ in Eq. (5.29) requires that $i = j$. Therefore, the entire mass matrix may be found as

$$m_{ij} = \begin{cases} \delta_{ij}\rho h L_x L_y + \sum_{l=DOF_{plate}+1}^{DOF_{plate}+NA} m_{s,l}\varphi_i(x_l, y_l)\varphi_j(x_l, y_l), & i, j \le DOF_{plate} \\ \delta_{ij} m_{p,i}, & i, j > DOF_{plate} \end{cases}. \tag{5.30}$$

For the stiffness matrix,

$$k_{ij} = \begin{cases} L(\varphi_i, \varphi_j) + \sum_{l=DOF_{plate}+1}^{DOF_{plate}+NA} k_l \varphi_i(x_l, y_l)\varphi_j(x_l, y_l), & i, j \le DOF_{plate} \\ -k_j \varphi_i(x_j, y_j), & i \le DOF_{plate},\ j > DOF_{plate} \\ -k_i \varphi_j(x_i, y_i), & j \le DOF_{plate},\ i > DOF_{plate} \\ \delta_{ij} k_i, & i, j > DOF_{plate} \end{cases}, \tag{5.31}$$

where

$$L(\varphi_i, \varphi_j) = \sum_{k=1}^{4} G_k \ , \tag{5.32}$$

and where

$$G_1 = \int_0^{L_x} \int_0^{L_y} D\varphi_{xx,i}\varphi_{xx,j} dydx \ , \tag{5.33}$$

$$G_2 = \int_0^{L_x} \int_0^{L_y} D\varphi_{yy,i}\varphi_{yy,j} dydx \ , \tag{5.34}$$

$$G_3 = 2\int_0^{L_x} \int_0^{L_y} D\upsilon\varphi_{xx,i}\varphi_{yy,j} dydx \ , \tag{5.35}$$

$$G_4 = 2\int_0^{L_x} \int_0^{L_y} D(1-\upsilon)\varphi_{xy,i}\varphi_{xy,j} dydx \ . \tag{5.36}$$

The derivatives required for computation of the stiffness matrix are:

$$\varphi_{xx}(x, y) = -2\left(\frac{m\pi}{L_x}\right)^2 \sin\left(\frac{m\pi x}{L_x}\right)\sin\left(\frac{n\pi y}{L_y}\right), \tag{5.37}$$

$$\varphi_{yy}(x, y) = -2\left(\frac{n\pi}{L_y}\right)^2 \sin\left(\frac{m\pi x}{L_x}\right)\sin\left(\frac{n\pi y}{L_y}\right), \tag{5.38}$$

$$\varphi_{xy}(x, y) = \varphi_{yx}(x, y) = 2\left(\frac{m\pi}{L_x}\right)\left(\frac{n\pi}{L_y}\right)\cos\left(\frac{m\pi x}{L_x}\right)\cos\left(\frac{n\pi y}{L_y}\right). \tag{5.39}$$

Assuming a uniform plate, and using orthogonality, yields

$$G_1 = D\left(\frac{m\pi}{L_x}\right)^4 L_x L_y\,, \tag{5.40}$$

$$G_2 = D\left(\frac{n\pi}{L_y}\right)^4 L_x L_y\,, \tag{5.41}$$

$$G_3 = 2D\upsilon\left(\frac{m\pi}{L_x}\right)^2\left(\frac{n\pi}{L_y}\right)^2 L_x L_y\,, \tag{5.42}$$

$$G_4 = 2D(1-\upsilon)\left(\frac{m\pi}{L_x}\right)^2\left(\frac{n\pi}{L_y}\right)^2 L_x L_y\,. \tag{5.43}$$

Like the mass matrix, the orthogonality of the *sine* functions requires that $i = j$. Therefore, the entire stiffness matrix for the sticking and free flight conditions respectively may be found as

$$k_{ij} = \begin{cases} \delta_{ij}L(\varphi_i,\varphi_j) + \sum_{l=DOF_{plate}+1}^{DOF_{plate}+NA} k_l\varphi_i(x_l,y_l)\varphi_j(x_l,y_l), & i,j \le DOF_{plate} \\ -k_j\varphi_i(x_j,y_j), & i \le DOF_{plate},\ j > DOF_{plate} \\ -k_i\varphi_j(x_i,y_i), & j \le DOF_{plate},\ i > DOF_{plate} \\ \delta_{ij}k_i, & i,j > DOF_{plate} \end{cases}, \tag{5.44}$$

$$k_{ij} = \begin{cases} \delta_{ij}L(\varphi_i,\varphi_j), & i,j \le DOF_{plate} \\ 0, & i \le DOF_{plate},\ j > DOF_{plate} \\ 0, & j \le DOF_{plate},\ i > DOF_{plate} \\ 1, & i,j > DOF_{plate} \end{cases}. \tag{5.45}$$

A periodic impulsive force $F(t) = F\delta(t)$ is applied at a single point on the plate, such that the generalized forces (applied to the plate DOF only, not to the PID DOF) are

$$Q_i = F\varphi_i = 2F\sin\left(\frac{m\pi x_F}{L_x}\right)\sin\left(\frac{n\pi y_F}{L_y}\right), \tag{5.46}$$

where (x_F, y_F) is the physical location of the excitation point on the plate.

5.2.3 Damping Model

Similarly to the beam, the damping model for the plate consists of two elements: i) damping of the PIDs, ii) damping of the plate. The derivation of equivalent viscous damping model in Chapter 3 is used for the former; the latter is modelled with proportional damping. The damping matrix of the plate without the PIDs is defined as

$$C_{plate} = \lambda (M_{plate} + K_{plate}) \tag{5.47}$$

where M_{plate} and K_{plate} are the mass and stiffness matrices of the plate without the PIDs, respectively. For a lightly damped system, the process of finding the proportionality constant, λ, is explained in Chapter 4.2.3. Using Eq. (4.26), it is assumed to be,

$$\lambda = 5.0 \times 10^{-5}. \tag{5.48}$$

Viscous damping forces can be accounted for in Lagrange's equations as,

$$\frac{d}{dt}\left(\frac{\partial T}{\partial \dot{q}_i}\right) - \frac{\partial T}{\partial q_i} + \frac{\partial V}{\partial q_i} = Q_i + (Q_i)_{visc}, \tag{5.49}$$

where $(Q_i)_{visc}$ is the viscous damping forces, and Q_i is the generalized forces including all non-conservative forces except for the viscous forces. Viscous damping forces can be expressed explicitly in the form

$$(Q_i)_{visc} = -\frac{\partial F_R}{\partial \dot{q}_i}, \quad i = 1, 2, ..., DOF_{plate}, \tag{5.50}$$

where F_R, Rayleigh's dissipation function, is a function of the generalized velocities [56]. Thus, Eq. (5.49) can be rewritten as

$$\frac{d}{dt}\left(\frac{\partial T}{\partial \dot{q}_i}\right) - \frac{\partial T}{\partial q_i} + \frac{\partial V}{\partial q_i} + \frac{\partial F_R}{\partial \dot{q}_i} = Q_i. \tag{5.51}$$

Rayleigh's dissipation function has the form

$$F_R = \frac{1}{2}\sum_{i=1}^{N}\sum_{j=1}^{N} c_{ij}\dot{q}_i\dot{q}_j \ , \tag{5.52}$$

where $c_{ij} = c_{ji}$ are constant, symmetric damping coefficients [56]. To find c_{ij}, the two elements of the damping model need to be merged as

$$F_R = \frac{1}{2}\sum_{i=1}^{DOF_{plate}}\sum_{j=1}^{DOF_{plate}} \left(C_{plate}\right)_{ij}\dot{q}_i\dot{q}_j + \frac{1}{2}\sum_{i=DOF_{plate}+1}^{DOF_{plate}+NA} c_i(\dot{q}_i - w_t(x_i, y_i))^2 \ . \tag{5.53}$$

In Eq. (5.53), the c_i are the floor or ceiling damper constants depending on the PID state. Using the assumed modes expansion for *w* yields

$$F_R = \frac{1}{2}\sum_{i=1}^{DOF_{plate}}\sum_{j=1}^{DOF_{plate}} \left(C_{plate}\right)_{ij}\dot{q}_i\dot{q}_j + \frac{1}{2}\sum_{i=DOF_{plate}+1}^{DOF_{plate}+NA} c_i\left(\dot{q}_i - \sum_{l=1}^{DOF_{plate}}\dot{q}_l\varphi_l(x_i, y_i)\right)^2 , \tag{5.54}$$

from which the elements of the damping matrix for the sticking conditions are identified as

$$c_{ij} = \begin{cases} \left(C_{plate}\right)_{ij} + \sum_{l=DOF_{plate}+1}^{DOF_{plate}+NA} c_l\varphi_i(x_l, y_l)\varphi_j(x_l, y_l), & i, j \le DOF_{plate} \\ -c_j\varphi_i(x_j, y_j), & i \le DOF_{plate},\ j > DOF_{plate} \\ -c_i\varphi_j(x_i, y_i), & j \le DOF_{plate},\ i > DOF_{plate} \\ \delta_{ij}c_i, & i, j > DOF_{plate} \end{cases} . \tag{5.55}$$

When the particle is in free flight, floor and ceiling dampers are not active so the damping matrix can be found as

$$c_{ij} = \begin{cases} \left(C_{plate}\right)_{ij}, & i, j \le DOF_{plate} \\ 0, & i \le DOF_{plate},\ j > DOF_{plate} \\ 0, & j \le DOF_{plate},\ i > DOF_{plate} \\ 0, & i, j > DOF_{plate} \end{cases} . \tag{5.56}$$

5.2.4 Metric of Performance

A plate, as schematically depicted in Figure 45, is a continuous structure and when considering the PID performance, it is aimed to decrease either the maximum or the average velocity amplitude on the plate depending on the simulation type. To be able to do this, an "effectiveness grid" is used to track the velocities of selected points on the plate. Figure 45 shows a schematic of the top view of the modeled simply supported plate with the effectiveness grid. The grid divides the plate into 16 equal parts and the 9 intersection points of the gridlines, indicated with the circles, are the selected points for effectiveness analysis. Frequency variation showed that the point with the maximum velocity varies for different excitation frequencies.

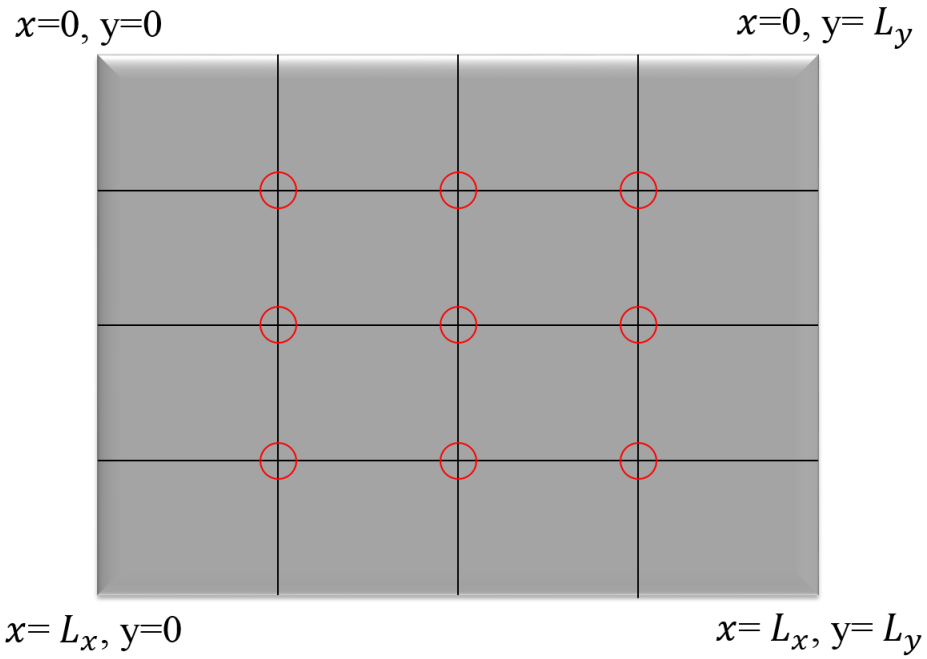

Figure 45: A schematic of the top view of the modeled simply supported plate with the effectiveness grid.

Finer grids were also tested and it was observed that the simulation duration significantly increases as the grid gets finer because effectiveness points are evaluated at each time step. Additionally, frequency variation results showed that the point with the maximum velocity is one of these 9 points for the plate considered and the frequency range of interest. Therefore, the velocities of the 9 points were tracked.

The velocity ratio is defined in Chapter 3 as

$$\psi = \frac{(v_{rms})_{noPID}}{(v_{rms})_{PID}}, \tag{5.57}$$

where $(v_{rms})_{noPID}$ is the RMS velocity of the base mass without an impact damper, and $(v_{rms})_{PID}$ is the RMS velocity of the base mass with an impact damper. $\psi > 1$, $\psi < 1$ and $\psi = 1$ correspond to increased effectiveness, decreased effectiveness and no impact, respectively.

5.2.5 Identification of Damping and Mass Effects using Kinetic Energy

The role of mass loading on the PID effectiveness is generally neglected in PID studies. However, relative locations of PIDs and excitation force, mass ratio, and damping ratio on continuous systems alter the mass loading vs. damping effects on energy input into the system and dissipation in the system, respectively. To identify and differentiate the damping and mass loading effects, two new measures are defined using the kinetic energy of the continuous system, the simply supported plate in this case, at various instants. The damping measure is defined as

$$Damping\ Measure = \frac{\left\langle T(t_{n^+})\right\rangle - \left\langle T(t_{(n+1)^-})\right\rangle}{\left\langle T(t_{n^+})\right\rangle}. \tag{5.58}$$

where $\left\langle T(t_{n^+})\right\rangle$ and $\left\langle T(t_{(n+1)^-})\right\rangle$ are the spatial average kinetic energy of the plate just after the n^{th} and just before the $(n+1)^{th}$ impulse excitations, respectively. By this means, the energy dissipation over a cycle can be quantified. The mass measure is defined as

$$Mass\ Measure = \frac{\left\langle T(t_{n^+})\right\rangle - \left\langle T(t_{n^-})\right\rangle}{\left\langle T(t_{n^-})\right\rangle_{noPID}}. \tag{5.59}$$

where $\left\langle T(t_{n^-})\right\rangle$ is the spatial average kinetic energy of the plate just before the nth impulse excitation and the subscript *noPID* indicates the plate without PIDs. By this means, the effect of the mass over a cycle can be quantified.

5.2.6 Dimensionless Parameters for the Plate Analysis

Table 5 shows the dimensionless parameters used in this chapter. In Table 5, m_p is the mass of the particle, m_s is the mass of the PID enclosure, m is the mass of the plate, h is the gap clearance, F is the forcing amplitude, ω is the forcing frequency, and ω_{n1} is the fundamental frequency of the plate. For the simulations Section 5.3, the dimensionless parameter values in Table 5 were used unless otherwise noted.

Table 5: Dimensionless parameters used for the plate analysis.

Parameter	**Equation**	**Value**
Mass ratio, m'	$m' = (m_p + m_s)/m$	$m' = 0.1,\ m_p = m_s$
Dimensionless gap clearance, h'	$h' = h{\omega_{n1}}^2/g$	$h' = 72.4$
Dimensionless forcing amplitude, f'	$f' = F\omega/(mg)$	$f' = 8.9$
Frequency ratio, ω'	$\omega' = \omega/\omega_{n1}$	$\omega' = 1$

5.3 Simulation Results of the Simply Supported Plate with PIDs

In this section, the effects of the excitation (forcing) frequency, forcing location, forcing amplitude, PID location, ratio of the particle mass to the enclosure mass, and plate dimension on the PID effectiveness are analyzed. The plate parameters and their values can be seen in Table 6.

Table 6: Simply supported plate parameters and their values.

Parameter	Value
Width	1 m
Thickness	7.91 mm
Length	4/3 m
Modulus of Elasticity	68.9 GPa
Poisson's Ratio	0.33
Density	2700 kg/m^3

5.3.1 Effect of Excitation Frequency

Figure 46 shows the velocity amplitude (normalized by the forcing amplitude) vs. excitation frequency plots of the plate without a PID (clean plate), the plate with an untuned PID attached at the center of the plate, and a tuned PID attached at the center under *harmonic excitation*. Here, "tuned" means a stiffness value for the PID floor is chosen so that the PID frequency is adjusted to the first natural frequency of the undamped system. This would affect the response amplitudes which is explained in the following analysis. The y-axis shows the ratio of the velocity amplitude at the center of the plate to the forcing amplitude. The plate is excited at $[0.250L_x, 0.375L_y]$. The first natural frequency of the clean plate is at 188 rad/s. When the untuned PID is attached, this frequency decreases to 184 rad/s with the effect of the extra mass. There is also a smaller peak at 92 rad/s due to the additional DOF of the PID. When the natural frequency of the PID is tuned to the first natural frequency of the plate, the amplitude of the

resonance frequency decreases with respect to the untuned case as is shown in Figure 46. The additional peak due to the DOF of the PID is at 176 rad/s for the tuned case.

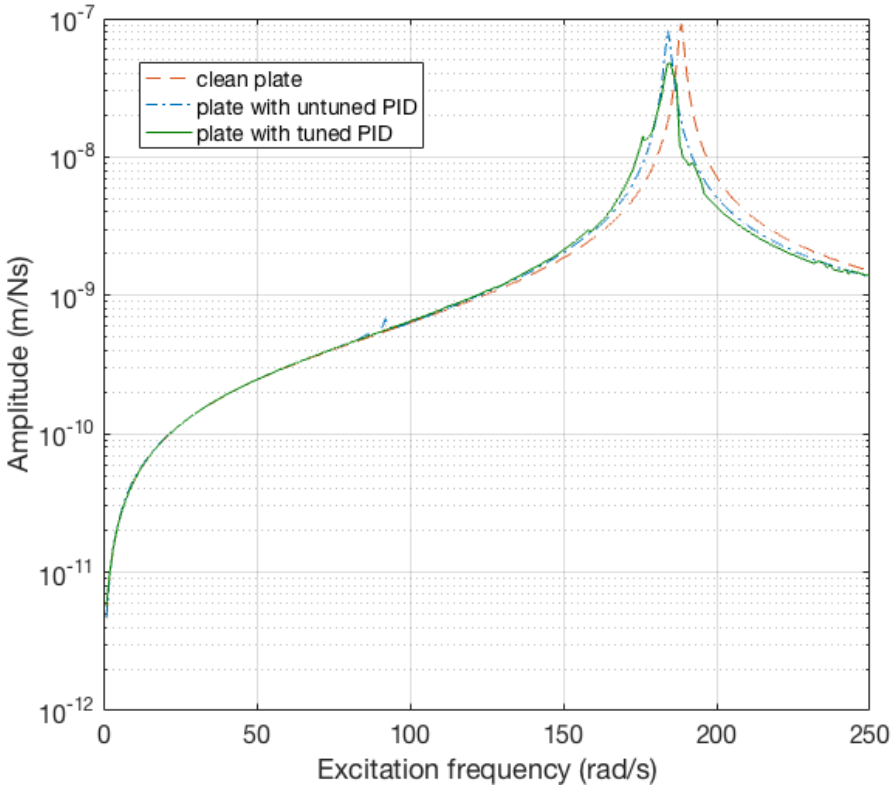

Figure 46: Velocity amplitude (normalized by the forcing amplitude) vs. excitation frequency of the plate under harmonic excitation.

Figure 47 shows the velocity amplitude ratios of the clean plate to the plate with a PID attached to the center under harmonic excitation for both untuned and tuned cases. Note that this is not the same as the metric of the performance (velocity ratio) of the PID because they are not RMS velocities. However, it is also a measure of response reduction. The effect of tuning is prominent at the natural frequency of the clean plate, 188 rad/s. At this point, the velocity amplitude ratio of the untuned PID is 5.02 whereas it reaches 7.95 for the tuned PID. For both cases, the velocity amplitude ratio is lower for frequencies below 188 rad/s compared to the

frequencies above this point, mainly because when the PID is attached, the natural frequency of the plate decreases and the peak amplitude shifts left on the plot.

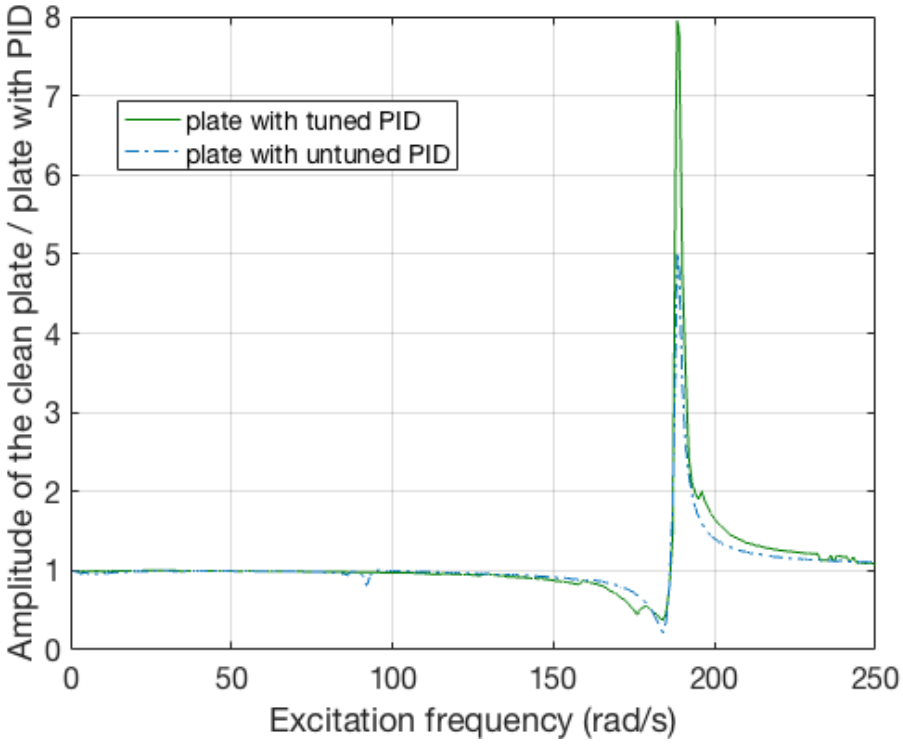

Figure 47: Velocity amplitude of the clean plate / plate with PID comparison of tuned vs. untuned systems at the center of the plate under harmonic excitation.

Figure 48 shows the velocity amplitude (normalized by the forcing amplitude) vs. excitation frequency plots of the plate without a PID (clean plate), and the plate with an untuned and a tuned PID attached to the center under *periodic impulse excitation*. The y-axis shows the ratio of the velocity amplitude at the center of the plate to the forcing amplitude. The plate is excited at $[0.250L_x, 0.375L_y]$. Note that, compared to the harmonic excitation, there are many additional peaks in the same frequency range for all 3 cases: the clean plate, the plate with an untuned PID, the plate with a tuned PID. At ω_n/k where ω_n are the natural frequencies of the plate and $k = 1, 2, 3, \dots$, response amplitudes are greater because of the high relative momentum change of the structure. For example, the first natural frequency of the clean plate is at 188 rad/s

and there are peaks at one half and one third of this frequency. Note that as k increases in ω_n/k, peak amplitudes decrease and they become less prominent. As in harmonic excitation, tuning the natural frequency of the PID to the first natural frequency of the plate decreases the amplitudes of all the peaks with respect to the untuned case.

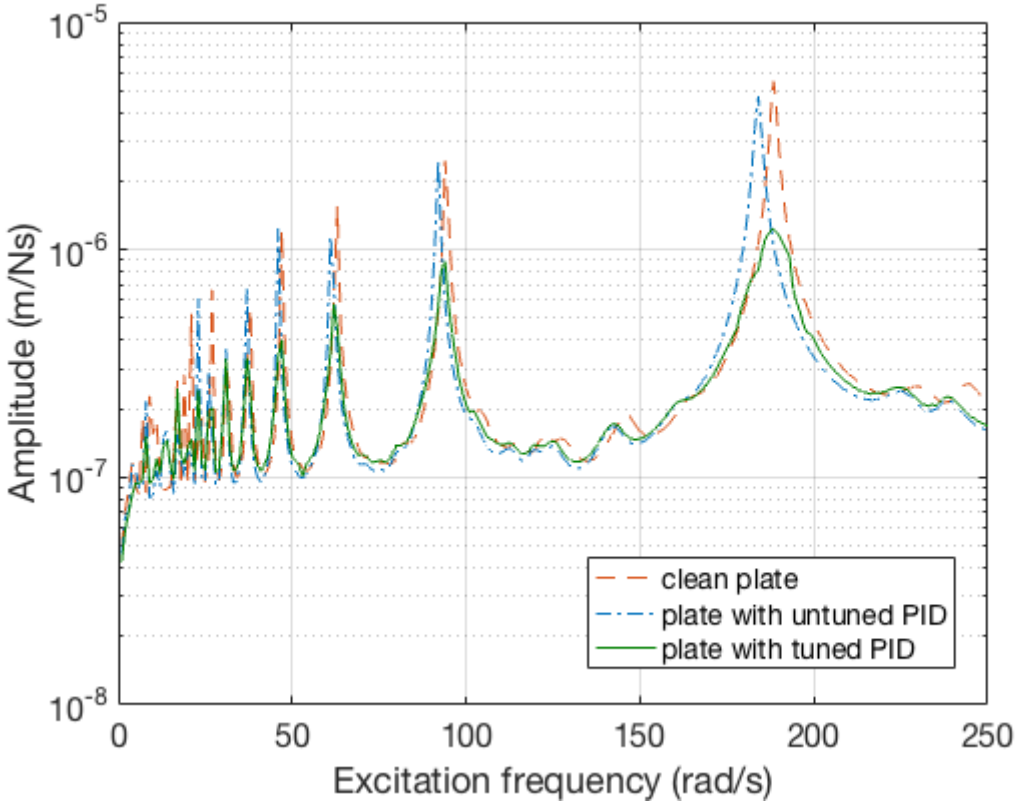

Figure 48: Velocity amplitude (normalized by the forcing amplitude) vs. excitation frequency of the plate under periodic impulse excitation.

Figure 49 is a combination of the data in Figure 48, which shows the velocity amplitude ratios of the clean plate to the plate with a PID attached to the center under periodic impulse excitation for both untuned and tuned cases. Although the system with the tuned PID has lower velocity amplitude ratio for all the peaks in this frequency range, the maximum value occurs for the system with the untuned PID at the natural frequency of the clean plate, 188 rad/s. At this point, the velocity amplitude ratio for the untuned PID is 5.27 whereas it is 4.46 for the tuned

PID. The velocity amplitude ratio for the untuned PID is higher at 188 rad/s because when the untuned PID is attached to the plate, the resonance frequency shifts to 184 rad/s whereas it stays at 188 rad/s for the tuned PID. However, this shift decreases the amplitude ratio to 0.22 for the untuned PID at 184 rad/s where it is 1.29 for the tuned PID. This behavior can be seen for all the other peaks, the untuned PID has the highest and lowest velocity amplitude ratio values around the resonance frequencies. Overall, the average up to 250 rad/s is 1.24 for the untuned PID and 1.17 for the tuned PID for all the excitation frequencies. Standard deviations of velocity amplitude ratios for the untuned and tuned cases are 0.75 and 0.53, respectively. So, it can be concluded that tuning the PID decreases the maximum velocity amplitude at the center of the plate and helps the response to be less sensitive to the frequency variation. However, it may not be necessary if the average velocity amplitudes in the broadband frequency range is considered.

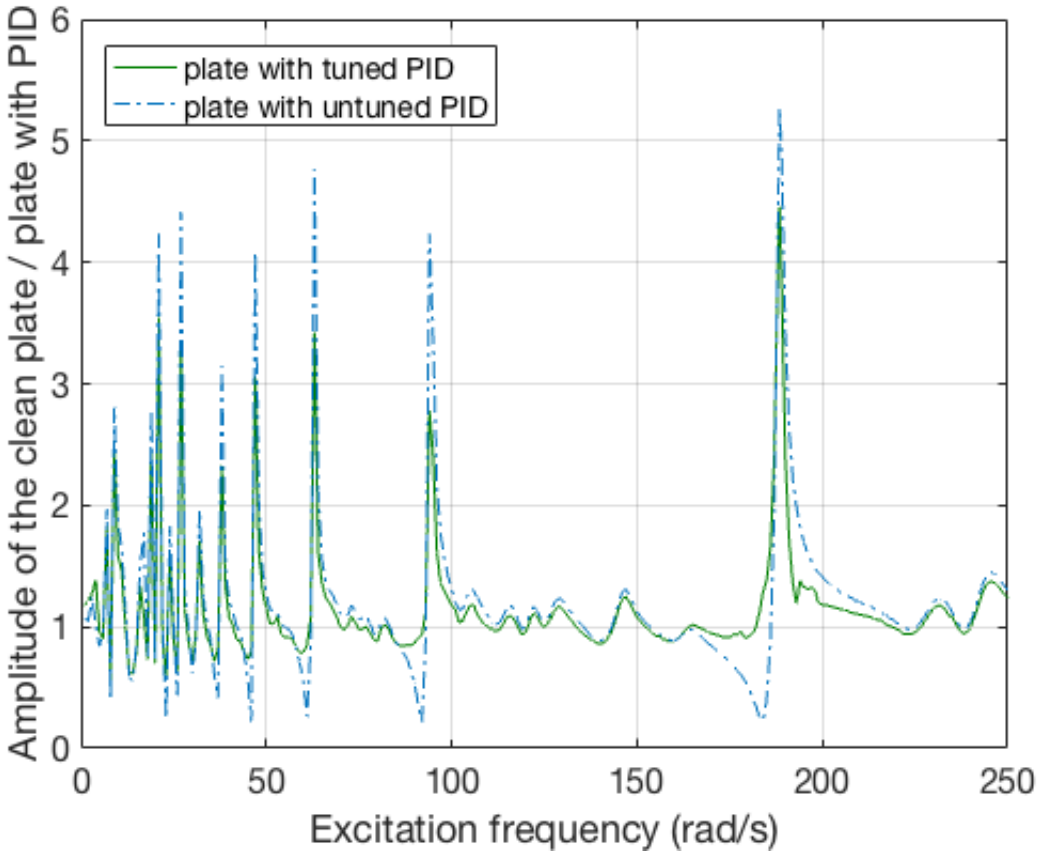

Figure 49: Velocity amplitude of the clean plate / plate with PID comparison of tuned vs. untuned systems at the center of the plate under periodic impulse excitation.

5.3.2 Plotting Plate Mode Shapes to Explore Points with Maximum Displacement Amplitudes

Simulation results of the first 4 mode shapes of the simply supported plate can be seen in Figure 50. Plate length, width and maximum displacements are normalized to 1. When the plate is excited at the frequencies corresponding to the natural frequencies of each of these 4 frequencies using periodic impulse excitation, the deflection shapes of the plate follow similar patterns. For different excitation frequencies, the point with the maximum velocity amplitude varies. Since it is aimed to decrease the velocity amplitudes, an effectiveness grid is used to track the velocities of selected points on the plate.

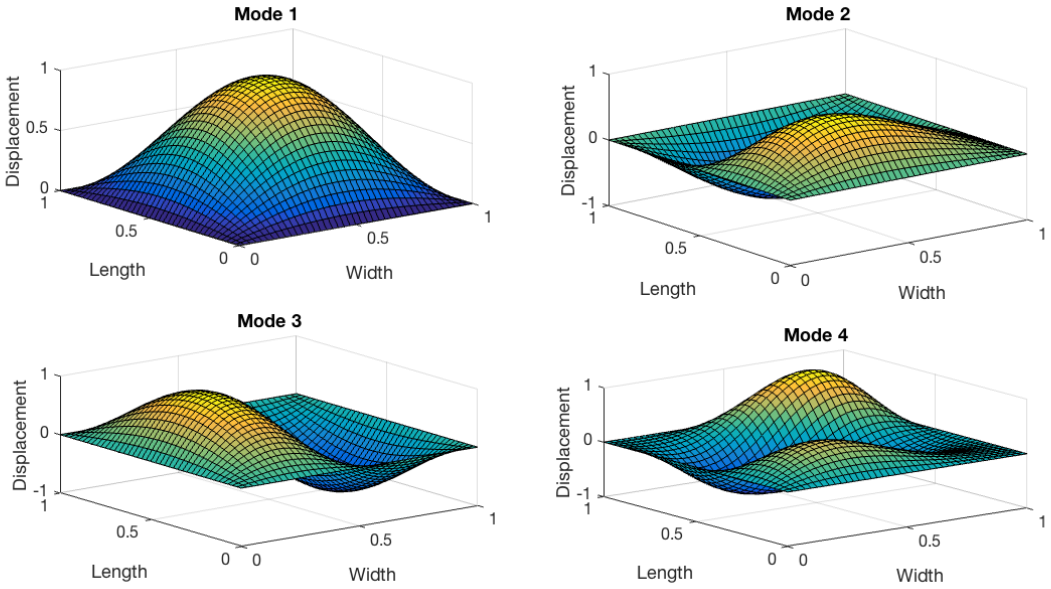

Figure 50: The first 4 mode shapes of the plate without PID.

5.3.3 Effect of PID Location and Excitation Point

In this section, the effect of PID location and excitation point on the PID effectiveness is analyzed. Figure 51 shows a schematic of the top view of the plate with the PID location grid and excitation points. A rectangular plate is considered here and since it is symmetric around its center, the plate is divided into four equal rectangles and the excitation is applied only on one of them. Six different excitation points are chosen, and their locations are shown with red circles in Figure 51. Periodic impulse force is applied only on one of them at a time. For each of these 6 forcing locations, the PID location is varied on the intersection points of the grid in Figure 51. There are 49 PID locations.

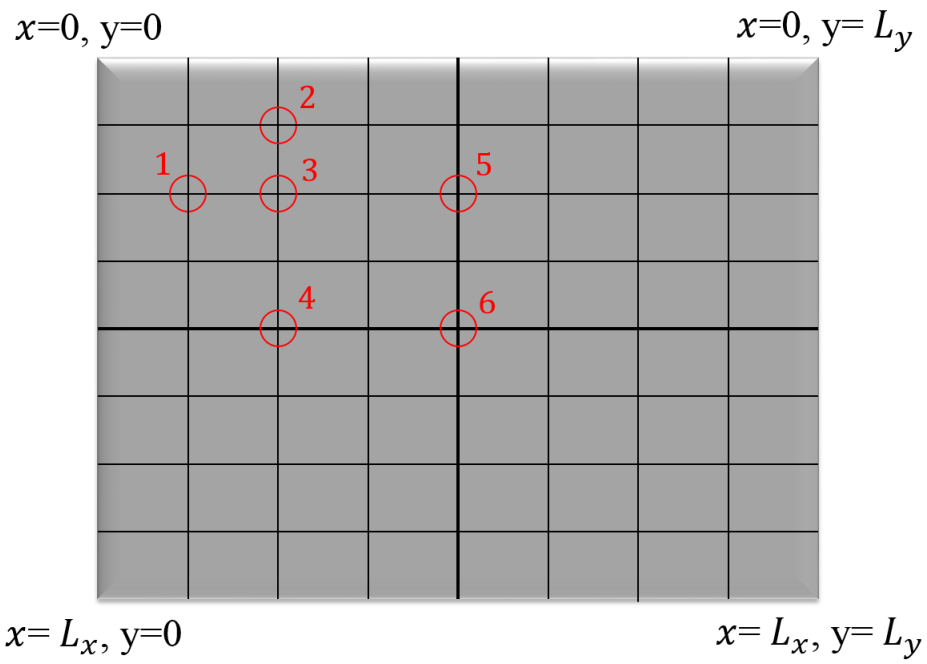

Figure 51: Top view of the plate with the PID location grid.

Figure 52 shows the velocity ratio variation as a function of a single PID location and excitation point on the plate. Excitation points are marked with a red 'x' on the plots. Plate length and width are normalized to 1. Excitation frequency is the first natural frequency of the clean plate. Thus, displacement amplitudes increase from the borders to the center. For all six excitation points, the PID effectiveness (velocity ratio) increases as the PID is moved towards the center. This is because the amplitudes of the points on the plate increases in that direction. For all cases, PID effectiveness is greatest at the center of the plate where the amplitude is maximum.

Since the length of the plate is greater than its width, that is $L_y > L_x$, the six excitation points 1-6 are ordered from the farthest to the closest to the center. From Figure 52, it can be concluded that PID effectiveness increases as the excitation point is moved towards the center

because increasing moment arm of the force relative to the boundary causes higher displacements.

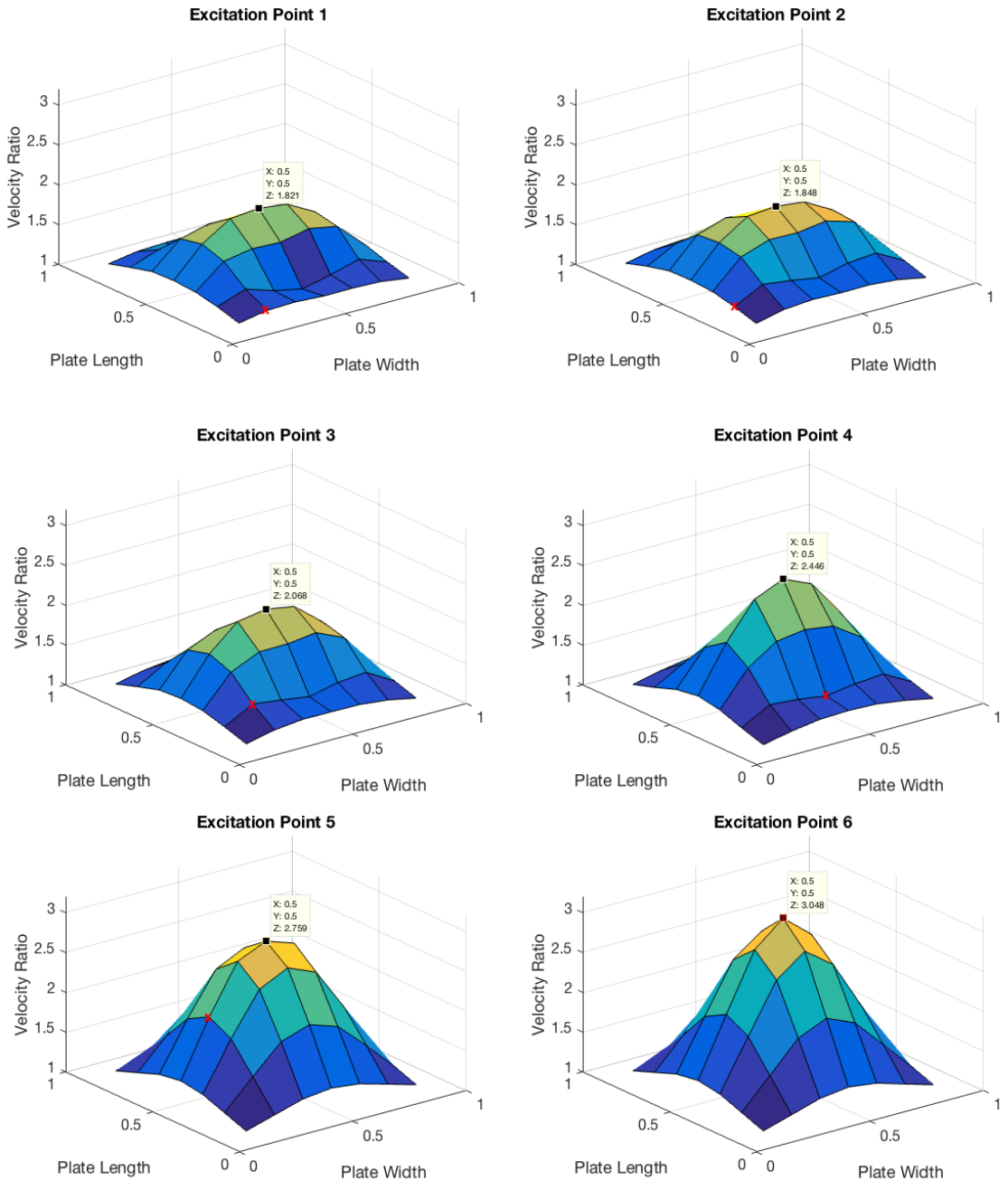

Figure 52: Velocity ratio variation as a function of PID location and excitation point on the plate at the first natural frequency of the plate, with a mass ratio of $m' = 0.1$.

Next, the plate is excited at its second natural frequency to be able to observe the change in PID effectiveness for different excitation frequencies. Before doing that, it may be helpful to remember the second mode shape of the plate which is shown in Figure 50. Note that there is a nodal line, where the plate is motionless, at the half length of the plate, $y = L_y/2$.

Figure 53 shows the velocity ratio variation as a function of a single PID location and excitation point on the plate. It is a repetition of Figure 52 except the excitation frequency is the second natural frequency of the clean plate. Again, the six excitation points and the effectiveness grid in Figure 51 are used. Excitation points are marked with an 'x' on the plots. Plate length and width are normalized to 1. For the excitation points 1, 2, 3, and 4 where the excitation points are away from the nodal line, the PID effectiveness (velocity ratio) is greater for greater displacements in the mode shape, and vice versa. For the excitation points 5 and 6, the excitations are on the nodal line, and the PID effectiveness is greater around the PID location. This is due to the mass loading of the PID.

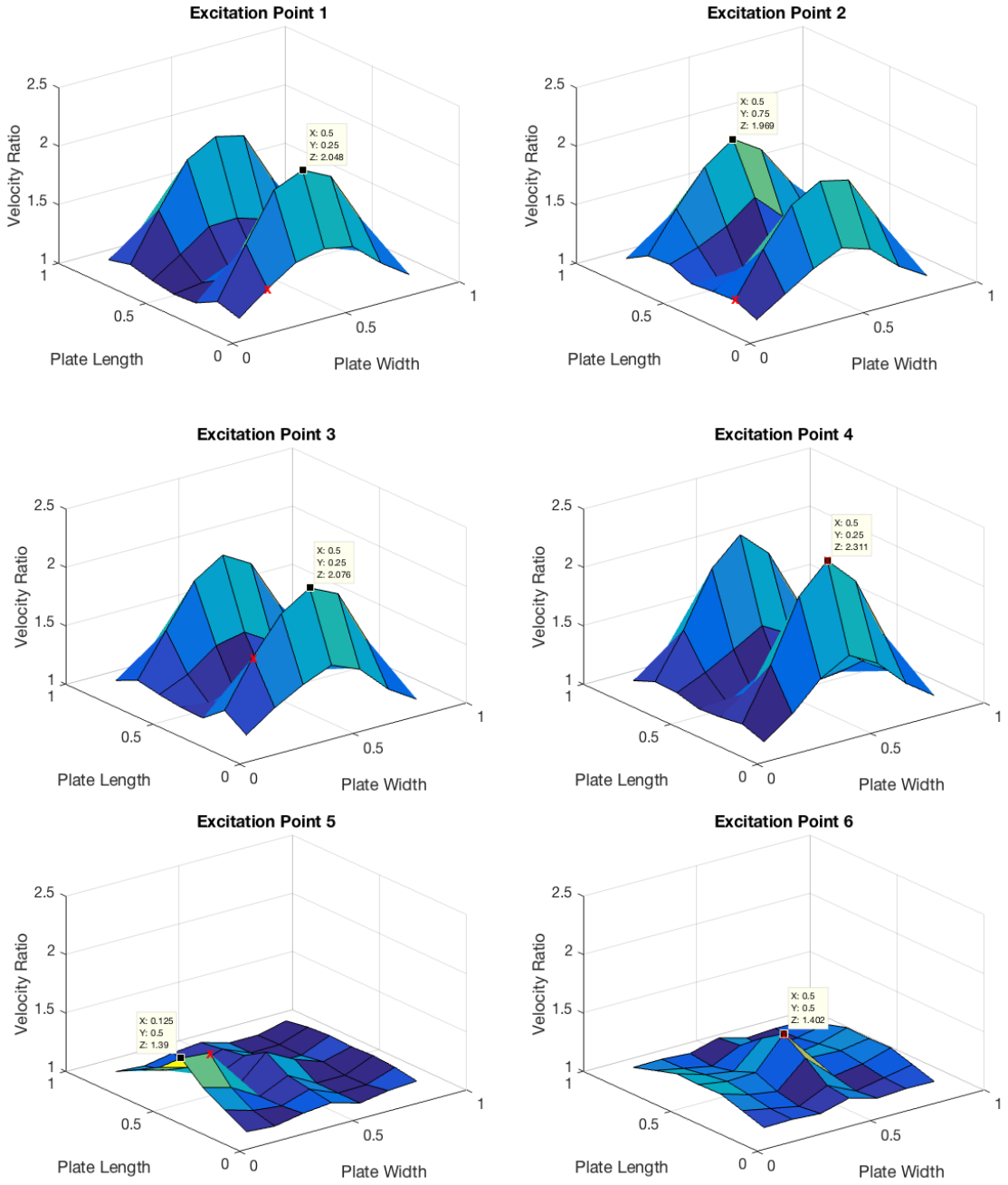

Figure 53: Velocity ratio variation as a function of PID location and excitation point on the plate at the second natural frequency of the plate, with a mass ratio of $m' = 0.1$.

Figure 54 shows the velocity ratio variation as a function of a single PID location and excitation point on the plate at the first natural frequency of the plate, with a mass ratio of $m' = 1$. Higher mass ratio is chosen to be able to observe the effect of the mass loading. The same six excitation points and the effectiveness grid in Figure 51 are used. Excitation points are marked with an 'x' on the plots. Plate length and width are normalized to 1. Remember that, in Figure 40 the system was the same except the mass ratio was lower, $m' = 0.1$, and the center of the plate was the most effective point for all forcing locations. In Figure 54, this is not true. The center of the plate is the most effective point only when the excitation is at the same location, as in the excitation point 6. The excitation points can be divided into two groups. The first group consists of the excitation points 1 and 2. These points are closer to the boundaries compared to the other points. For each of these points, one of the most effective points is a neighbor of the excitation point, which is the furthest to the boundary. This means, when the excitation is relatively 'closer' to the boundary, the PID may be placed next to the excitation point away from the boundary. The second group consists of the excitation points 3, 4, 5, and 6. For these 4 points, the excitation point is one of the most effective points on the plate. Thus, the PID may be placed at the excitation point for greater effectiveness. In general, being 'closer' to the boundary depends on the plate dimensions and the mass ratio. To embrace both cases, it can be concluded from Figure 54 that when the mass ratio is high, placing the PID closer to the excitation point increases the effectiveness.

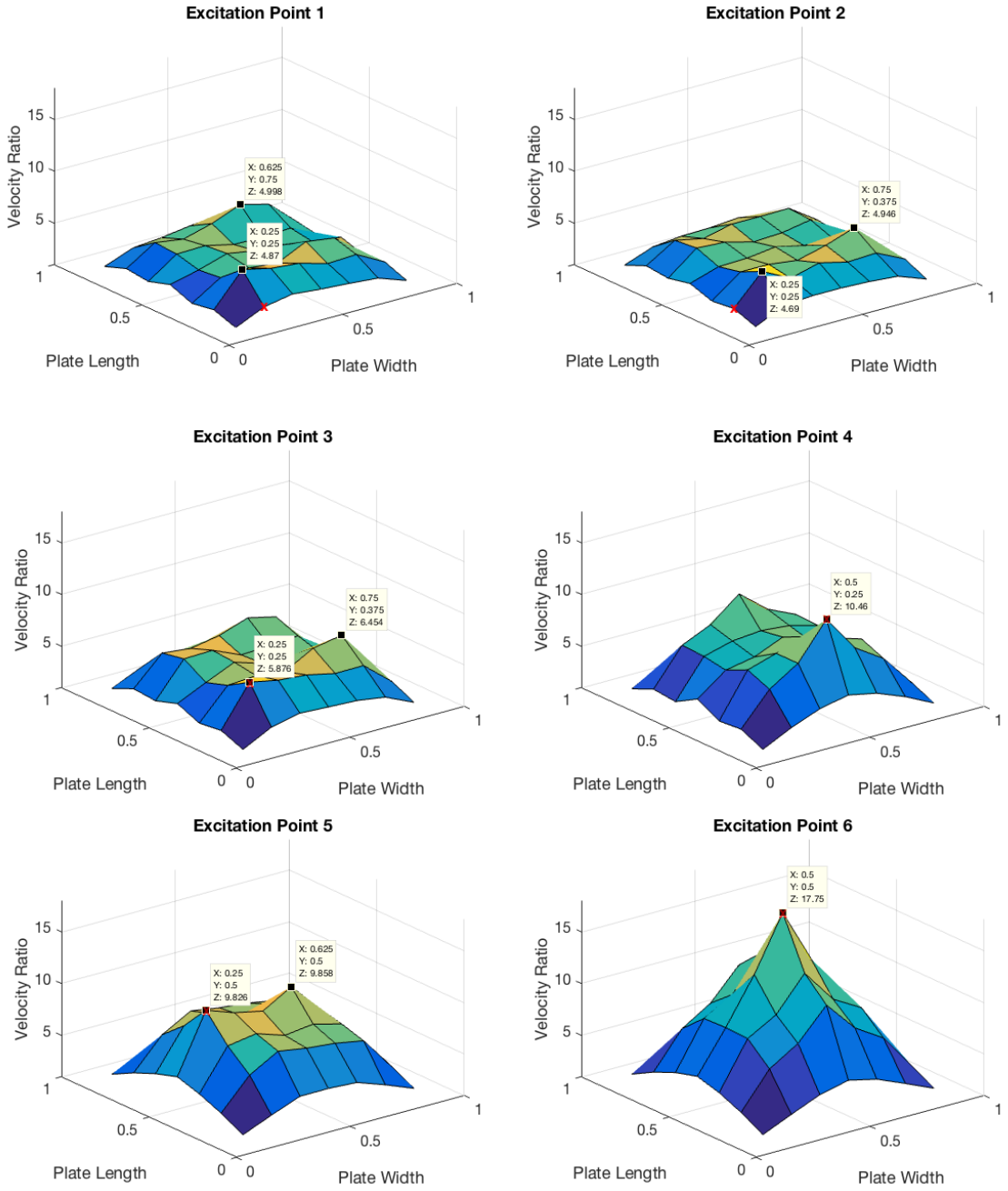

Figure 54: Velocity ratio variation as a function of PID location and excitation point on the plate at the first natural frequency of the plate, with a mass ratio of $m' = 1$.

Figure 55 shows the velocity ratio variation as a function of a single PID location and excitation point on the plate at the second natural frequency of the plate, with a mass ratio of $m' = 1$. The same six excitation points and the effectiveness grid in Figure 51 are used. Excitation points are marked with an 'x' on the plots. Plate length and width are normalized to 1. Again, the excitation points can be divided into two groups. The first group, with the excitation points 1 and 2, is closer to the boundaries compared to the other points. For each of these points, the most effective point is a neighbor of the excitation point, which is the furthest to the boundary. The second group consists of the excitation points 3, 4, 5, and 6. For these points, the excitation point is the most effective point on the plate. Thus, the PID may be placed at the excitation point for greater effectiveness.

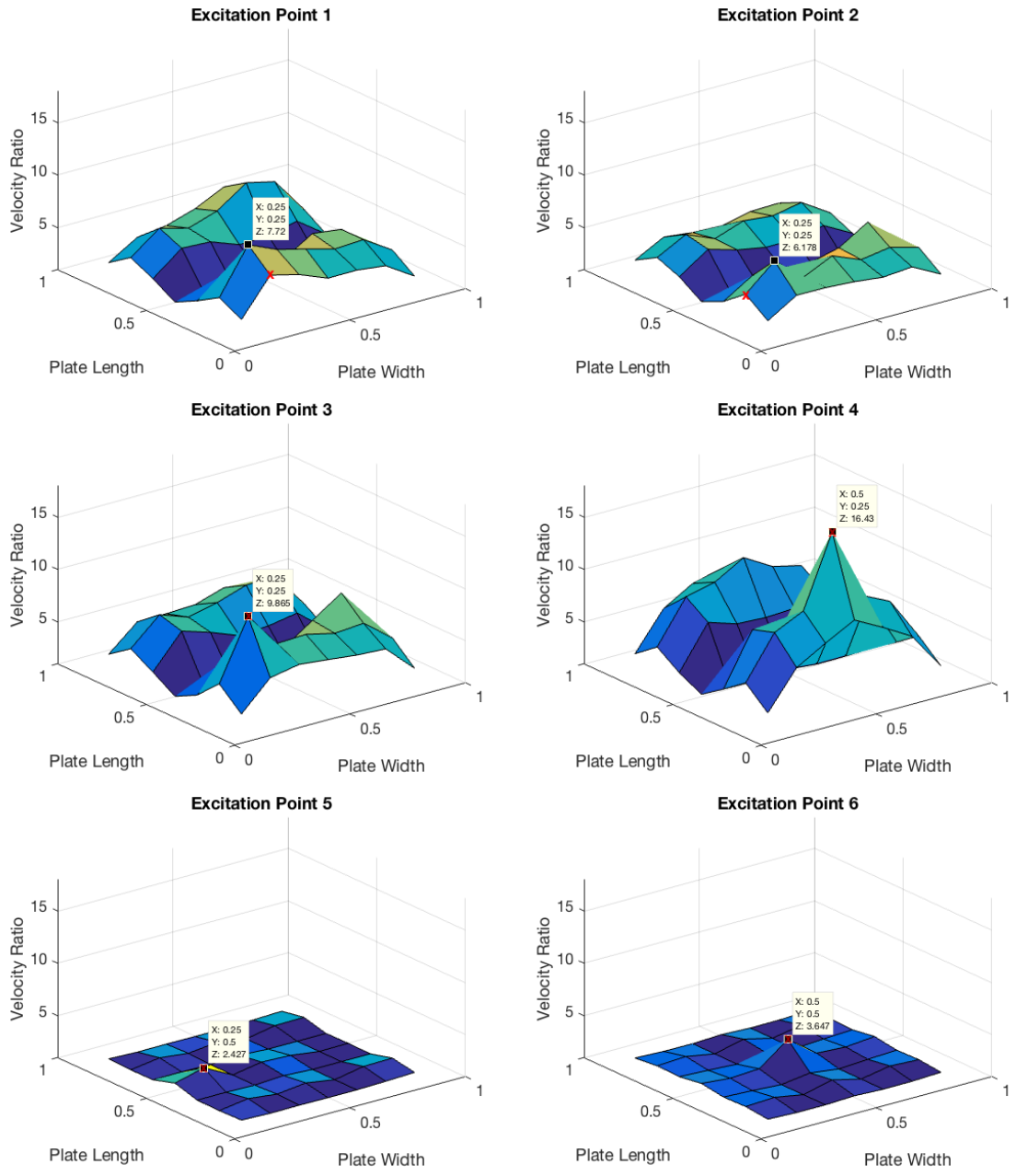

Figure 55: Velocity ratio variation as a function of PID location and excitation point on the plate at the second natural frequency of the plate, with a mass ratio of $m' = 1$.

To sum up the results in Figures 9-13, when the mass ratio is relatively lower as in Figure 9 and 11, excitation frequency and the resultant operational deflection shape becomes important for the optimum PID location in terms of the effectiveness. For example, if the plate is excited at its first natural frequency, the center point is the most effective point for all forcing locations. However, if the plate is excited at its second natural frequency, the center point is on the nodal line, and is a poor choice for PID location. In general, the points with the greatest velocities on the corresponding deflection shape give the greatest efficiency. The only exception is when the plate is excited from a point on the nodal line, the PID should be placed near the excitation point.

When the mass ratio is relatively higher, the optimum PID location does not depend on the excitation frequency. If the excitation point is close to the boundaries, PID is most effective on the other side of the excitation with respect to the boundary. If the excitation point is away from the boundaries, the excitation point is the most effective location for the PID.

For low mass ratios, the advantage from the deflection shape is more dominant with respect to the mass loading. As the mass ratio is increased, the mass loading becomes more dominant. This is demonstrated with the following example.

Figure 56 shows the effect of the mass ratio variation on the velocity ratio for two different PID locations; P1 at $[0.50L_x, 0.50L_y]$ and P2 at $[0.50L_x, 0.25L_y]$. These are the excitation points 4 and 6 in Figure 40 and Figure 54. For both cases, the plate is excited at the location of P2. The effectiveness of P1 (the center point) is superior to P2 for the low mass ratios. As the mass ratio is increased, the increase in the effectiveness of P2 is higher with respect to the increase in the effectiveness of P1. At $m' = 0.45$, the effectiveness for both locations is the same. Then as the mass ratio is further increased, the effectiveness of P2 surpasses the effectiveness of P1. This intersection point is the balance point where the

advantage from the deflection shape and the effect of mass loading on the effectiveness is equal. The intersection point is not a function of the forcing amplitude, as the variation of the forcing amplitude didn't change the intersection point. However, it is a function of structural damping. As the damping in the plate increases, the intersection point also increases.

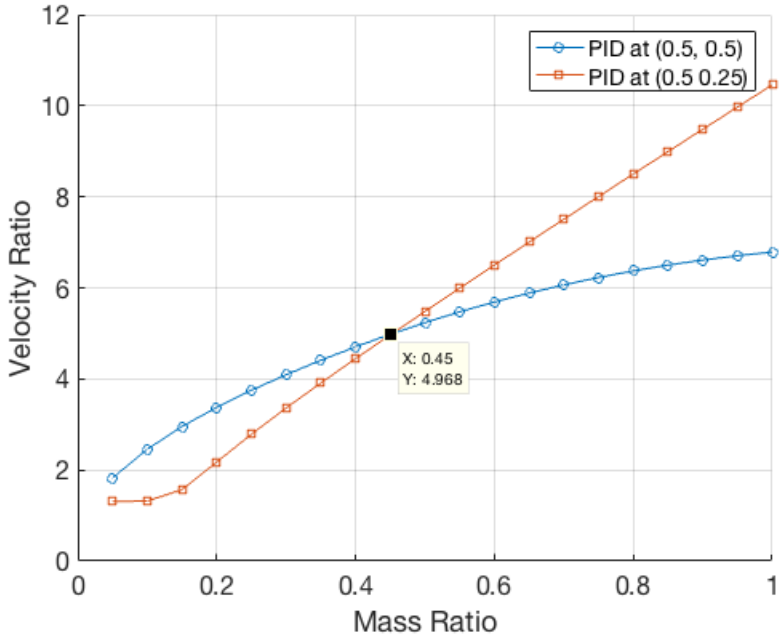

Figure 56: The effect of the mass ratio variation on the velocity ratio for two different PID locations and $\lambda = 5.0\times10^{-5}$.

As an example, Figure 57 shows the effect of the mass ratio variation on the velocity ratio for the same two PID locations in Figure 56 but with a different proportionality constant that is used to model the structural damping, $\lambda = 2.0\times10^{-4}$ which is 4 times of the proportionality constant in Figure 56. Note that, overall effectiveness values are less compared to the lower structural damping because the effectiveness is a relative metric comparing the system velocities without the PID and with the PID. If the system without the PID has higher damping, the effectiveness will be lower for the same PID mass. The intersection point in Figure 57 is just above $m' = 0.65$. This means the effect of mass loading becomes more important than the

advantage from the deflection shape *at a higher mass ratio*. When the two systems in Figure 56 and Figure 57 are compared, it can be concluded that the effect of mass loading is more important for lightly damped systems, and decreases with increasing structural damping compared to the excitation frequency and the resultant deflection shape.

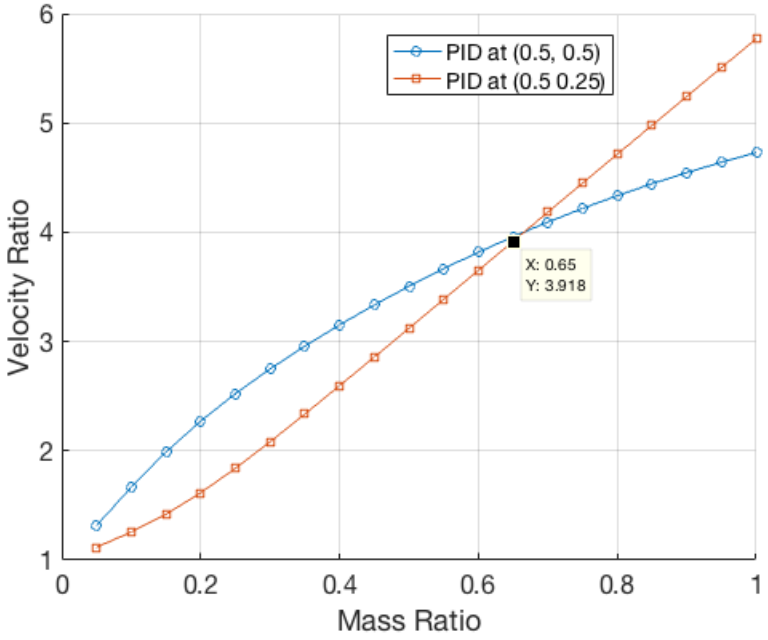

Figure 57: The effect of the mass ratio variation on the velocity ratio for two different PID locations and $\lambda = 2.0 \times 10^{-4}$.

5.3.4 Damping Measure vs. Mass Measure

Figure 58 shows the damping measure given in Eq. 5.58 for a periodic impulse excitation at $[0.25L_x, 0.375L_y]$ and a PID at $[0.50L_x, 0.50L_y]$. Note that the damping measure is directly related to the damping effect because if the damping in the system increases the change in the kinetic energy over a cycle would be higher. The excitation frequency is the first natural frequency of the clean plate. After the initial transients die out, the damping measure value for the clean plate is lower compared to the plate with a PID because the only damping mechanism is the intrinsic damping of the plate. When a PID with a mass ratio of 0.1 is attached, the

damping measure value increases. When the mass ratio is increased to 1.0, the damping measure value also increases. This is because the particle spends more time stuck to the enclosure compared to the low mass ratio case which increases the damping.

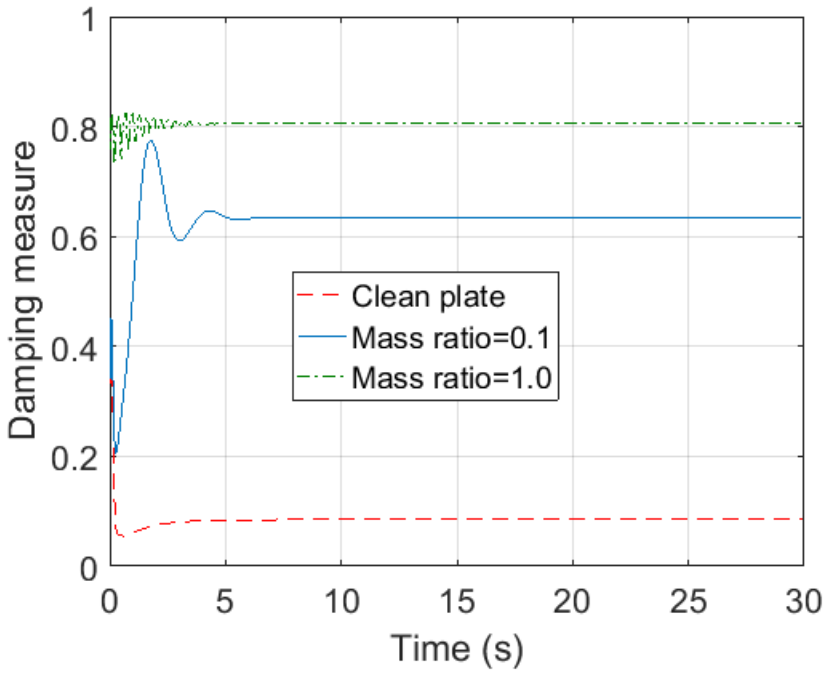

Figure 58: The damping measure for a periodic impulse excitation at $[0.25L_x, 0.375L_y]$ and a PID at $[0.50L_x, 0.50L_y]$.

Figure 59 shows the mass measure given in Eq. 5.59 for a periodic impulse excitation at $[0.25L_x, 0.375L_y]$ and a PID at $[0.50L_x, 0.50L_y]$. Note that there is an inverse relation between the mass measure and the mass ratio because when the mass ratio increases (higher PID mass) the change in velocity and the kinetic energy at the impulse excitation would be lower. The excitation frequency is the first natural frequency of the clean plate. After the initial transients die out, the mass measure value for the clean plate is higher compared to the plate with a PID. When a PID with a mass ratio of 0.1 is attached, the mass measure value decreases. When the mass ratio is increased to 1.0, the further decrease in the mass measure value shows the increased mass effect.

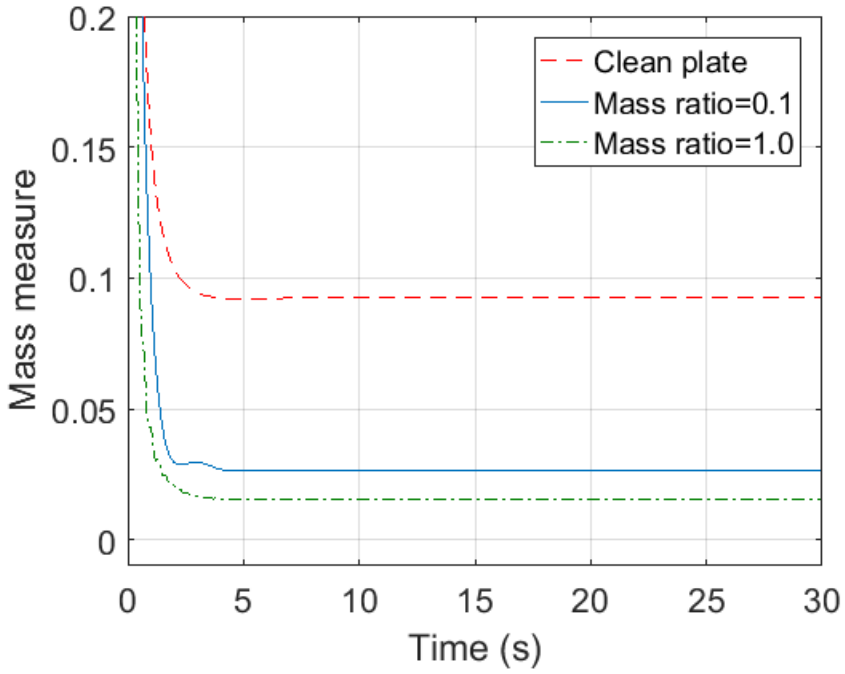

Figure 59: The mass measure for a periodic impulse excitation at $[0.25L_x, 0.375L_y]$ and a PID at $[0.50L_x, 0.50L_y]$.

Figure 60 shows the damping measure results for a periodic impulse excitation at $[0.50L_x, 0.50L_y]$ and a PID at $[0.50L_x, 0.50L_y]$. Note that the excitation and the PID are at the same location which is the most effective point at this frequency. The excitation frequency is the first natural frequency of the clean plate. After the initial transients die out, the damping measure trends are similar to Figure 58. The damping measure is lowest for the clean plate, and increases with increasing mass ratio. However, when the PID is attached, the damping measure values are lower for both the low and high mass ratio cases compared to Figure 58 where the excitation and the PID are at separate locations. The reason is when the PID and the excitation is at the same location, there is less relative motion at the excitation point which would decrease the PID damping.

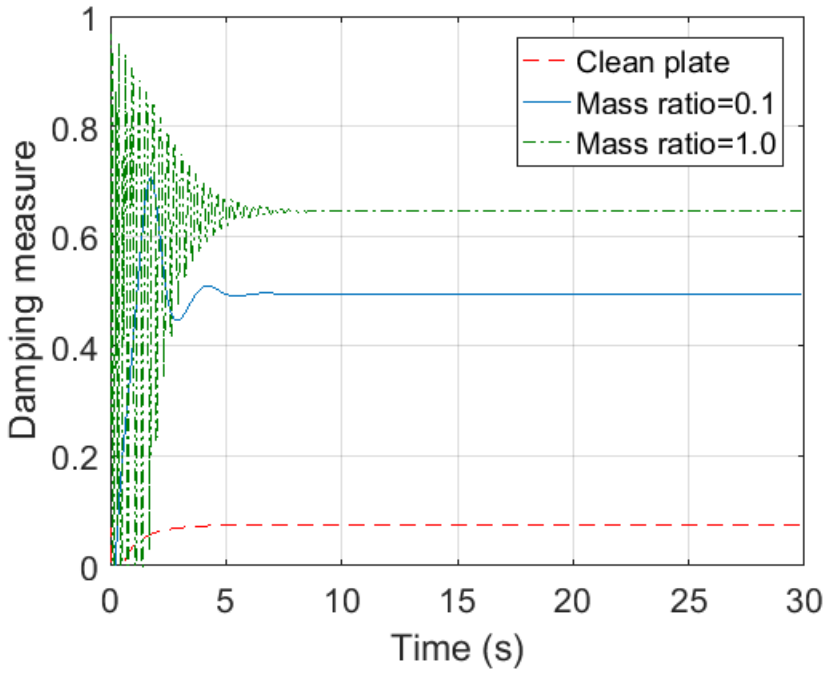

Figure 60: The damping measure for a periodic impulse excitation at $[0.50L_x, 0.50L_y]$ and a PID at $[0.50L_x, 0.50L_y]$.

Figure 61 shows the mass measure results for a periodic impulse excitation at $[0.50L_x, 0.50L_y]$ and a PID at $[0.50L_x, 0.50L_y]$. Again, the excitation and the PID are at the same location which is the most effective point at this frequency. After the initial transients die out, the mass measure value decreases with increasing mass ratio similar to Figure 59. However, when the PID is attached, the mass measure values are lower compared to Figure 59 where the excitation and the PID are at separate locations. This shows the increased effect of the PID mass when it is closer to the excitation point.

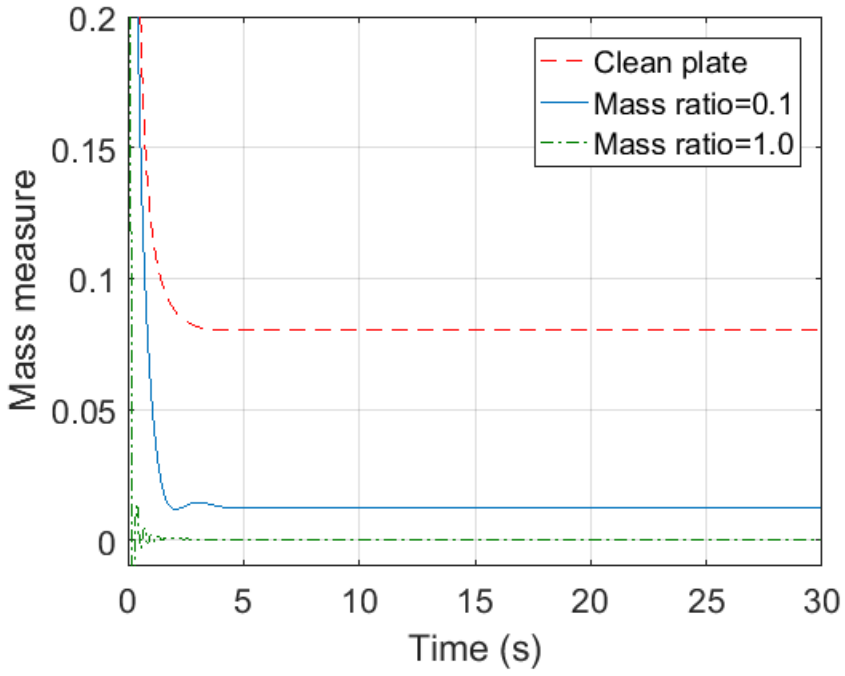

Figure 61: The mass measure for a periodic impulse excitation at $[0.50L_x, 0.50L_y]$ and a PID at $[0.50L_x, 0.50L_y]$.

Figure 62 shows the damping measure results for a periodic impulse excitation at $[0.25L_x, 0.375L_y]$ and a PID at $[0.25L_x, 0.375L_y]$. Note that the excitation and the PID are at the same location but not at the center of the plate this time. The excitation frequency is the first natural frequency of the clean plate. After the initial transients die out, the damping measure value for the clean plate is the minimum like the previous cases in Figure 58 and Figure 60. When the PID with a low mass ratio is attached, the damping measure value increases. However, the damping measure value decreases with increasing mass ratio unlike the previous cases. The reason is since the PID and the excitation is at the same location and closer to the boundaries, increased mass ratio is *pinning* the plate at the PID location and there is minimum motion at that point.

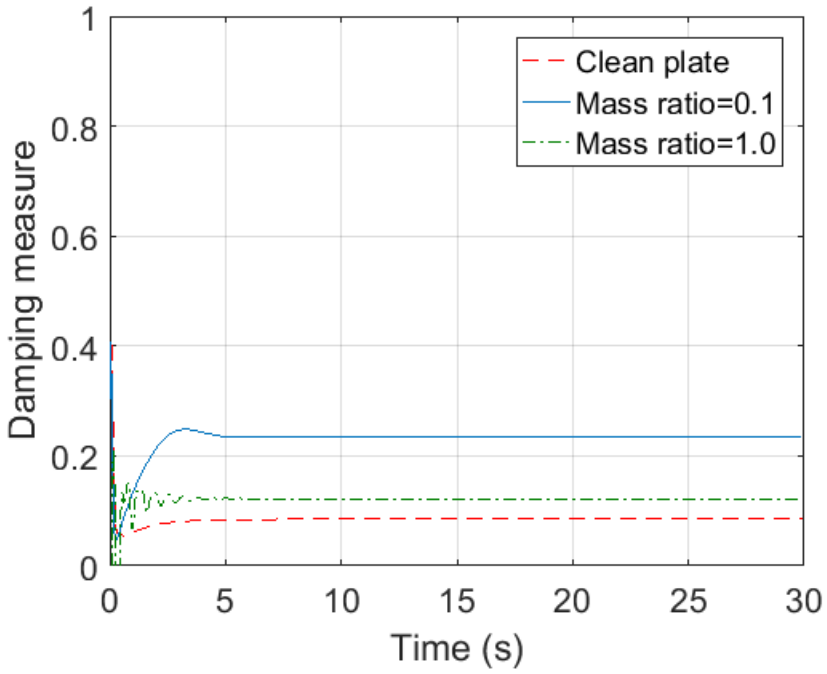

Figure 62: The damping measure for a periodic impulse excitation at $[0.25L_x, 0.375L_y]$ and a PID at $[0.25L_x, 0.375L_y]$.

Figure 63 shows the mass measure results for a periodic impulse excitation at $[0.25L_x, 0.375L_y]$ and a PID at $[0.25L_x, 0.375L_y]$. Again, the excitation and the PID are at the same location but not at the center of the plate. After the initial transients die out, the mass measure value decreases with increasing mass ratio similar to Figure 59 and Figure 61. When the PID is attached, the mass measure values are higher compared to Figure 61 where both the excitation and the PID are at the center of the plate. This shows that when the excitation and the PID are at the same location, the mass effect depends on the location over the plate.

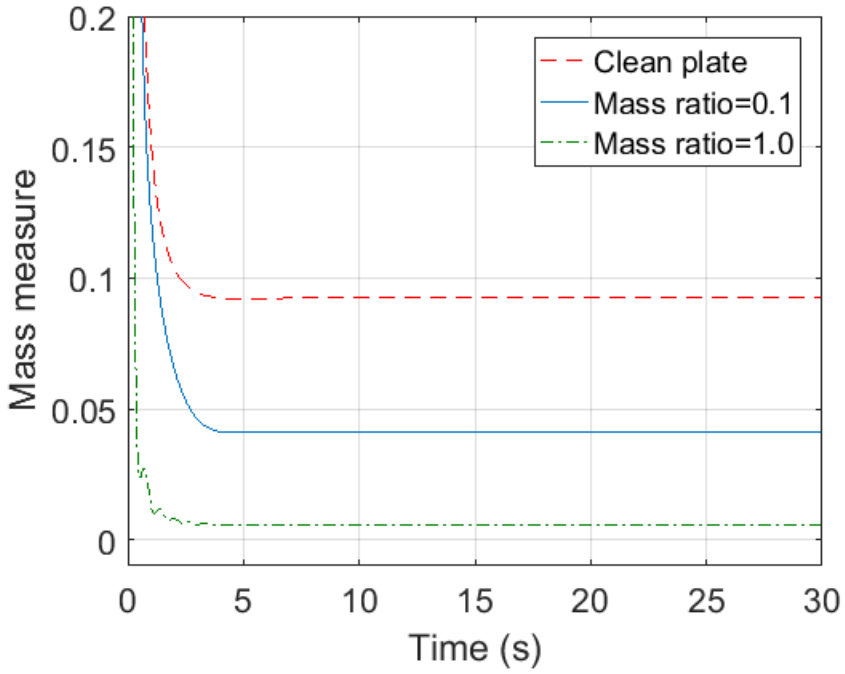

Figure 63: The mass measure for a periodic impulse excitation at $[0.25L_x, 0.375L_y]$ and a PID at $[0.25L_x, 0.375L_y]$.

5.3.5 Effect of Forcing Amplitude

In this section, 4 different plate systems are considered with (i) a single PID, (ii) an array with 4 PIDs (2 by 2 grid), (iii) 6 PIDs (2 by 3 grid), and (iv) 9 PIDs (3 by 3 grid). The single PID is at the center of the plate. The locations of the PIDs for (ii)-(iv) are shown in Figures 15-17, respectively. The PIDs are represented with yellow rectangles and the spacing is constant which is 2 cm. For all cases the plate is excited at $[0.250L_x, 0.375L_y]$ and the excitation frequency is the first natural frequency of the clean plate, that is $\omega' = 1$. The PIDs are uniformly filled and the mass ratio is constant ($m' = 0.1$) for all cases. For example, for 4 PIDs, the mass of a single PID (both m_s and m_p) is one fourth of the 1 PID case.

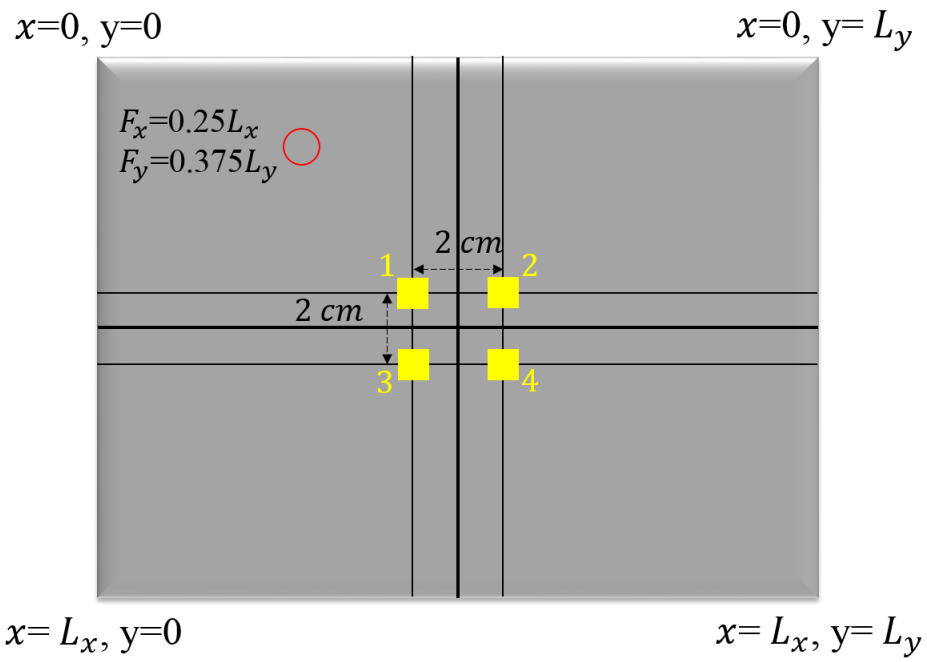

Figure 64: A schematic of the top view of the modeled simply supported plate with 4 PIDs.

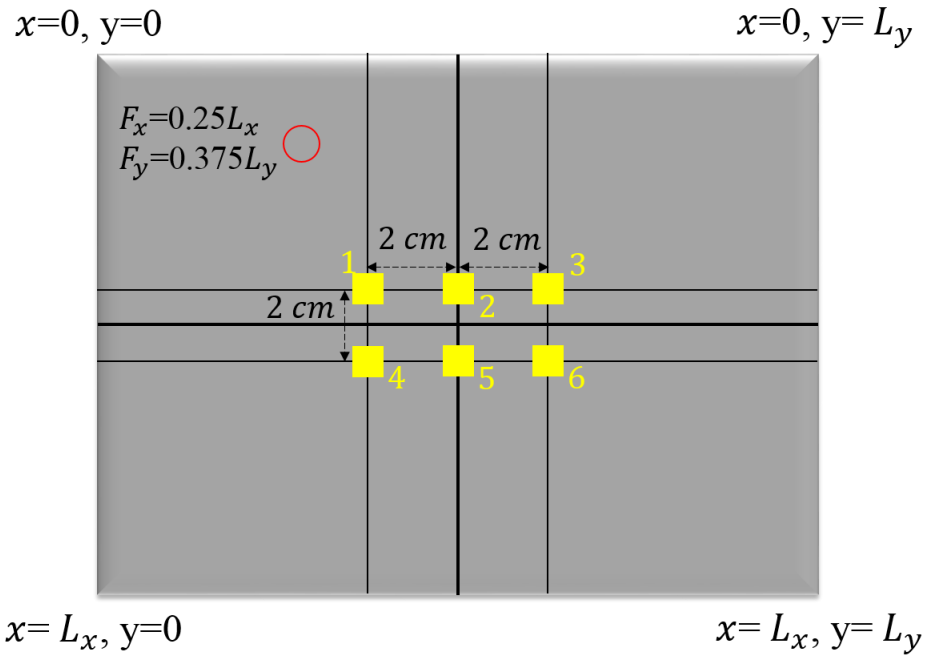

Figure 65: A schematic of the top view of the modeled simply supported plate with 6 PIDs.

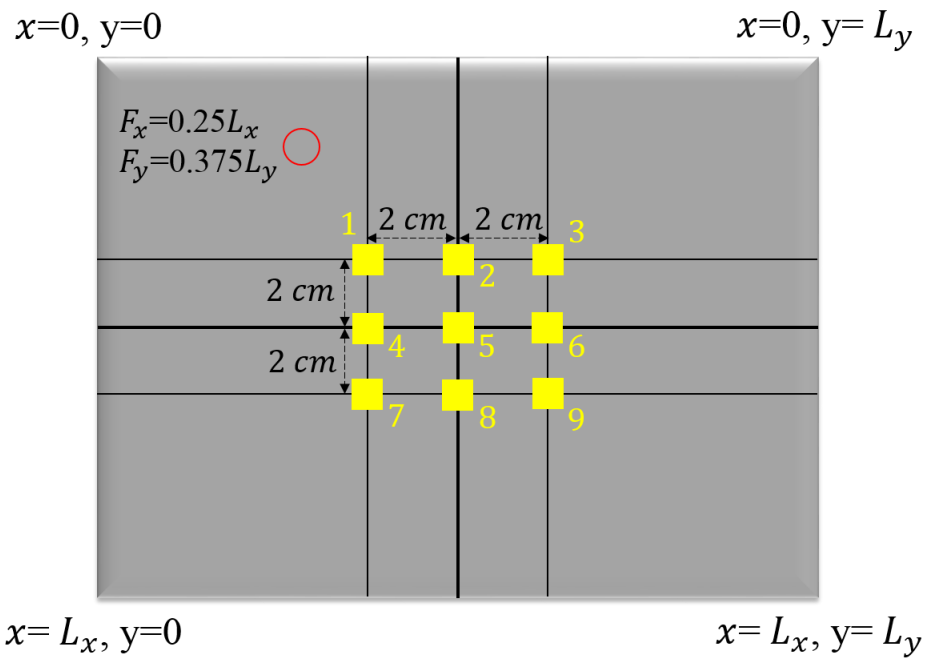

Figure 66: A schematic of the top view of the modeled simply supported plate with 9 PIDs.

Figure 42 shows the velocity ratio variation as a function of the dimensionless forcing amplitude for all 4 cases, (i)-(iv). The single PID at the center has the lowest effectiveness (velocity ratio). As the number of PIDs increases, the effectiveness also increases. Note that, the single PID is at its most effective location for all forcing locations. Therefore, having increasing performance as the number of PIDs increases means in terms of the effectiveness, it is better to have multiple PIDs spread out across the plate instead of a single PID at a single location. Also note that, multiple PIDs are uniformly filled in Figure 42 and the performance may be further improved after optimizing the gap clearances.

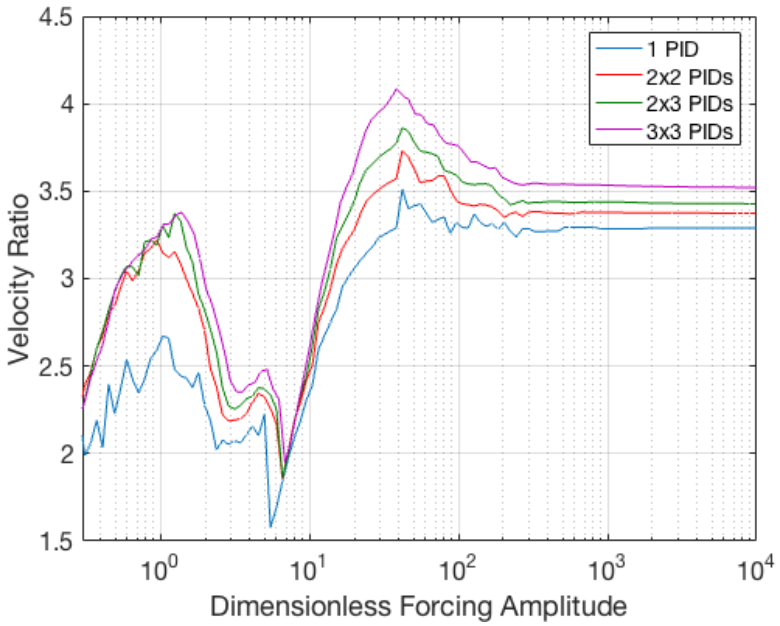

Figure 67: Velocity ratio variation as a function of the dimensionless forcing amplitude for excitation point at $[0.250L_x, 0.375L_y]$.

5.3.6 Effect of Particle Mass to Enclosure Mass Ratio for a Constant Mass Ratio

In this section, the effect of particle mass to enclosure mass ratio (m_p/m_s) for a constant mass ratio, m', is analyzed. Recall that the mass ratio is the ratio of sum of the particle mass and the enclosure mass to the mass of the plate, that is,

$$m' = \frac{m_p + m_s}{m}. \tag{5.60}$$

Therefore, for a constant mass ratio, the particle mass is inversely related to the enclosure mass.

Figure 68 shows the velocity ratio variation as a function of the dimensionless forcing amplitude for various m_p/m values for a single PID with $m' = 0.1$. For very low and high forcing amplitudes, the most effective case is where the particle mass is minimum which also means that enclosure mass is maximum. For these cases, the relative motion between the particle and the enclosure is minimum when they are in contact. Therefore, the energy dissipated by the dampers is also minimum. The high effectiveness is a result of both the change in natural frequency of the plate and increased impedance at the point of the excitation due to the addition of the enclosure mass. As the particle mass increases, overall velocity ratio decreases but the peaks at around $f' = 10^{-2}$ and $f' = 10^{0}$ becomes more prominent. The most effective case is when the particle mass is maximum ($m_p/m = 0.09$). The forcing amplitude is just above $f' = 10^{-2}$ and at this point effectiveness decreases as m_p/m is decreased to 0.07 and 0.05. As the particle mass further decreased, the effect of the enclosure mass becomes more important than the effect of the particle mass.

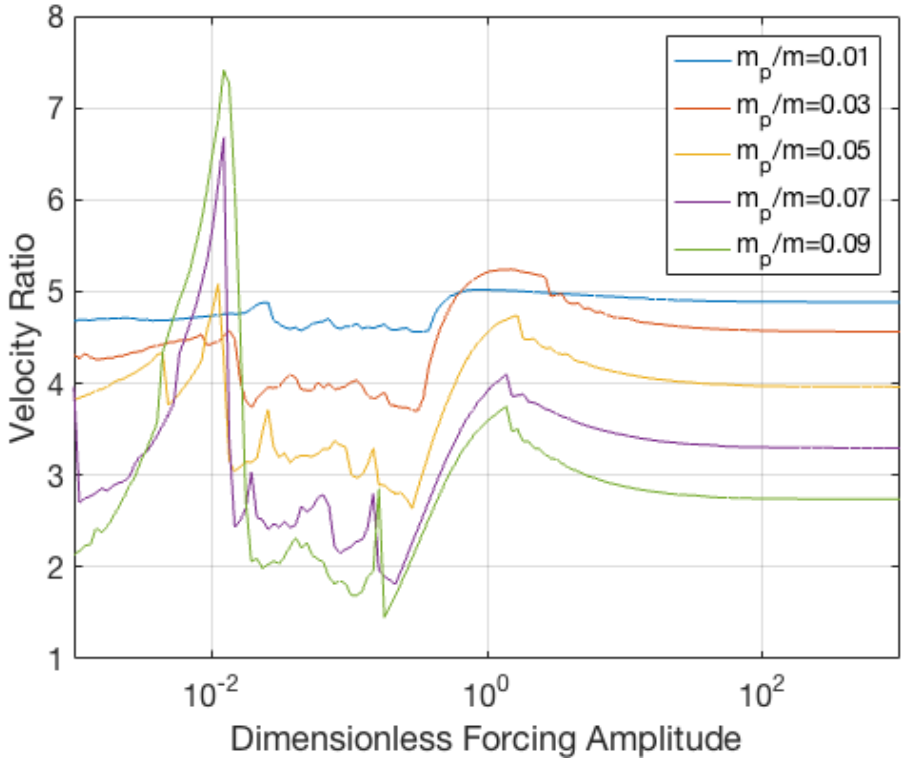

Figure 68: Velocity ratio variation as a function of the dimensionless forcing amplitude for various m_p/m values for $m' = 0.1$.

Figure 69 shows the velocity ratio variation as a function of the dimensionless forcing amplitude for various m_p/m values for a single PID with $m' = 1$. Compared to the system in Figure 68, both the particle mass and the enclosure mass is much higher this time. For Figure 69, there is almost a perfectly inverse relation between particle mass and the effectiveness. This shows that for a single PID, when the mass ratio is high, the enclosure mass is the driving factor for the effectiveness.

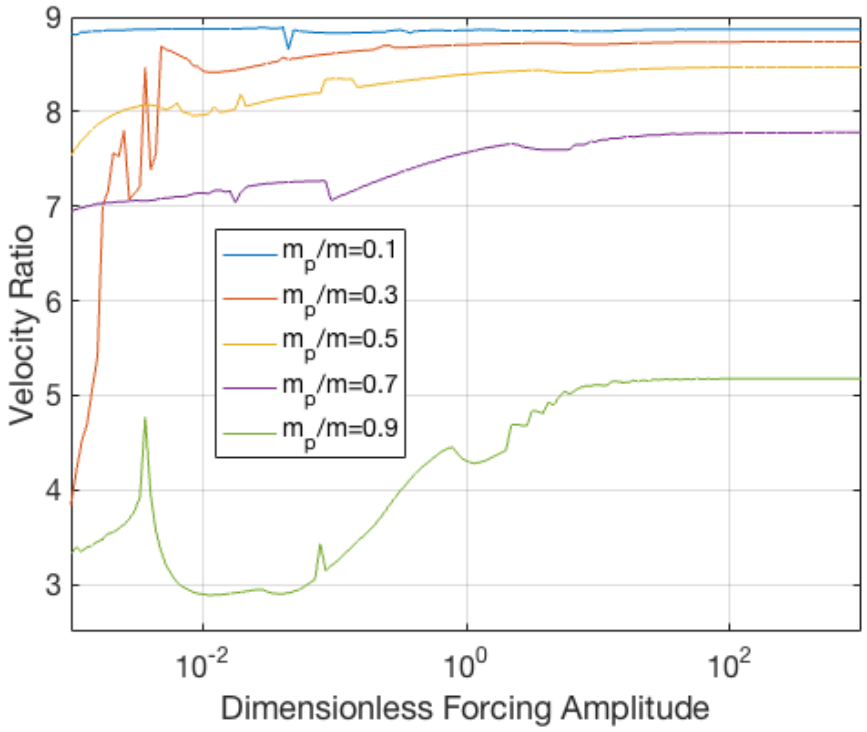

Figure 69: Velocity ratio variation as a function of the dimensionless forcing amplitude for various m_p/m values for $m' = 1$.

5.3.7 Effect of Plate Dimensions

Up to this point, only the plate given in Table 4 was considered. In this section, this plate will be compared to the plate in Table 7. They are named as Plate 1 and Plate 2, respectively.

Table 7: Plate 2 parameters

Parameter	**Value**
Width	1/2 m
Thickness	1.98 mm
Length	2/3 m

Modulus of Elasticity	68.9 GPa
Poisson's Ratio	0.33
Density	2700 kg/m^3

The length and the width of Plate 2 is half, whereas the thickness is one fourth of Plate 1. Plate 2 is less stiff and lighter than Plate 1. The first natural frequency of a simply supported rectangular plate is [59]

$$\omega_{n1} = \pi^2 \sqrt{\frac{D}{\rho}} \left(\frac{1}{L_x^2} + \frac{1}{L_y^2} \right). \tag{5.61}$$

The bending rigidity, D, is proportional to the cube of thickness, h^3. Therefore, the first natural frequencies of both plates are at the same frequency, 30 Hz or 188.50 rad/s.

Figure 70 shows the velocity ratio comparison as a function of the dimensionless forcing amplitude for Plate 1 and Plate 2. The single PID is at $[0.50L_x, 0.50L_y]$ and the plates are excited at $[0.250L_x, 0.375L_y]$. The excitation frequency is the first natural frequency of the plates, that is $\omega' = 1$. The mass ratio is $m' = 0.1$ for both cases.

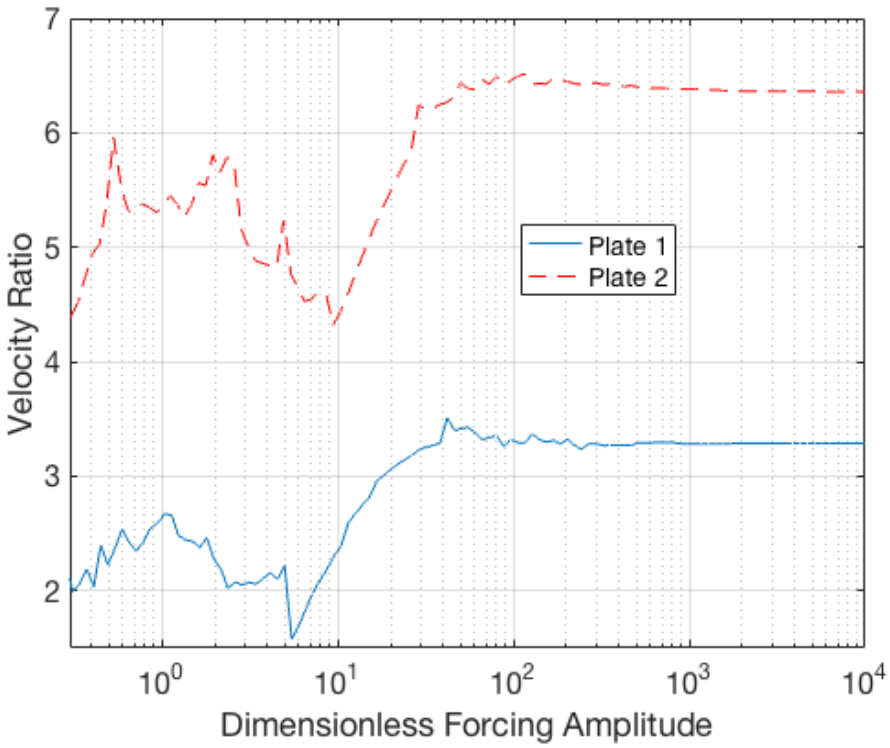

Figure 70: Velocity ratio comparison as a function of the dimensionless forcing amplitude for Plate 1 and Plate 2.

Both plates shows similar trends with respect to the forcing amplitude variation. However, velocity ratio amplitudes are approximately twice for Plate 2. The reason is the proportional damping assumption for the plate. Remember that the damping matrix of the plate without the PIDs is defined as

$$C_{plate} = \lambda (M_{plate} + K_{plate}) . \tag{5.62}$$

Since Plate 2 is less stiff and lighter than Plate 1, the structural damping of the plate is lower with respect to Plate 1. Therefore, the effect of the PID is relatively higher.

CHAPTER 6

OPTIMIZATION OF DISTRIBUTED ARRAY OF PARTICLE IMPACT DAMPERS

6.1 Overview

This chapter details the optimization of the gap clearances of a distributed array of particle impact dampers attached to continuous systems, specifically a cantilever beam and simply supported plate. Two parameters were found to be particularly important in terms of their effects on the velocity ratio: PID location and gap clearance. Optimum PID locations were already analyzed and the results for cantilever beam and simply supported plate were presented in Chapter 4 and Chapter 5, respectively. It was also presented in this study that there is an optimum gap clearance for PIDs attached to vibrating structures. The optimum gap clearance is greater for higher forcing amplitude. Note that, until now PID arrays used in this study are assumed to be uniformly filled. The research objective in this chapter is to answer the question: *Do uniformly or non-uniformly filled arrays of closely-spaced PIDs provide a better and more robust velocity ratio for an arbitrary excitation point in the broadband frequency range?*

The chapter is organized as follows: First section describes the optimization technique employed and explains the objective function. The final section presents the results from the optimization of the beam and the plate, respectively.

6.2 Optimization Method

Nonlinear behavior of particle damping is one of the main reasons modeling and optimizing PIDs is a challenge. A genetic algorithm is a commonly used method for finding global optimum for highly nonlinear problems. Genetic algorithms are based on a natural

selection process in which a population of candidate solutions is generated at the first iteration and better points are stochastically selected to form the next population. The iteration continues until a termination condition is satisfied. In this study, a genetic algorithm function is used for the optimization problem.

An objective function is the expression of the main goal of the optimization process which is either to be minimized or maximized. The objective function herein is to maximize PID effectiveness, the velocity ratio. The velocity ratio is defined as

$$\psi = \frac{(v_{rms})_{noPID}}{(v_{rms})_{PID}}, \tag{6.1}$$

where $(v_{rms})_{noPID}$ is the RMS velocity of the base mass without an impact damper, and $(v_{rms})_{PID}$ is the RMS velocity of the base mass with an impact damper. $\psi > 1$, $\psi < 1$ and $\psi = 1$ correspond to increased effectiveness, decreased effectiveness and no impact, respectively. Because the base without the PIDs is not affected by the optimization process, the objective can be restated as minimizing the RMS velocity of the base with the PIDs.

There are as many parameters (gap clearances) in the optimization process as the number of PIDs. Note that if all of the gap clearances are equal, the PIDs are uniformly filled. For the analyses in this chapter, 4 PIDs are used for both the beam and the plate optimization. The number of PIDs is decided by considering the computation time which increases exponentially with increasing number of PIDs. For the beam, 4 PIDs are placed at different locations along the length of the beam. For the plate, 4 PIDs are placed as a 2 by 2 array at different locations on the plate. The gap clearances are intended to be optimized for different PID locations and mass ratios. 6 separate excitation points are considered, and the average velocity ratio is observed.

The genetic algorithm is a heuristic algorithm that allows for moving out of a local optimum, however it does not guarantee that the global optimum will be found. For possible improvement of the beam and the plate optimization, a 2-opt improvement heuristic algorithm is employed after the genetic algorithm. 2-opt is a local search algorithm which compares the results obtained by swapping the values of each parameter pair. Comparing the optimum gap clearances depending on the PID locations and excitation point is important for the interpretation of the results and 2-opt is a quick way to check and possibly improve the optimum solutions. Results showed that, swapping the gap clearances made a difference for some cases.

The genetic algorithm allows for the setting of constraints for the solution. Equality, inequality, lower bound, upper bound, nonlinear, or integer constraints can be used depending on the problem. In this study, only lower and upper bounds are set to limit the solution domain. The objective function is to minimize the RMS velocity of the base with the PIDs. The objective function is also called the "fitness function" in a genetic algorithm and the value of the fitness function is known as "fitness". Various stopping criteria can be employed for a genetic algorithm and 2 of them are observed in this study: maximum time and function tolerance. The maximum time condition is met when the algorithm stops after running for a preset amount of time. The function tolerance condition is met when the algorithm runs until the average relative change in the fitness value is less than "function tolerance".

6.3 Cantilever Beam Optimization Results

The genetic algorithm optimization described above was used to optimize the gap clearances of 4 PIDs applied to a vibrating cantilever beam. Beam parameters, which are shown in Table 8, are the same as the beam used in Chapter 4.

Table 8: Beam parameters

Parameter	**Value**
Width	30 mm
Thickness	5 mm
Length	1 m
Modulus of Elasticity	200 GPa
Density	7800 kg/m^3

The optimization algorithm was considered for an impulse excitation with a frequency equal to the first natural frequency of the beam, $\omega' = 1.6$ different forcing locations were used, and the velocity ratio was averaged. By this means, it is aimed to have the optimum velocity ratio for an arbitrary forcing location. The 6 forcing locations used are given in Table 9.

Table 9: Forcing locations for the cantilever beam

Forcing Location	**Value**
1st	1 m
2nd	5/6 m
3rd	4/6 m
4th	3/6 m
5th	2/6 m

6^{th}	1/6 m

In the following analyses, 2 different PID location conditions are considered. The location conditions are named B1 and B2, and are shown in Figure 71 and Figure 72, respectively. For both conditions, the PID spacing is constant at 4 cm. Thus, the array of PIDs spans 16% of the total beam length. In B1, PIDs are placed starting from the tip of the beam. B2 represents the condition where the PIDs are moved with the excitation point. Therefore, the PID locations are not constant. The 4 PIDs are centered on a sample excitation points as shown in Figure 72.

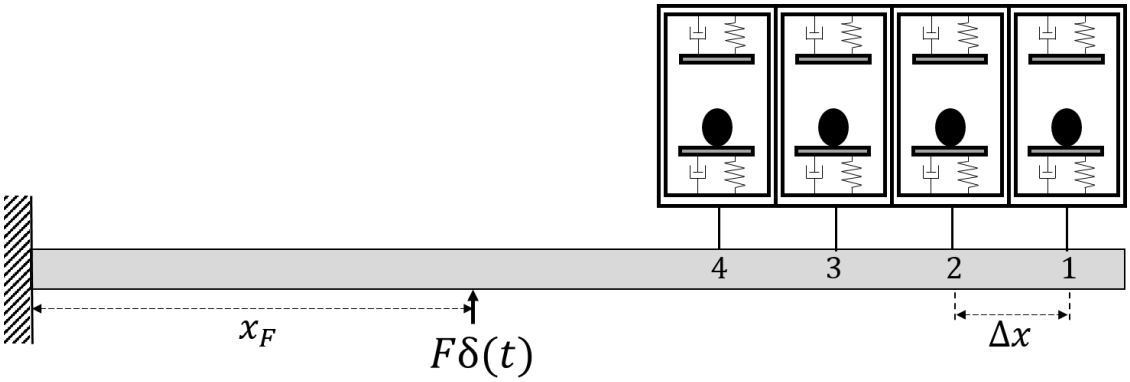

Figure 71: B1 PID locations

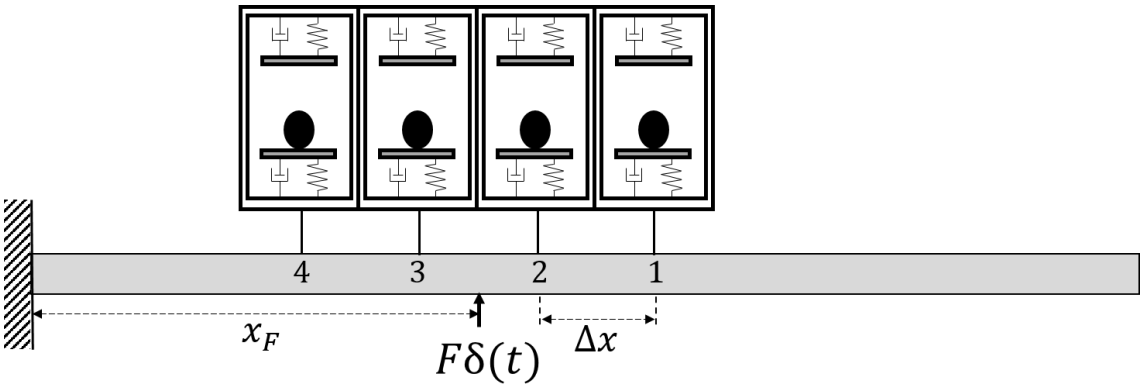

Figure 72: B2 PID locations

6.3.1 Optimizing Gap Clearances of the PIDs with Low Mass Ratio, $m' = 0.1$

Table 10 shows the optimization results of 4 PIDs for B1 case with a mass ratio, $m' = 0.1$. The objective function is the average value of the $(v_{rms})_{PID}$ of 4 PIDs for 6 different excitation points given in Table 9. Note that $(v_{rms})_{PID}$ is the RMS velocity of the base mass with the PIDs and by minimizing the $(v_{rms})_{PID}$ the velocity ratio is maximized. The value of the objective function is named as "fitness" for simplicity. The genetic algorithm improved the fitness from 794.8 mm/s to 427.3 mm/s with respect to the uniform gap clearances. The 2-opt heuristic algorithm did not change the optimum solution.

Table 10: Optimization results for B1 case with $m' = 0.1$.

Parameter	**Value**
Uniform fitness (mm/s)	794.8
GA fitness (mm/s)	427.3
GA gap clearances (mm)	8.3, 56.8, 3.0, 18.8
2-opt gap clearances (mm)	8.3, 56.8, 3.0, 18.8
2-opt fitness (mm/s)	427.3
Overall optimum fitness (mm/s)	427.3

Table 11 shows the optimization results of 4 PIDs at B2 case with a mass ratio, $m' = 0.1$. The fitness for uniformly filled PIDs is 1253.5 mm/s. The genetic algorithm did not find a better solution than the uniform case. 2-opt analysis is not performed because it is redundant with uniform gap clearances.

Table 11: Optimization results for B2 case and $m' = 0.1$.

Parameter	**Value**
Uniform fitness (mm/s)	1253.5
GA fitness (mm/s)	1253.5
GA gap clearances (mm)	41.9, 41.9, 41.9, 41.9
2-opt gap clearances (mm)	Not performed
2-opt fitness (mm/s)	Not performed
Overall optimum fitness (mm/s)	1253.5

The optimization results of B1 and B2 cases both with a low mass ratio shows that B1 has lower optimum fitness. Therefore, PIDs are more effective at the tip of the beam.

6.3.2 Optimizing Gap Clearances of the PIDs with High Mass Ratio, $m' = 1$

Table 12 shows the optimization results of 4 PIDs for B1 case with a mass ratio of $m' = 1$. The genetic algorithm improved the fitness from 762.2 mm/s to 649.7 mm/s with respect to the uniformly filled PIDs. The 2-opt heuristic algorithm did not change the optimum result. When the uniform fitness is compared to the B1 case with the low mass ratio, this case has a lower uniform fitness which means a higher velocity ratio. However, optimum fitness for the low mass ratio case is lower, indicating that increasing the mass ratio may decrease the effectiveness if the PID locations are not optimum.

Table 12: Optimization results for B1 case and $m' = 1$.

Parameter	Value
Uniform fitness (mm/s)	762.2
GA fitness (mm/s)	649.7
GA gap clearances (mm)	72.3, 3.4, 3.0, 29.4
2-opt gap clearances (mm)	72.3, 3.4, 3.0, 29.4
2-opt fitness (mm/s)	649.7
Overall optimum fitness (mm/s)	649.7

Table 13 shows the optimization results of 4 PIDs for B2 case with a mass ratio, $\mathrm{m}' = 1$. The fitness for uniformly filled PIDs is 759.8 mm/s and the optimum fitness was found using the GA and the 2-opt algorithm, which is 392.4 mm/s. Note that, B2 was the less effective case for the low mass ratio analysis. However, for the high mass ratio, it has the best overall velocity ratio when compared to the previous 3 cases, with low and high mass ratios. This result confirms that, when the mass ratio is high, placing the PIDs around the excitation point increases effectiveness.

Table 13: Optimization results for B2 case and $m' = 1$.

Parameter	Value
Uniform fitness (mm/s)	759.8
GA fitness (mm/s)	392.4
GA gap clearances (mm)	8.3, 83.7, 0.1, 39.7

2-opt gap clearances (mm)	8.3, 0.1, 83.7, 39.7
2-opt fitness (mm/s)	355.0
Overall optimum fitness (mm/s)	355.0

6.3.3 Frequency Variation for Optimum and Uniform Gap Clearances

Figure 73 compares the velocity ratio variation of the 4 PIDs with optimum vs. uniform gap clearances as a function of frequency for B1 case with $m' = 0.1$. The velocity ratio is the performance metric and a higher velocity ratio is desirable. The y-axis is given in logarithmic scale for a better representation. Note that when the mass ratio is low, B1 is the case with optimum PID locations. The excitation frequency is varied between 15-35 rad/s since the first natural frequency of the clean beam is 25.7 rad/s. The peak velocity ratios are 44.5 for the optimum case and 39.5 for the uniform case. This is also the point with greatest difference in favor of the optimum case. On the other hand, the uniform case is slightly more effective for most of the frequencies. The greatest advantage in terms of the velocity ratio of the uniform case is 0.3. As a result, it can be said that the advantage in the optimum case is signidicant around the resonance frequency. For other frequencies, the difference is relatively small and generally in favor of the uniform case.

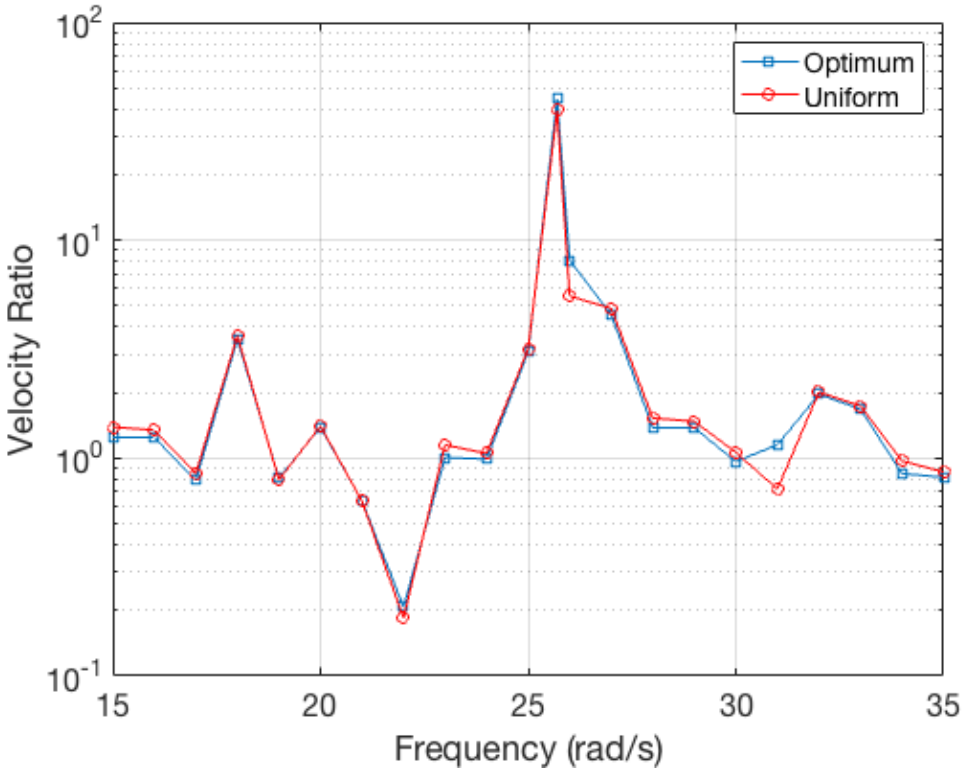

Figure 73: Velocity ratio variation as a function of frequency for the B1 case with $m' = 0.1$.

Figure 74 shows the velocity ratio variation of the 4 PIDs with optimum vs. uniform gap clearances as a function of frequency at B2 for $m' = 1$. Note that B2 is the case with optimum PID locations for the high mass ratio. The excitation frequency is varied between 15-35 rad/s as in the low mass ratio case. The PIDs with optimum gap clearances have higher velocity ratios for all frequencies in the range except for 34 rad/s. At this frequency, the velocity ratio of the uniform case is 0.06 more than the optimum case. The greatest difference is in favor of the optimum case at the peak frequency, 25.7 rad/s, where the velocity ratio is 53.5 for the optimum case and 22.4 for the uniform case. Average velocity ratio for all frequencies in the range is 4.5 for the optimum case, whereas it is 1.9 for the uniform case. Although the optimum case has higher overall velocity ratio, most significant difference is around the optimization frequency.

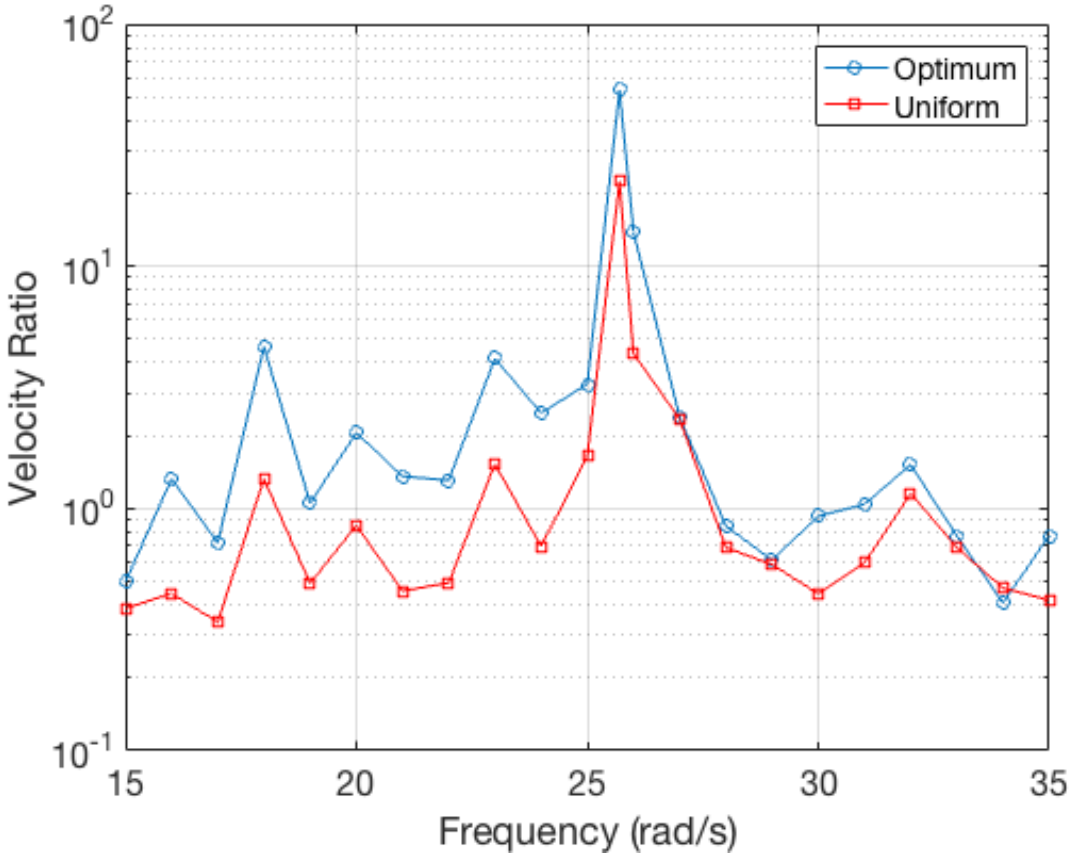

Figure 74: Velocity ratio variation as a function of frequency for the B2 case with $m' = 1$.

6.4 Simply Supported Plate Optimization Results

The genetic algorithm was used to optimize the gap clearances of 4 PIDs attached to a vibrating simply supported plate. A method similar to that used in the beam optimization was employed for the plate optimization. Plate parameters, which are shown in Table 14 are the same with Plate 2 in Chapter 5.

Table 14: Plate 2 parameters

Parameter	**Value**
Width	1/2 m

Thickness	1.98 mm
Length	2/3 m
Modulus of Elasticity	68.9 GPa
Poisson's Ratio	0.33
Density	2700 kg/m^3

The optimization algorithm was considered for an impulse excitation with a frequency equal to the first natural frequency of the plate, $\omega = 30\ Hz$. This frequency is also the average operation frequency of the intended excitation mechanism, rivet guns. The dimensions of the plate are chosen to result 30 Hz as the first natural frequency, so that maximum effectiveness may be observed. 6 different forcing locations were used, and the velocity ratio was averaged. By this means, it is aimed to have optimum velocity ratio for an arbitrary forcing location. The forcing locations are shown in Figure 75.

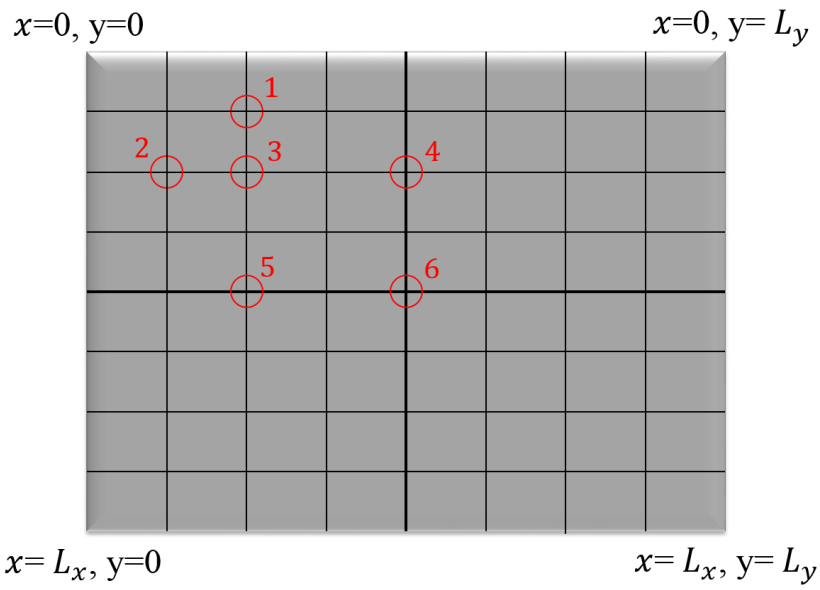

Figure 75: Top view of the plate with forcing locations.

In the following analyses, 3 different PID location cases are considered. They are named as C1, C2, and C3, which are shown in Figure 76-8. PIDs are represented with yellow rectangles and an example forcing location is shown with a red circle. Note that the plate is symmetric around its center. Because of this, it is divided into four equal rectangles and the excitation is applied only on one of them. The PID spacing is constant for all 3 cases, 3 cm and 4 cm in x and y directions, respectively. For the C1 case, PIDs are placed around the center of the plate. In C2, PIDs are placed to the same quarter with the 6 separate excitation points. Lastly, C3 represents the case where the PIDs are moved with the excitation. The 4 PIDs are centered around the excitation points. Therefore, the PID locations are not constant.

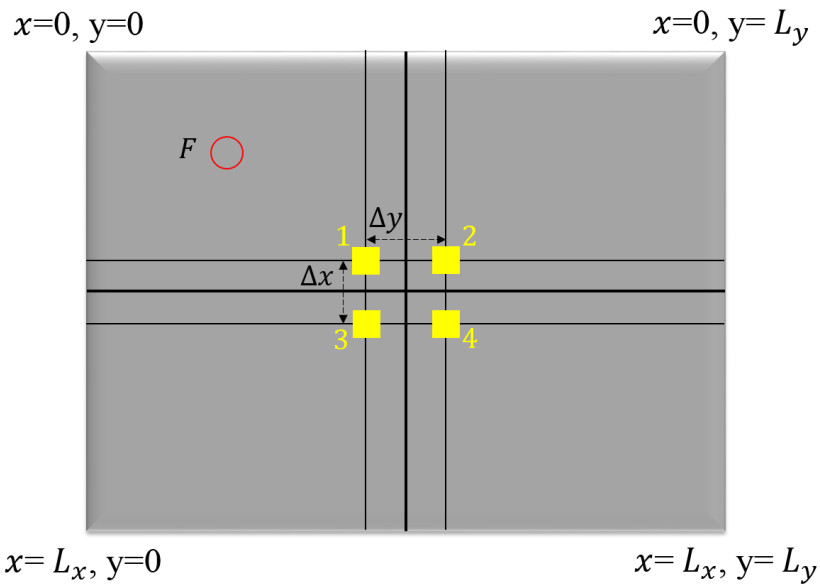

Figure 76: C1 PID locations

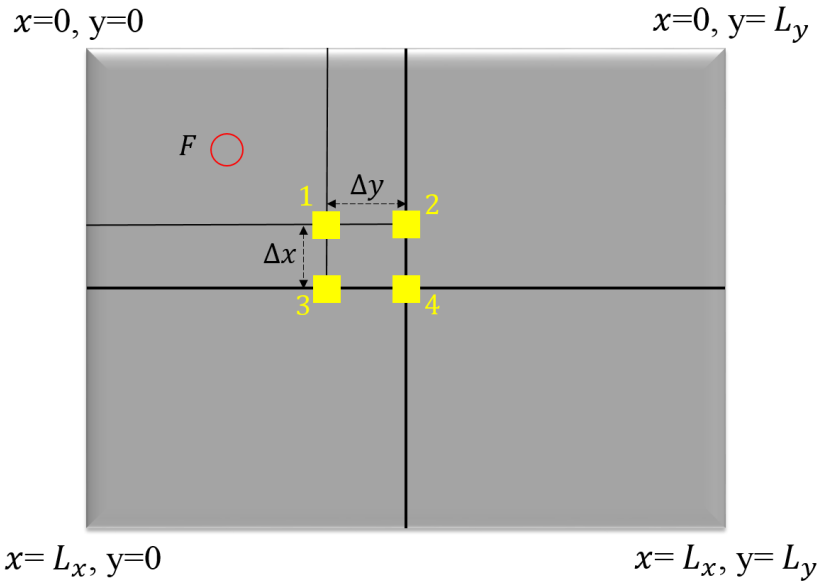

Figure 77: C2 PID locations

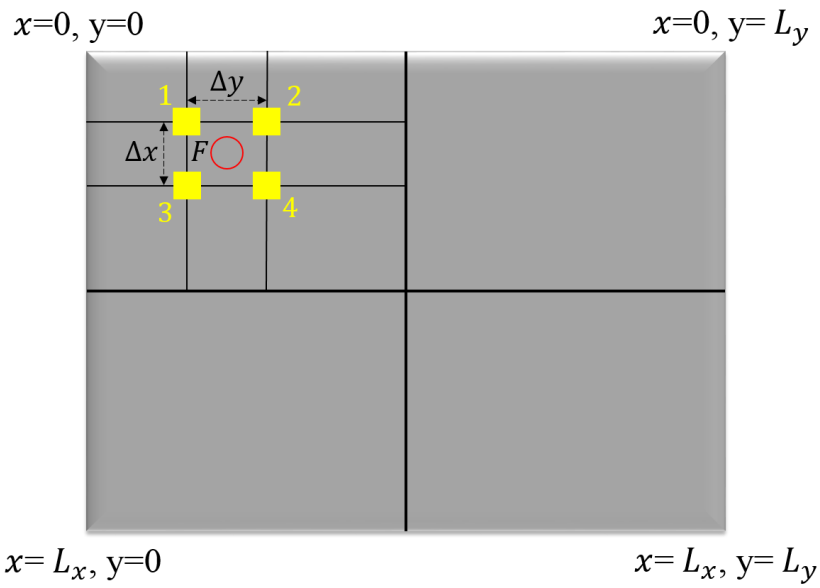

Figure 78: C3 PID locations

In Chapter 5, it was shown that the optimum locations for PIDs with low mass ratio and PIDs with high mass ratio are different. Therefore, two mass ratio cases are considered, a low mass ratio where $m' = 0.1$ and a high mass ratio where $m' = 1$. By this means, optimum gap clearances for the two cases can be analyzed. Note that C1 represents the optimum PID locations for the low mass ratio case and C3 represents the optimum PID locations for the high mass ratio case. C2 can be thought of as an intermediate case where the PIDs are closer to the excitation than C1 but the PID locations does not change with moving excitation point.

6.4.1 Optimizing Gap Clearances of the PIDs with Low Mass Ratio, $m' = 0.1$

Table 15 shows the optimization results of 4 PIDs for C1 case with a mass ratio of $m' = 0.1$. The objective function is the average value of the velocity ratios of 4 PIDs for 6 different excitation points given in Figure 75. The genetic algorithm slightly improved the fitness with respect to the PIDs with uniform gap clearances. 2-opt algorithm did not change the optimum solution.

Table 15: Optimization results for C1 and $m' = 0.1$.

Parameter	**Value**
Uniform fitness (mm/s)	116.5
GA fitness (mm/s)	115.7
GA gap clearances (mm)	2.25, 0.35, 0.38, 1.18
2-opt gap clearances (mm)	2.25, 0.35, 0.38, 1.18
2-opt fitness (mm/s)	115.7
Overall optimum fitness (mm/s)	115.7

Table 16 shows the optimization results of 4 PIDs for the C2 case. The fitness for uniformly filled PIDs is 117.3 mm/s. 2-opt algorithm has the optimum solution where the fitness is 114.6 mm/s. Note that PID #1 is the closest to the excitation point and it has the highest gap clearance. It is because the effect of the force is higher at that location and the particle can jump higher in PID #1.

Table 16: Optimization results for C2 and $m' = 0.1$.

Parameter	**Value**
Uniform fitness (mm/s)	117.3
GA fitness (mm/s)	115.6
GA gap clearances (mm)	0.38, 0.35, 2.25, 1.18

2-opt gap clearances (mm)	2.25, 0.35, 0.38, 1.18
2-opt fitness (mm/s)	114.6
Overall optimum fitness (mm/s)	114.6

Table 17 shows the optimization results of 4 PIDs for the C3 case. The fitness for uniformly filled PIDs is 198.4 mm/s and the optimum fitness is 176.8 mm/s. Compared to the C1 and C2 cases, C3 has the lowest effectiveness. This result confirms that, when the mass ratio is low, placing the PIDs around the excitation point is not a good choice in terms of the effectiveness.

Table 17: Optimization results for C3 and $m' = 0.1$.

Parameter	**Value**
Uniform fitness (mm/s)	198.4
GA fitness (mm/s)	178.6
GA gap clearances (mm)	4.37, 0.36, 0.10, 2.11
2-opt gap clearances (mm)	4.37, 0.36, 2.11, 0.10
2-opt fitness (mm/s)	176.8
Overall optimum fitness (mm/s)	176.8

6.4.2 Optimizing Gap Clearances of the PIDs with High Mass Ratio, $m' = 1$

Table 18 shows the optimization results of 4 PIDs for the C1 case with a mass ratio of $m' = 1$. The genetic algorithm slightly improved the fitness from 113.0 mm/s to 111.8 mm/s

with respect to the uniformly filled PIDs. 2-opt algorithm did not change the optimum result. PID #1, which is the closest to the excitation point, has the highest gap clearance. The difference in gap clearances between PID #1, 7.90 mm, and the others, 0.35 mm, 0.10 mm, 2.11 mm, is prominent.

Table 18: Optimization results for C1 and $m' = 1$.

Parameter	**Value**
Uniform fitness (mm/s)	113.0
GA fitness (mm/s)	111.8
GA gap clearances (mm)	7.90, 0.35, 0.10, 2.11
2-opt gap clearances (mm)	7.90, 0.35, 2.11, 0.10
2-opt fitness (mm/s)	111.8
Overall optimum fitness (mm/s)	111.8

Table 19 shows the optimization results of 4 PIDs for the C2 case with $m' = 1$. The fitness for uniformly filled PIDs is 129.3 mm/s and the optimum fitness is 128.5 mm/s. Although the PIDs in C2 is closer to the excitation points, this case has a lower average effectiveness compared to the C1 case. Therefore, for an arbitrary forcing location and a high mass ratio, moving the PIDs closer to the excitation point did not improve the effectiveness when the PID locations are constant.

Table 19: Optimization results for C2 and $m' = 1$.

Parameter	Value
Uniform fitness (mm/s)	129.3
GA fitness (mm/s)	128.5
GA gap clearances (mm)	1.21, 7.90, 0.10, 7.90
2-opt gap clearances (mm)	1.21, 7.90, 0.10, 7.90
2-opt fitness (mm/s)	128.5
Overall optimum fitness (mm/s)	128.5

Table 20 shows the optimization results of 4 PIDs for the C3 case with $m' = 1$. The fitness for uniformly filled PIDs is 47.6 mm/s and the optimum fitness is 45.9 mm/s. Note that, C3 was the worst case among the 3 low mass ratio cases. However, for high mass ratio, it has the best overall effectiveness when compared to the previous 5 cases, with low and high mass ratios. This result confirms that, when the mass ratio is high, placing the PIDs around the excitation point, and moving the PIDs with the excitation is the best choice.

Table 20: Optimization results for C3 and $m' = 1$.

Parameter	Value
Uniform fitness (mm/s)	47.6
GA fitness (mm/s)	45.9
GA gap clearances (mm)	1.33, 5.61, 1.56, 1.26

2-opt gap clearances (mm)	1.56, 5.61, 1.33, 1.26
2-opt fitness (mm/s)	45.9
Overall optimum fitness (mm/s)	45.9

6.4.3 Frequency Variation for Optimum and Uniform Gap Clearances

Figure 79 compares the velocity ratio variation of the 4 PIDs with optimum vs. uniform gap clearances as a function of frequency for C1 with $m' = 0.1$. The velocity ratio is the performance metric and a higher velocity ratio is desirable. Note that, C1 is the optimum PID location for the low mass ratio case. The y-axis is given in logarithmic scale for a better representation. The excitation frequency is varied between 20 Hz and 40 Hz because it is the common operating range for rivet guns. Although the PIDs with optimum gap clearances have higher velocity ratios for all frequencies, the difference is relatively small. Average velocity ratio for all frequencies in the range is 1.27 for the optimum case, whereas it is 1.25 for the uniform case. Therefore, the advantage of the optimum case is 1.6% with respect to the uniform case.

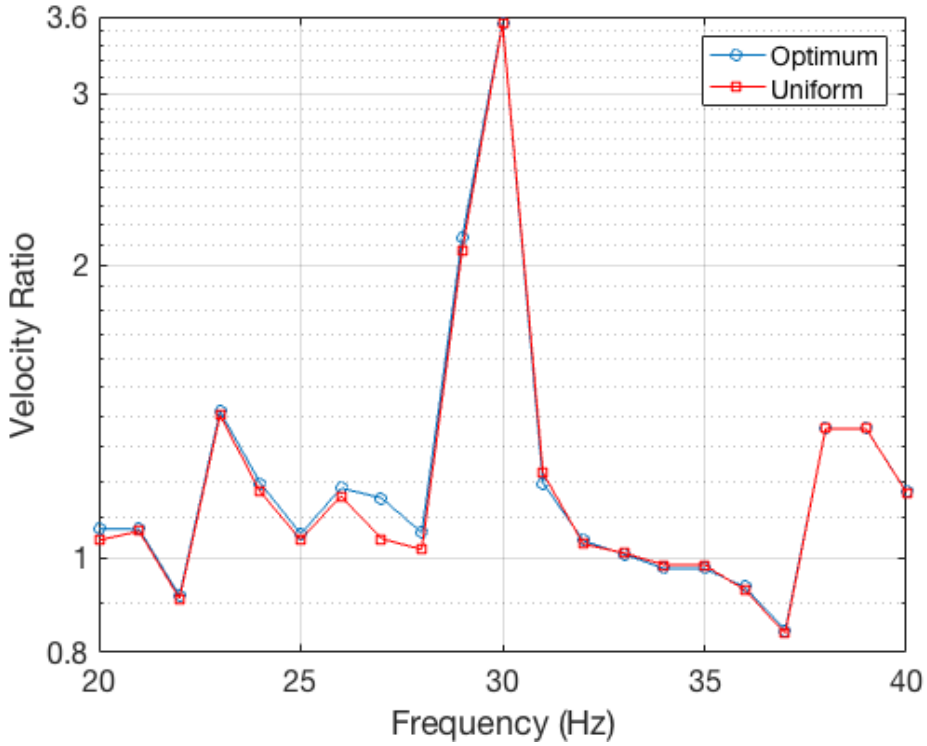

Figure 79: Velocity ratio variation as a function of frequency at C1 for $m' = 0.1$.

Figure 80 shows the velocity ratio variation of the 4 PIDs with optimum vs. uniform gap clearances as a function of frequency for C3 with $m' = 1$. Note that, C3 is the optimum PID location for the high mass ratio case. Again, the excitation frequency is varied between 20 Hz and 40 Hz. The PIDs with optimum gap clearances have higher velocity ratios for all frequencies except 22 Hz, where the velocity ratio is higher for the uniform case by 0.01. Average velocity ratio for all frequencies in the range is 2.27 for the optimum case, whereas it is 2.22 for the uniform case. Therefore, the advantage of the optimum case is 2.3% with respect to the uniform case. Maximum difference is at 30 Hz where the advantage of the optimum case is 3.53%.

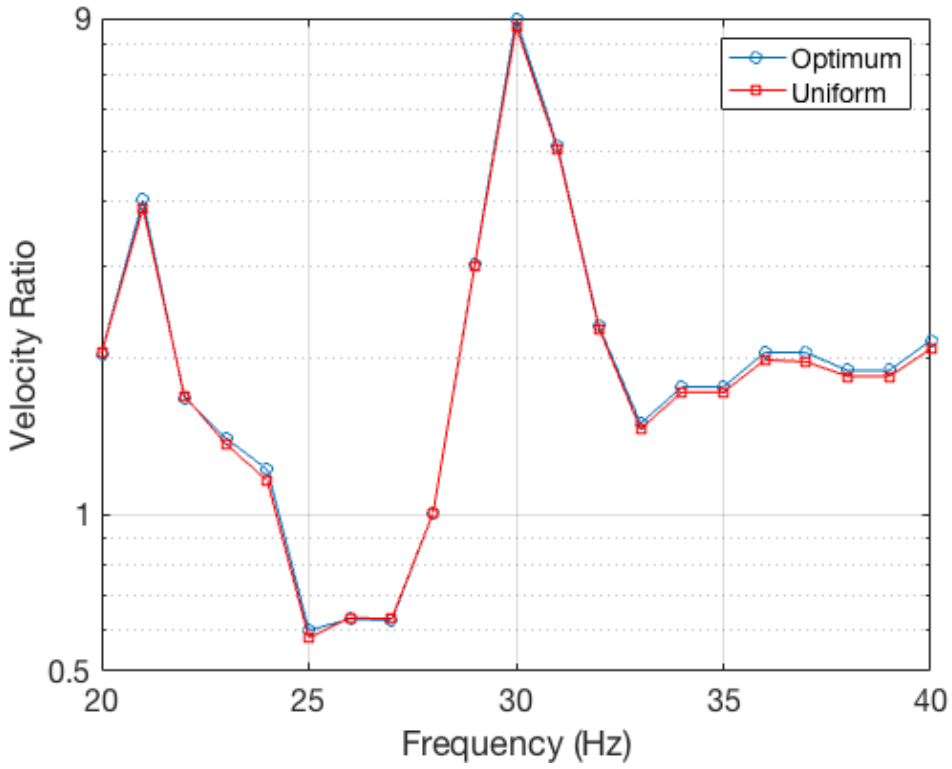

Figure 80: Velocity ratio variation as a function of frequency at C3 for $m' = 1$.

To summarize the results in this chapter, analyses on both the beam and the plate showed that optimizing the gap clearances for an arbitrary forcing location improves the PID effectiveness. However, frequency analysis showed that the advantage of the optimum case is significant only around the resonance frequency which was also used to conduct the optimization study. For other frequencies, either the advantage is relatively small or the PIDs with uniform gap clearances have better effectiveness. Overall, non-uniformly filled arrays of PIDs found to have higher effectiveness.

CHAPTER 7

CONCLUSIONS

7.1 Overview

In this dissertation, a novel resilient and removable PID model with "soft-floor and soft-ceiling" is introduced and analytically examined under periodic impulse excitation in the vertical direction. Effects of various parameters on a single PID, a beam with distributed array of PIDs, and a plate with distributed array of PIDs are analyzed. Optimum PID locations and gap clearances are sought for a cantilever beam and a simply supported plate.

Analyses on a single PID provided the following results:

- Treating PIDs as state-switched devices and using LTI simulation methods for response modeling are validated by comparing the simulation results with studies in the literature.
- A new performance metric, velocity ratio, is introduced which is defined as the ratio of RMS velocity of the base mass without an impact damper to the RMS velocity of the base mass with an impact damper.
- When a limit stop is used to model the compressional length of the resilient PID floor and ceiling, the model with the limit stop approaches to a higher velocity ratio value than the model without the limit stop as the forcing amplitude goes to infinity. However, in both cases the maximum effectiveness values and corresponding forcing amplitudes are the same. Therefore, using limit stop does not affect the optimum forcing amplitude and the resultant effectiveness.

- Ideally, the impulse force is assumed to be applied instantaneously. However, in reality it takes finite amount of time to apply the force. If an evenly distributed force is considered, maximum effectiveness decreases, and corresponding forcing amplitude increases as the forcing duration increases. However, when a triangular impulsive force is considered, there is not a significant change in the analysis results as the forcing duration increases.

Analyses on a cantilever beam with distributed array of PIDs provided the following results:

- PIDs have more potential under impulse excitation with respect to harmonic excitation to provide higher effectiveness within a broadband frequency range.
- There is an optimum gap clearance for a PID attached to a cantilever beam and optimum gap clearance is higher for higher forcing amplitudes. This means, for an arbitrary excitation and PID arrays, non-uniform gap clearances may be more effective.

The following results are valid when the beam is excited at the first natural frequency and the ratio of the mass of the PIDs to the mass of the beam is 0.1:

- For a fixed forcing location, PID effectiveness increases as the PIDs are moved towards the free end of the beam.
- For fixed PID locations, PID effectiveness increases as the forcing location is moved towards the free end of the beam.
- For an arbitrary forcing location, a single PID at the free end of the beam is more effective than multiple PIDs.

Analyses on a simply supported plate with distributed array of PIDs provided the following results:

- When the excitation frequency is varied around the first natural frequency of the plate, tuning the PID to the first natural frequency of the plate decreases the maximum velocity amplitude over the plate corresponding to the peak frequencies compared to the untuned case and helps the response to be less to the frequency variation. However, there is not a significant difference between the two cases if the average of the maximum velocity amplitudes in the broadband frequency range is considered. Overall, the PIDs should be tuned especially if the objective is to reduce the maximum velocity amplitude in the system.
- When the mass of the PID compared to the mass of the plate is low, PID effectiveness depends on the excitation frequency and the resultant deflection shapes. On the other hand, when the mass of the PID compared to the mass of the plate is high, PIDs are more effective when they are closer to the excitation.
- The difference between low and high mass ratios is a result of the effects of mass loading vs. damping on the effectiveness. The role of mass loading on the PID effectiveness is generally neglected in PID studies. However, the analysis results showed that for low mass ratios the effect of damping on the effectiveness is more dominant whereas for high mass ratios the effect of mass loading is the dominant factor.
- Keeping the total mass of the PIDs constant, if the number of PIDs with uniform gap clearances increases, the effectiveness also increases.

Optimization of the gap clearances for array of PIDs on a cantilever beam and a simply supported plate provided the following innovative aspects:

- For a fixed excitation frequency, optimizing the gap clearances for an arbitrary forcing location improves the PID effectiveness. Non-uniform gap clearances are more effective than uniform gap clearances.
- Frequency analysis showed that the advantage of the optimum case is significant only around the resonance frequency which was also used to conduct the optimization study. For other frequencies, either the advantage is relatively small or the PIDs with uniform gap clearances have better effectiveness. Overall, non-uniformly filled arrays of PIDs found to have slightly higher effectiveness.

REFERENCES

[1] Wang, D., Wu, C., Yang, R., and Lei, X., 2014, "FORCED VIBRATION OF THE PARTICLE-DAMPING BEAM BEASED ON MULTIPHASE FLOW THEORY OF GAS-PARTICLE," *21 Th International Congress on Sound & Vibration, Beijing, China*.

[2] de Melo, F. M., 2018, "On the Use of Particle Impact Dampers to Control Vertical Impact-Induced Vibration: An Experimental Investigation," University of Campinas.

[3] Masri, S. F., and Caughey, T. K., 1966, "On the Stability of the Impact Damper.," J. Appl. Mech., pp. 586–592.

[4] Papalou, A., and Masri, S. F., 1996, "Performance of Particle Dampers under Random Excitation," Trans.-Am. Soc. Mech. Eng. J. Vib. Acoust., **118**, pp. 614–621.

[5] Masri, S. F., 1970, "General Motion of Impact Dampers," J. Acoust. Soc. Am., **47**(1B), pp. 229–237.

[6] Lu, Z., Lu, X., Lu, W., and Masri, S. F., 2012, "Shaking Table Test of the Effects of Multi-Unit Particle Dampers Attached to an MDOF System under Earthquake Excitation," Earthq. Eng. Struct. Dyn., **41**(5), pp. 987–1000.

[7] Bapat, C. N., and Sankar, S., 1985, "Single Unit Impact Damper in Free and Forced Vibration," J. Sound Vib., **99**(1), pp. 85–94.

[8] Bapat, C. N., and Sankar, S., 1985, "Multiunit Impact Damper—Re-Examined," J. Sound Vib., **103**(4), pp. 457–469.

[9] Popplewell, N., and Liao, M., 1991, "A Simple Design Procedure for Optimum Impact Dampers," J. Sound Vib., **146**(3), pp. 519–526.

[10] Saeki, M., 2005, "Analytical Study of Multi-Particle Damping," J. Sound Vib., **281**(3), pp. 1133–1144.

[11] Saeki, M., 2002, "Impact Damping with Granular Materials in a Horizontally Vibrating System," J. Sound Vib., **251**(1), pp. 153–161.

[12] Ma, S., and Semercigil, S. E., 1997, "A Modified Passive Tuned Absorber for Secondary Systems under Random Excitation," J. Sound Vib., **208**(3), pp. 349–366.

[13] Papalou, A., and Masri, S. F., 1996, "Response of Impact Dampers with Granular Materials under Random Excitation," Earthq. Eng. Struct. Dyn., **25**(3), pp. 253–267.

[14] Witt, B. L., 2011, "Particle Impact Damping in the Horizontal Plane," Texas A&M University.

[15] Witt, B., and Kinra, V., 2006, "Particle Impact Damping in the Horizontal Plane," *47th AIAA/ASME/ASCE/AHS/ASC Structures, Structural Dynamics, and Materials Conference 14th AIAA/ASME/AHS Adaptive Structures Conference 7th*, p. 2209.

[16] Roy, Ranjit K., Rocke, R. D., and Foster, J. E., 1975, "The Application of Impact Dampers to Continuous Systems," J. Eng. Ind., p. 1317.

[17] Zahrai, S. M., and Rod, A. F., 2009, "Effect of Impact Damper on SDOF System Vibrations under Harmonic and Impulsive Excitations," *Journal of Physics: Conference Series*, IOP Publishing, p. 012066.

[18] Araki, Y., Yokomichi, I., and Jinnnouchi, Y., 1986, "Impact Damper with Granular Materials : 4th Report Frequency Response in a Horizontal System," Bull. JSME, **29**(258), pp. 4334–4338.

[19] de Melo, F. M., Bisgaard, E., and Cunefare, K. A., 2015, "Distributed Array of Particle Impact Dampers as a Removable Noise Control Treatment in Metal Fabrication," *INTER-*

NOISE and NOISE-CON Congress and Conference Proceedings, Institute of Noise Control Engineering, pp. 4556–4566.
[20] Ema, S., and Marui, E., 1996, "Damping Characteristics of an Impact Damper and Its Application," Int. J. Mach. Tools Manuf., **36**(3), pp. 293–306.
[21] Nelson, D. I., Nelson, R. Y., Concha-Barrientos, M., and Fingerhut, M., 2005, "The Global Burden of Occupational Noise-Induced Hearing Loss," Am. J. Ind. Med., **48**(6), pp. 446–458.
[22] Yang, M. Y., Lesieutre, G. A., Hambric, S. A., and Koopmann, G. H., 2005, "Development of a Design Curve for Particle Impact Dampers," Noise Control Eng. J., **53**(1), pp. 5–13.
[23] Inoue, M., Yokomichi, I., and Hiraki, K., 2011, "Particle Damping with Granular Materials for Multi Degree of Freedom System," Shock Vib., **18**(1–2), pp. 245–256.
[24] Yokomichi, I., Araki, Y., Jinnnouchi, Y., and Inoue, J., 1996, "Impact Damper with Granular Materials for Multibody System," J. Press. Vessel Technol., **118**, p. 95.
[25] Friend, R. D., and Kinra, V. K., 1999, "Measurement and Analysis of Particle Impact Damping," *1999 Symposium on Smart Structures and Materials*, International Society for Optics and Photonics, pp. 20–31.
[26] Friend, R. D., and Kinra, V. K., 2000, "Particle Impact Damping," J. Sound Vib., **233**(1), pp. 93–118.
[27] Ramachandran, S., and Lesieutre, G., 2008, "Dynamics and Performance of a Harmonically Excited Vertical Impact Damper," J. Vib. Acoust., **130**(2), p. 021008.
[28] Duncan, M. R., Wassgren, C. R., and Krousgrill, C. M., 2005, "The Damping Performance of a Single Particle Impact Damper," J. Sound Vib., **286**(1), pp. 123–144.
[29] Butt, A. S., and Akl, F. A., 1997, "Numerical Model of Impact-Damped Continuous Systems," J. Eng. Mech., **123**(4), pp. 384–392.
[30] Akl, F. A., and Butt, A. S., 1995, "Application of Impact Dampers in Vibration Control of Flexible Structures."
[31] Fowler, B. L., Flint, E. M., and Olson, S. E., 2001, "Design Methodology for Particle Damping," Proc. SPIE Int. Soc. Opt. Eng. Smart Struct. Mater. Proc SPIE, **4331**, pp. 186–197.
[32] Meirovitch, L., *Elements of Vibration Analysis. 1986*, Singapore, McGraw-Hill. ISBN 0-07-041342-8.
[33] Li, K., and Darby, A. P., 2006, "An Experimental Investigation into the Use of a Buffered Impact Damper," J. Sound Vib., **291**(3–5), pp. 844–860.
[34] Cheng, C. C., and Wang, J. Y., 2003, "Free Vibration Analysis of a Resilient Impact Damper," Int. J. Mech. Sci., **45**(4), pp. 589–604.
[35] Li, K., and Darby, A. P., 2009, "Modelling a Buffered Impact Damper System Using a Spring–Damper Model of Impact," Struct. Control Health Monit., **16**(3), pp. 287–302.
[36] Li, K., and Darby, A. P., 2006, "An Experimental Investigation into the Use of a Buffered Impact Damper," J. Sound Vib., **291**(3–5), pp. 844–860.
[37] Li, K., and Darby, A. P., 2006, "Experiments on the Effect of an Impact Damper on a Multiple-Degree-of-Freedom System," J. Vib. Control, **12**(5), pp. 445–464.
[38] Li, K., and Darby, A. P., 2008, "A Buffered Impact Damper for Multi-Degree-of-Freedom Structural Control," Earthq. Eng. Struct. Dyn., **37**(13), pp. 1491–1510.
[39] Chen, T., Mao, K., Huang, X., and Wang, M. Y., 2001, "Dissipation Mechanisms of Nonobstructive Particle Damping Using Discrete Element Method," *Smart Structures and*

Materials 2001: Damping and Isolation, International Society for Optics and Photonics, pp. 294–302.
[40] Xiao, W., Huang, Y., Jiang, H., Lin, H., and Li, J., 2016, "Energy Dissipation Mechanism and Experiment of Particle Dampers for Gear Transmission under Centrifugal Loads," Particuology, **27**, pp. 40–50.
[41] Michon, G., Almajid, A., and Aridon, G., 2013, "Soft Hollow Particle Damping Identification in Honeycomb Structures," J. Sound Vib., **332**(3), pp. 536–544.
[42] Vakakis, A. F., Gendelman, O. V., Bergman, L. A., McFarland, D. M., Kerschen, G., and Lee, Y. S., 2008, *Nonlinear Targeted Energy Transfer in Mechanical and Structural Systems*, Springer Science & Business Media.
[43] Vakakis, A. F., 2001, "Inducing Passive Nonlinear Energy Sinks in Vibrating Systems," J. Vib. Acoust., **123**(3), pp. 324–332.
[44] Vakakis, A. F., 2003, "Shock Isolation through the Use of Nonlinear Energy Sinks," Modal Anal., **9**(1–2), pp. 79–93.
[45] Vakakis, A. F., Manevitch, L. I., Gendelman, O., and Bergman, L., 2003, "Dynamics of Linear Discrete Systems Connected to Local, Essentially Non-Linear Attachments," J. Sound Vib., **264**(3), pp. 559–577.
[46] Li, T., Seguy, S., and Berlioz, A., 2017, "Optimization Mechanism of Targeted Energy Transfer with Vibro-Impact Energy Sink under Periodic and Transient Excitation," Nonlinear Dyn., **87**(4), pp. 2415–2433.
[47] Al-Shudeifat, M. A., Wierschem, N., Quinn, D. D., Vakakis, A. F., Bergman, L. A., and Spencer Jr, B. F., 2013, "Numerical and Experimental Investigation of a Highly Effective Single-Sided Vibro-Impact Non-Linear Energy Sink for Shock Mitigation," Int. J. Non-Linear Mech., **52**, pp. 96–109.
[48] Darabi, A., and Leamy, M. J., 2017, "Clearance-Type Nonlinear Energy Sinks for Enhancing Performance in Electroacoustic Wave Energy Harvesting," Nonlinear Dyn., **87**(4), pp. 2127–2146.
[49] Trigui, M., Foltete, E., and Bouhaddi, N., 2014, "Prediction of the Dynamic Response of a Plate Treated by Particle Impact Damper," Proc. Inst. Mech. Eng. Part C J. Mech. Eng. Sci., **228**(5), pp. 799–814.
[50] Panossian, H., Kovac, B., and Rackl, R., 2004, "Composite Honeycomb Treatment via Non-Obstructive Particle Damping (NOPD)," *45th AIAA/ASME/ASCE/AHS/ASC Structures, Structural Dynamics & Materials Conference*, p. 1689.
[51] Panossian, H., and Ehrgott, R., 2007, "Non-Obstructive Particle Damping (NOPD) Treatment Optimization for Composite Honeycomb Panels," *48th AIAA/ASME/ASCE/AHS/ASC Structures, Structural Dynamics, and Materials Conference*, p. 2047.
[52] Cunefare, K. A., De Rosa, S., Sadegh, N., and Larson, G., 2000, "State-Switched Absorber for Semi-Active Structural Control," J. Intell. Mater. Syst. Struct., **11**(4), pp. 300–310.
[53] Cunefare, K. A., 2002, "State-Switched Absorber for Vibration Control of Point-Excited Beams," J. Intell. Mater. Syst. Struct., **13**(2–3), pp. 97–105.
[54] Holdhusen, M. H., 2005, "The State-Switched Absorber Used for Vibration Control of Continuous Systems."
[55] Li, K., and Darby, A. P., 2009, "Modelling a Buffered Impact Damper System Using a Spring–Damper Model of Impact," Struct. Control Health Monit., **16**(3), pp. 287–302.
[56] Meirovitch, L., 2010, *Fundamentals of Vibrations*, Waveland Press.

[57] Halvorsen, W. G., and Brown, D. L., 1977, "Impulse Technique for Structural Frequency Response Testing," Sound Vib., **11**(11), pp. 8–21.
[58] Shames, I., 2017, *Energy and Finite Element Methods In Structural Mechanics: SI Units*, Routledge.
[59] Steinberg, D., 2000, *Vibration Analysis for Electronic Equipment*, John Wiley and Sons Inc.: New York, NY, USA.